# Development of High-Speed Camera Techniques for Droplet Measurement in Annular Flows

**Ayden Cohn**

Thesis submitted to the faculty of the
Virginia Polytechnic Institute and State University
in partial fulfillment of the requirements for the degree of

Master of Science
In
Nuclear Engineering

Yang Liu, Chair

Alireza Haghighat

Mark Pierson

May 2, 2024

Blacksburg, Virginia

Keywords: annular regime, depth-of-field, droplet, high-speed camera, two-phase flow

Annular Regime Droplet Measurement Technique with High-Speed Cameras

Ayden Cohn

# Abstract

This research addresses the critical need for precise two-phase flow data in the development of computer simulation models, with a specific focus on the annular flow regime's droplet behavior. The study aims to contribute to the evaluation of safety and efficiency in nuclear reactors that handle fluids transitioning between liquid and gas states for thermal energy transport. Central to the investigation is the collection and analysis of droplet size and velocity distribution data, particularly to help with developing models for the water-cooled nuclear power plants. The experimental setup employs advanced tools, including a high-speed camera, lens, teleconverter, and a selected light source, to capture high-resolution images of droplets. Calibration procedures, incorporating depth of field testing, are implemented to ensure accurate droplet size measurements. A critical component of the research is the introduction of a droplet identification program, developed using Matlab, which facilitates efficient processing of experimental data. Preliminary results from the Virginia Tech test facility demonstrate the system's capability to eliminate out-of-focus droplets and obtain precise droplet data in a reasonable amount of time. Experimental results from the Rensselaer Polytechnic Institute test facility provide droplet size and velocity distributions for a variety of annular flow conditions. This facility has a concurrent two-flow system that pumps air and water at different rates through a 9.525 mm inner diameter tube. The conditions tested include gas superficial velocities ranging from 22 to 40 m/s and liquid superficial velocities ranging from 0.09 to 0.44 m/s. The measured flow has a temperature of 21°C and a pressure of 1 atm.

Annular Regime Droplet Measurement Technique with High-Speed Cameras

Ayden Cohn

# General Audience Abstract

This research explores the behavior of small droplets as fluids transition between liquid and gas states, particularly within the context of the cooling water in nuclear power plants. The overarching goal is to collect data on these droplets to improve computer simulations that help design nuclear reactors and assess their safety. This is important because it is often infeasible due to safety, monetary, or time restrictions to physically test some nuclear reactor equipment. The study employs state-of-the-art technology, including high-speed cameras and specialized imaging tools, to capture and analyze droplet size distribution data. This investigation is pivotal in ensuring the fuel in nuclear reactors remain adequately cooled during part of the boiling process. The research methodology includes the development of a droplet identification program using Matlab, ensuring efficient processing of experimental data. Preliminary findings from experimental tests at Virginia Tech showcase the program's capability to filter out irrelevant data and provide accurate droplet information. Experimental results from the Rensselaer Polytechnic Institute annular flow test facility provide droplet size and velocity data for a range of conditions that cooling water may face. Beyond its contributions to nuclear engineering, this research holds promise for influencing advancements in various applications that involve liquid droplets, opening avenues for innovation in the broader scientific and engineering communities.

# Acknowledgments

I would like to sincerely thank my advisor, Dr. Yang Liu, for his guidance over the past two years. I am very appreciative of the amount of time he allocated and assistance he offered to help make me a better researcher. I would also like to thank my thesis advisory committee members, Dr. Alireza Haghighat and Dr. Mark Pierson for their input to my thesis and for providing me with valuable experiences, such as mentoring me during my GTA position, including me in a nuclear energy political event with Governor Youngkin, and involving me in undergraduate nuclear engineering research. I am also deeply grateful for Dr. Pierson's willingness to serve on my committee considering his retirement status. It has been an honor to work with all three of these nuclear engineering experts during my time at Virginia Tech and I look forward to when our paths cross next.

Special thanks to my colleagues at Rensselaer Polytechnic Institute, Dr. Shanbin Shi, Eymon Lan, and Ilyas Yilgor. Without their contributions in constructing the test facility, my work would have much less significance. They were also very welcoming during my stay in New York.

I would also like to thank my parents and brother Brian for their unconditional support. I am so lucky to have these three people in my life.

# Contents

# List of Figures

# List of Tables

# List of Abbreviations

| | |
|---|---|
| CDF | cumulative distribution function |
| $C_w$ | constant defined by equation (5) |
| D | droplet diameter |
| $D_h$ | hydraulic diameter of pipe |
| $D_{vm}$ | volumetric median diameter |
| j | superficial velocity |
| Nμ | Viscosity number defined by equation (6) |
| P | absolute pressure |
| PDF | probability density function |
| PIV | particle image velocimetry |
| PSV | particle streak velocimetry |
| PTV | particle tracking velocimetry |
| Q | volumetric flowrate |
| Re | Reynolds Number |
| SCFH | standard cubic feet per hour |
| Um | magnitude of velocity (total speed) |
| Ux | magnitude of horizontal component of velocity (horizontal speed) |
| Uz | magnitude of vertical component of velocity (vertical speed) |
| We | Weber Number |
| y | parameter defined by equation (2) and (7) |
| $\alpha_d$ | droplet fraction |
| Δ | volume fraction oversize |
| Δρ | density difference between phases |
| μ | dynamic viscosity |
| ρ | density |
| σ | surface tension |

**Subscripts:**

| | |
|---|---|
| f | liquid phase |
| g | gas phase |

# Chapter 1

# 1. Introduction

## 1.1 Background

Developing computer simulation models with accurate two-phase flow data is critical to assessing the safety and effectiveness of equipment that utilizes fluids that occur in both the liquid and gas state. A strong model with accurate data can simulate a variety of conditions of these types of equipment without needing to physically test the equipment, which can be expensive, unsafe, or not possible in certain instances. Further, equipment can be tested through simulation before it is ever built. There are a variety of important occurrences of two-phase flow such as irrigation methods, steam boilers, equipment in the chemical industry, and refrigeration systems [1-2]. Another unique, but very important, natural process that could be modeled as two-phase flow is the vapor and mucus mixture in the airway of humans and other animals, which can lead to transmission of diseases such as coronavirus disease 2019 (COVID-19) [3]. A limitation of many current two-phase flow models is the lack of high-quality experimental data to use for validation of the models.

This study focuses on a data acquisition method for entrained water droplets in the annular regime of two-phase flow for nuclear reactors that use water as their coolants. While there are other types of nuclear reactor coolants such as liquid sodium, air, or carbon dioxide, the most commonly used coolant in the United States is water [4]. Water is used as the coolant in pressurized

water reactors (PWRs), boiling water reactors (BWRs), and heavy water reactors such as the Canada Deuterium Uranium reactor (CANDU) [5]. As new advanced water-cooled reactors are designed, it is important that their safety can be accurately assessed before they are built and operated through simulation. Actual experimental data can be used to make the simulations more accurate or validate current simulations, especially if they relied on artificially created data.

Within nuclear power plants that use water as coolant, there are a few different occurrences of two-phase flow besides the primary coolant, such as the containment spray system, the steam generator, and the pressurizer [6-7]. Some of the methods in this study could be used to collect data for these systems, but this study focuses on the annular flow regime in light water reactor cores. Understanding and collecting data for the different boiling regimes of cooling water is important because different regimes of two-phase flow lead to different heat transfer rates. If not enough heat is transferred from the nuclear fuel in the core, there could be a risk of a meltdown. Therefore, it is critical that there is enough liquid water, as opposed to vapor, in contact with the fuel since liquid conducts heat at much higher rates than gas.

## 1.2 Two-Phase Flow Regimes

As liquid water boils and vapor forms, the two-phase flow mixture goes through a few different regimes with different behaviors. For vertical gas-liquid flow, four key flow regimes were defined by Hewitt and Hall-Taylor and are still commonly used today [8]. These four regimes are bubbly flow, slug flow, churn flow, and annular flow. There are sub-regimes within these main four regimes, but only annular flow is analyzed more closely for this study. A two-phase flow mixture can undergo these regime changes from either adiabatic or diabatic processes [9]. This

study utilizes adiabatic processes to avoid the need for high temperatures. Instead, the liquid and gas flowrates are varied to achieve the different flow regimes without transferring heat.

Bubbly flow occurs at the lowest gas flow rate of the four main regimes for a constant liquid flow rate. Small gas bubbles flow inside liquid. As the gas flow rate increases, larger and longer bubbles form during the slug regime. Smaller bubbles join to make these cap bubbles. These large gas bubbles continue to grow as gas flow rate increases, become lined up closer to each other, and the top of bubbles sometimes touch the bottom of bubbles above them. This makes the bubbles unstable due to the strong wake effect and the flow is known as the churn flow regime [10]. Bubbles in the churn regime are constantly created and destroyed due to rapid breakups and coalescences. If the gas flow rate continues to increase, there will no longer be large discrete bubbles. Instead, a thin liquid film forms on the surface of the pipe with a gas inner core, as the two-phase flow enters the annular regime. The liquid film may still contain smaller gas bubbles and the inner core may have liquid droplets during different sub-regimes of annular flow.

These four main regimes can be seen in Figure 1[9]. Figure 1(a) allows for view inside the middle of the pipe, which is harder to see for the churn and annular regime of the real images in Figure 1(b). This study uses a 9.525 mm diameter pipe, which is smaller than the 25.4 mm pipe in Figure 1(b).

Much research has been conducted to define the boundaries between the different flow regimes more accurately. Once these boundaries are defined, it is common for flow regime maps to be created to plot the boundaries for specific flow geometries. These maps often use the superficial velocities of the two-phases ($j_g$ and $j_f$) as the axes but can also use void fraction on one of the axes. The subscript “g” refers to parameters of the gas (air in the present study) and the

subscript “f” refers to parameters of the liquid (water in the present study). A commonly referenced flow regime map was created by Mishima and Ishii and is slightly updated for this study and shown in Figure 2 [10].

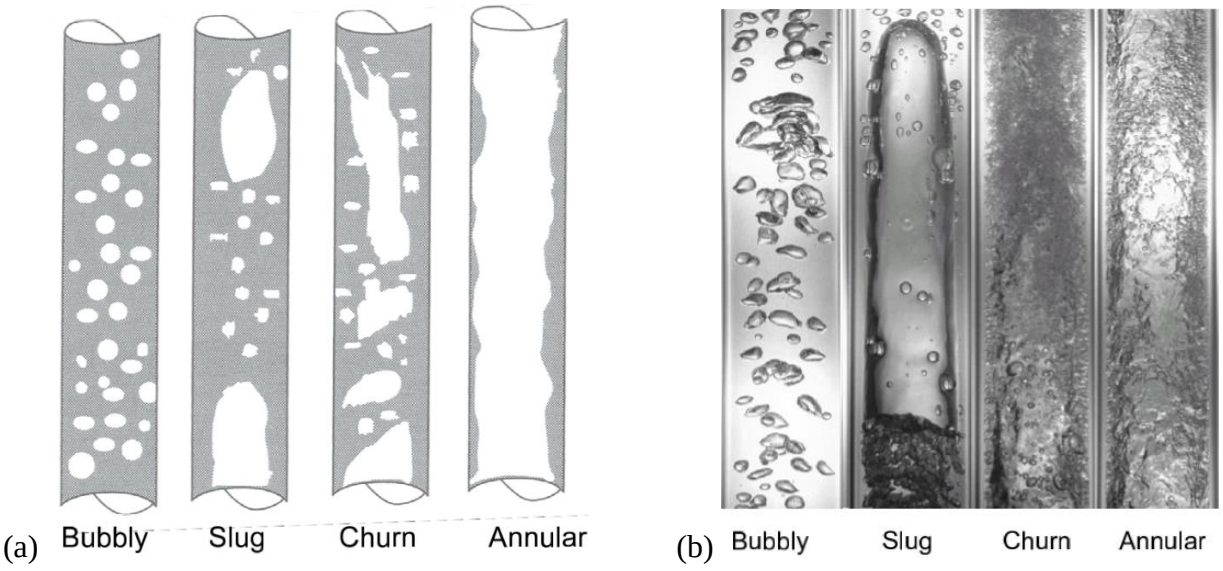


*Figure 1: (a) Simplified Drawings of Two-Phase Vertical Flow Regimes and (b) Images of Two-Phase Vertical Flow Regimes in a 25.4 mm Diameter Pipe [9].*

The original flow regime map does not distinguish between different parts of the annular regime. Therefore, an additional section is included to separate the entrainment and no entrainment sections of the annular regime according to the inception criteria for droplet entrainment developed by Ishii and Grolmes [11]. This is an important distinction since this study is designed to study entrained droplets. Another change to the flow regime map is the inclusion of the designed operating range of the two-phase flow test facility that is used for testing at RPI [12]. Finally, geometric properties of the test facility and physical properties of air and water are substituted into

the regime and entrainment equations to finish Figure 2 [10-11]. This map is useful to select superficial velocity combinations that will be in the annular regime, contain droplet entrainment, and be possible for the test facility.

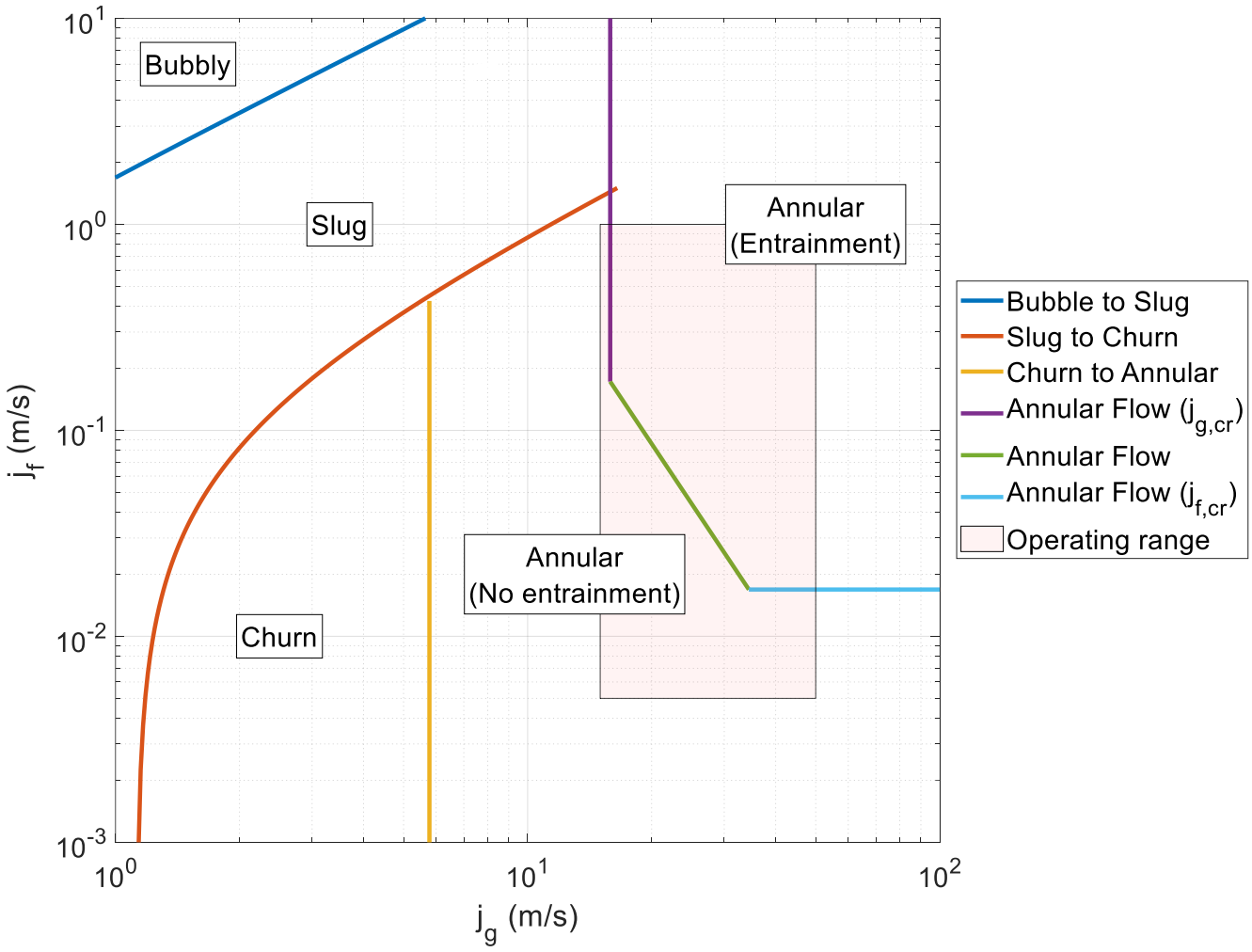


*Figure 2: Two-Phase Flow Regime Map with RPI Facility Operating Range [10-12].*

## 1.3 Theoretical Droplet Size Distribution

The literature provides a few models which estimate the size distribution of droplets in annular two-phase flow. These models are useful to help predict the size of droplets that will be expected for different test conditions. This helps determine the size range of droplets that the system needs to be designed to measure. Additionally, these models are used to compare the data collected for the droplet size distribution at different annular flow conditions.

A widely referenced model for the size distribution of droplets in annular two-phase flow was developed by Kataoka et al. [13]. The model calculates the volumetric median diameter ($D_{vm}$) as

$$D_{vm} = 0.28 \frac{\sigma}{\rho_g j_g^2} Re_f^{-\frac{1}{6}} Re_g^{\frac{2}{3}} \left(\frac{\rho_g}{\rho_f}\right)^{-\frac{1}{3}} \left(\frac{\mu_g}{\mu_f}\right)^{\frac{2}{3}} \quad (1)$$

where σ is the surface tension between the two fluids, ρ is density, Re is Reynolds number, and μ is dynamic viscosity. A dimensionless variable y is calculated with $D_{vm}$ as

$$y = \ln\left(\frac{2.13D}{3.13D_{vm} - D}\right) \quad (2)$$

where D is droplet diameter. Finally, a correlation for droplet distribution is obtained as

$$\frac{d\Delta}{dy} = \frac{0.884}{\sqrt{\pi}} e^{-0.781y^2} \quad (3)$$

where Δ is the volume fraction oversize, or fraction of volume in droplets with a diameter larger than D. This model was later revised by Kocamustafaogullari et al. a decade later to include the effects of the dynamic forces and surface tension's stabilizing effect on droplet size [14]. This updated model calculates the volumetric median diameter ($D_{vm}$) as

$$D_{vm} = 0.9 D_h C_w{}^{-\frac{4}{15}} We^{-\frac{3}{5}} \left(\frac{Re_g^4}{Re_f}\right)^{\frac{1}{15}} \left(\frac{\rho_g/\rho_f}{\mu_g/\mu_f}\right)^{\frac{4}{15}} \quad (4)$$

where $D_h$ is the inner diameter of the pipe containing the flow, We is the Weber number, and $C_w$ is defined as

$$C_w = \frac{1}{35.34} N\mu^{4/5} \ \ for\ N\mu \leq \frac{1}{15} \quad (5a)$$

and

$$C_w = 0.25 \ \ for\ N\mu > \frac{1}{15} \quad (5b)$$

where viscosity number, Nμ, is defined as

$$N\mu = \frac{\mu_f}{\sqrt{\rho_f \sigma \sqrt{\frac{\sigma}{g\Delta\rho}}}}. \quad (6)$$

The dimensionless variable y is calculated with $D_{vm}$ as

$$y = \ln\left(\frac{1.93D}{2.93D_{vm} - D}\right) \quad (7)$$

and a correlation for droplet distribution is obtained as

$$\frac{d\Delta}{dy} = \frac{0.75}{\sqrt{\pi}} e^{-0.563y^2}. \quad (8)$$

Both models take liquid and gas superficial velocities, $j_f$ and $j_g$, as inputs along with physical properties of the fluids and the hydraulic diameter of the flow passage as inputs. The models output correlations for droplet size distributions that can be used to generate a cumulative distribution function (CDF) and probability density function (PDF) for any combination of superficial velocities within the annular regime that experiences droplet entrainment. Figure 3 presents a CDF and PDF for an example combination of superficial velocities within the annular

flow regime for the model developed by Kataoka et al. (shown by striped lines) and by Kocamustafaogullari eta al. (shown by solid lines) [13-14].

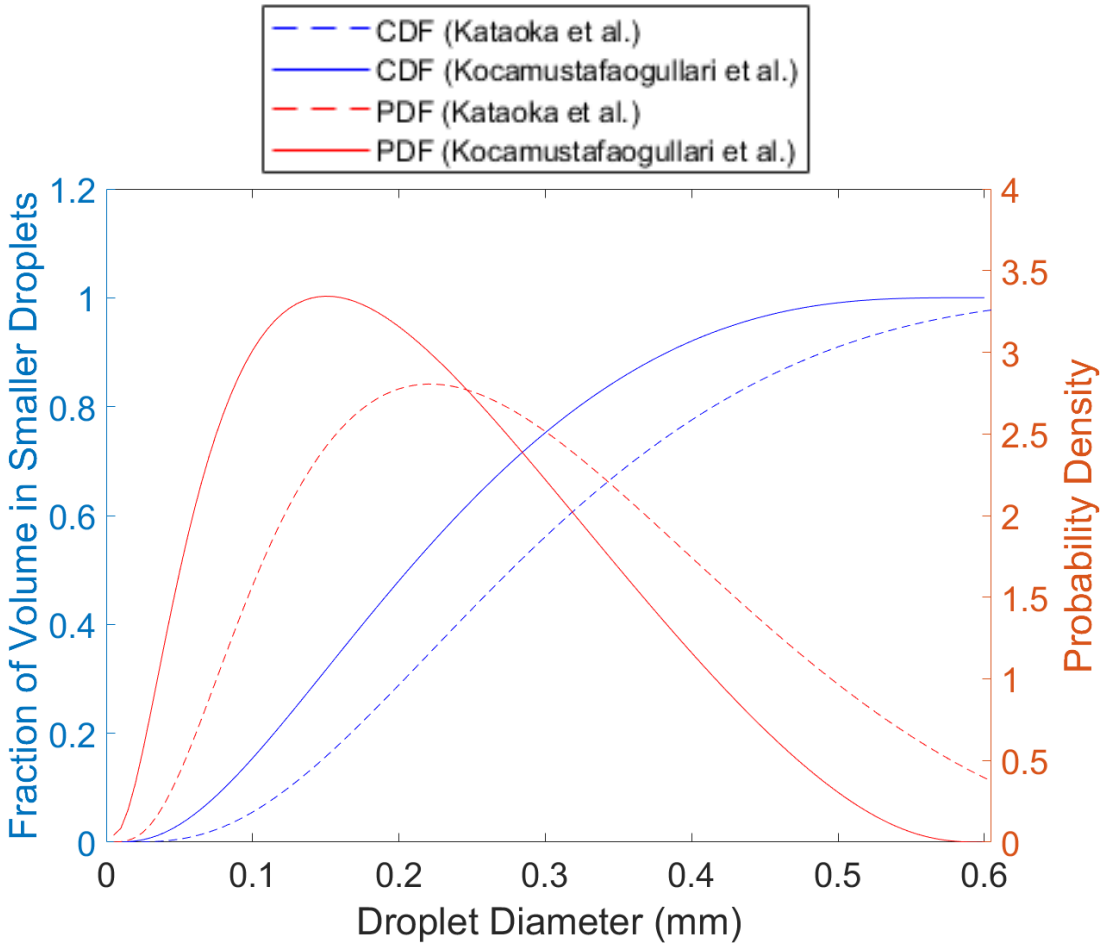


*Figure 3: CDF and PDF of droplet sizes for jg = 30 m/s and jf = 0.1 m/s [13-14].*

Figure 4(a) and Figure 4(b), which are also based on the model developed by Kataoka et al., show the effect of changing the gas superficial velocity or the liquid superficial velocity on the cumulative distribution function of droplet sizes. As either superficial velocity increases, the graphs move leftward towards smaller droplets. This analysis shows that the graphs move faster in changes in gas superficial velocity than for changes in liquid superficial velocity. Therefore, droplet size distributions for annular flow are more sensitive to changes in gas superficial velocity.

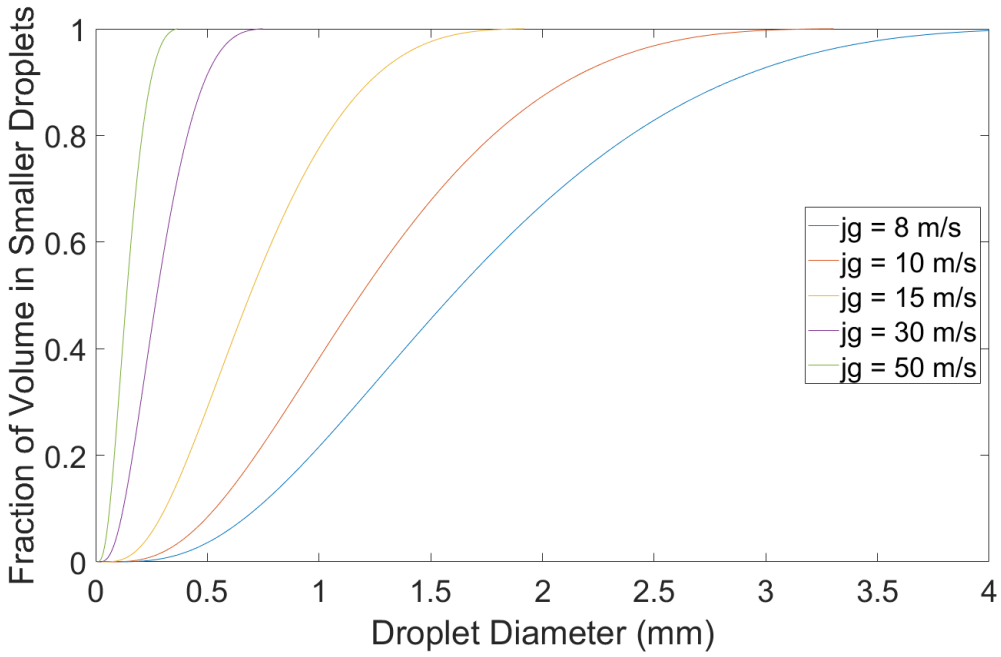


a)

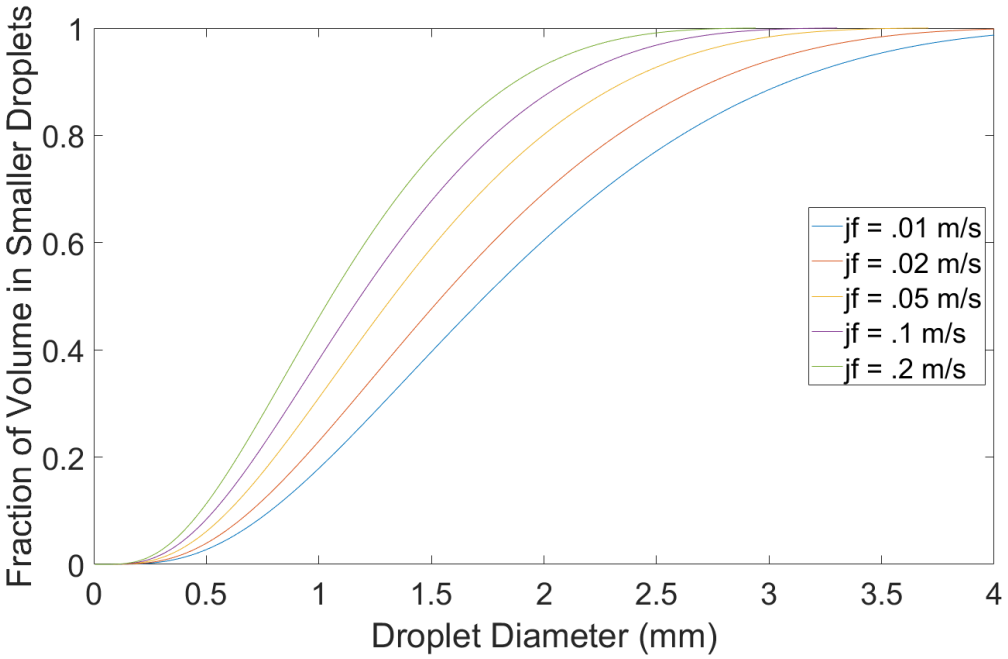


b)

*Figure 4: CDF of Droplet Sizes as (a) gas superficial velocity changes with $j_f$ = 0.1 m/s and (b) as liquid superficial velocity changes with $j_g$ = 10 m/s[13].*

## 1.4 Previous Two-Phase Flow Data Acquisition Methods

Numerous studies in the literature have explored various approaches to devising data acquisition techniques for the analysis of two-phase flow involving air and water. These include procedures for both raw data collection and data processing. One method that has been used to collect two-phase flow data involves using an x-ray densitometry system [15-16]. This technique can be used to capture accurate void fraction and velocity data; however, it is not capable of collecting individual droplet size data. Another study used x-ray densitometry in conjunction with high-speed imaging and a conductivity probe to collect more two-phase flow data than would be possible with just x-ray densitometry but did not study droplets [17]. Other previous studies have used high-speed cameras to study droplets in annular flow. Some studies used a high-speed camera to test how well other equipment, such as a conductivity probe or optical probe, could measure droplets [18-19]. These studies analyzed individual droplets rather than frames of many droplets as with the present study.

Additionally, other studies have collected actual data of droplets in annular flow, rather than to test another data acquisition method [20-21]. These studies displayed the effectiveness of using a high-speed camera to collect droplet data but have a few differences from the present study. One major difference is that they use other technology in addition to the high-speed cameras, such as a particle dynamics analyzer, to compensate for lower resolution images than the technique used in the present study. They also collected data from pipes with a different geometry than the data that is collected in the present study. The images captured in this study contain pixels that correspond to smaller physical distances, as low as 5.7 micrometers. This leads to the capability to analyze smaller droplets than in previous studies that used high-speed cameras to study droplets in annular flow.

Some studies have also developed image processing algorithms for two-phase flow images. This research is focused on bubbly flow and resulted in the development of a two-dimensional bubble identification program that can identify individual bubbles, even if they are overlapped [22-23]. This algorithm was improved by tracking individual bubbles with multiple cameras to create three-dimensional size data models [24-26]. Some of the algorithms developed for bubbles are modified to identify significantly smaller droplets in this study. Information about the modified algorithms is located in Chapter 4.

The literature also provides previous research to create velocity distributions of single and two-phase flow through velocimetry methods [27-28]. The velocimetry methods consist of particle image velocimetry (PIV), particle tracking velocimetry (PTV), and particle streak velocimetry (PSV). PIV analyzes the velocity field of an entire region in successive images to determine fluid velocity, while PTV focuses on tracking individual particles. In contrast, PSV captures particle streaks in long-exposure images to determine the velocity from the distance traveled during the exposure time. These methods provide options for creating droplet velocity distributions in the present study.

## 1.5 Objectives

The presented research in this thesis intends to develop a test procedure that can be used to collect droplet size and velocity distribution data at both the Virginia Tech and RPI test facilities. The objectives for the data collection process are described below:

a) Select equipment for droplet measurement procedure that can be transported to the RPI test facility [12].

b) Develop and test a camera calibration method to determine the focal plane and verify consistent lighting conditions during course of experiment.
c) Test data collection procedure at small-scale Virginia Tech facility with droplets produced through an atomization nozzle.
d) Collect annular flow droplet size and velocity data at the RPI test loop [12].

The research in this thesis also aims to develop a droplet measurement program to analyze the droplet images recorded and produce droplet size and velocity distributions. The objectives for the data analysis process are described below:

a) Modify bubble identification algorithm, developed by Fu and Liu, to successfully identify in-focus droplets and create size distributions [22].
b) Modify particle tracking velocimetry (PTV) algorithm, developed by Wang, to successfully identify droplet velocity distributions [28].

## 1.6 Outline

This thesis is organized as follows:

- Chapter 2 presents the equipment testing and selection for the high-speed cameras, camera lens and lens accessories, lights, and other minor equipment.
- Chapter 3 presents the calibration target creation process, testing, and final selection, enabling the assessment of depth-of-field.
- Chapter 4 presents the droplet identification programs.
- Chapter 5 presents preliminary testing at the small-scale Virginia Tech test facility with droplets produced through an atomization nozzle and its results.

- Chapter 6 presents annular two-phase flow testing at the RPI test loop, collection of droplet data, and its results.
- Chapter 7 summarizes the important conclusions and discusses future work.

# Chapter 2

# 2. Experimental Setup

Several pieces of important equipment are carefully selected and tested at Virginia Tech with the goal of bringing them to the RPI test facility to collect annular flow data. This includes the high-speed cameras, camera lenses and lens accessories, and the lights. Some minor equipment, such as diffusor paper and stands for the cameras and lights are also discussed. Equipment for the calibration testing is discussed in Chapter 3. The main specification that the camera setup needs to meet is capturing 11 mm width images. The RPI test facility is designed with 10.5 mm internal diameter pipes, which will provide a flow of droplets. The cameras need to capture the entire width of flow to create radial profiles. Therefore, an 11 mm target width allows for a small amount of buffer and will maximize the number of pixels on the cameras' sensors that will capture droplet data.

## 2.1 Camera Selection and Magnification

Two high-speed cameras are used to collect data both at the Virginia Tech and RPI test facility, one Photron Fastcam SA4 and one Photron Fastcam SA6. Two cameras are employed for gathering annular flow data to ensure uniform radial distribution of data around the test section. The cameras each collect data at two different frame rates and are placed 90 degrees apart, facing the center of droplet flow.

First, both cameras take images at their maximum resolutions, with low frame rates, to collect data that is used to accurately study droplet size radial distributions for different flow conditions. The SA4 has a maximum resolution of 1,024 by 1,024 pixels and the SA6 has a maximum resolution of 1,920 by 1,440 pixels [29-30]. Therefore, for particle size distribution data, the SA6 will perform better due to its high maximum resolution and collect the primary data. The data collected by the SA4 will be used to validate that the radial distribution is similar from a perpendicular view. A relatively low frame rate can be used because individual droplets are not tracked in successive frames. Full specifications, including resolutions at each frame rate, can be seen for the SA4 in Table 1 and for the SA6 in Table 2. The highest frame rate that provides the maximum resolution is selected for each camera. A high shutter speed of 1/277,000 s is used for this portion of testing to minimize motion blur. More information about the selection of shutter speeds can be found in Chapter 5.

*Table 1: Photron Fastcam SA4 Specifications at Different Frame Rates (Selected Frame Rate Bolded) [29].*

| Frame Rate | Maximum Resolution | | Pixel Size with 11 mm width of window | Height Recorded | Magnification Ratio Needed | # Images per droplet at 15 m/s |
|---|---|---|---|---|---|---|
| | Horizontal | Vertical | | | | |
| fps | pixels | pixels | µm | mm | - | Count |
| 1000 | 1024 | 1024 | 10.7 | 11 | 1.86 | 0.7 |
| 2000 | 1024 | 1024 | 10.7 | 11 | 1.86 | 1.5 |
| 3000 | 1024 | 1024 | 10.7 | 11 | 1.86 | 2.2 |
| **3600** | **1024** | **1024** | **10.7** | **11** | **1.86** | **2.6** |
| 5000 | 1024 | 768 | 10.7 | 8.3 | 1.86 | 2.8 |
| 6750 | 1024 | 576 | 10.7 | 6.2 | 1.86 | 2.8 |
| 7500 | 1024 | 512 | 10.7 | 5.5 | 1.86 | 2.8 |
| 10000 | 768 | 512 | 14.3 | 7.3 | 1.40 | 4.9 |
| 12500 | 640 | 480 | 17.2 | 8.3 | 1.16 | 6.9 |
| 13500 | 512 | 512 | 21.5 | 11 | 0.93 | 9.9 |
| 27000 | 512 | 256 | 21.5 | 5.5 | 0.93 | 9.9 |
| 36000 | 384 | 240 | 28.6 | 6.9 | 0.70 | 16.5 |
| 45000 | 256 | 256 | 43.0 | 11 | 0.47 | 33.0 |
| 50000 | 320 | 192 | 34.4 | 6.6 | 0.58 | 22.0 |
| 86400 | 256 | 128 | 43.0 | 5.5 | 0.47 | 31.7 |

*Table 2: Photron Fastcam SA6 Specifications at Different Frame Rates (Selected Frame Rate Bolded) [30].*

| Frame Rate | Maximum Resolution | | Pixel Size with 11 mm width of window | Height Recorded | Magnification Ratio Needed | # Images per droplet at 15 m/s |
|---|---|---|---|---|---|---|
| | Horizontal | Vertical | | | | |
| fps | pixels | pixels | µm | mm | - | Count |
| 250 | 1920 | 1440 | 5.73 | 8.3 | 1.75 | 0.1 |
| 500 | 1920 | 1440 | 5.73 | 8.3 | 1.75 | 0.3 |
| **1125** | **1920** | **1440** | **5.73** | **8.3** | **1.75** | **0.6** |
| 1500 | 1920 | 1080 | 5.73 | 6.2 | 1.75 | 0.6 |
| 2000 | 1280 | 1024 | 8.59 | 8.8 | 1.16 | 1.2 |
| 3000 | 1024 | 768 | 10.7 | 8.3 | 0.93 | 1.7 |
| 4000 | 1280 | 512 | 8.59 | 4.4 | 1.16 | 1.2 |
| 4500 | 1024 | 512 | 10.7 | 5.5 | 0.93 | 1.7 |
| 5000 | 768 | 512 | 14.3 | 7.3 | 0.70 | 2.4 |
| 6000 | 768 | 448 | 14.3 | 6.4 | 0.70 | 2.6 |
| 8000 | 512 | 384 | 21.5 | 8.3 | 0.47 | 4.4 |
| 12000 | 512 | 256 | 21.5 | 5.5 | 0.47 | 4.4 |
| 25000 | 256 | 128 | 43.0 | 5.5 | 0.23 | 9.2 |
| 45000 | 256 | 64 | 43.0 | 2.8 | 0.23 | 8.3 |
| 75000 | 256 | 32 | 43.0 | 1.4 | 0.23 | 6.9 |

Second, the cameras are adjusted to collect data to measure droplet velocities with the goal of making radial velocity distributions. PTV, PIV, and PSV methods are all considered. PTV requires sparse droplets in each frame with a high shutter speed to minimize motion blur. It also requires individual droplets to be able to be tracked between successive frames. An estimate is created for the average number of consecutive frames in which each individual droplet is expected to be appear for each shutter speed. This can be seen in the last column of Tables 1 and 2. 15 m/s was used as a conservative estimate of the droplet speed since this is towards the upper range of expected droplet speeds in annular flow at the RPI test facility [10-12]. PIV also requires a high shutter speed to minimize motion blur but does not involve tracking individual droplets. Another requirement is PIV requires dense droplets since it measures instantaneous velocity of entire regions for a specific frame. Few droplets per frame results in high uncertainty.

PSV is quite different since it requires high exposure and a low shutter speed to induce intentional motion blur. This method works by dividing the length of the blurred droplet by the shutter speed to estimate an instantaneous velocity for a specific droplet in a specific frame. Slower shutter speeds result in longer motion blur, which results in reduced uncertainty. A drawback with very slow shutter speeds is the increase in instances of the streaks of different droplets overlapping. Therefore, images with sparse droplets are preferred for PSV.

Initially, a PIV method is tested. This method is ruled out due to frames of droplets having a relatively low droplet fraction and not having dense droplets causing a relatively high uncertainty. Next, PTV is tested. This method is also ruled out because individual droplets do not appear in enough individual frames unless the frame rate is set to one of the highest options. This results in too large of a decrease in resolution to create meaningful results.

Finally, a PSV method is tested. Table 3 lists the minimum shutter speeds for different target motion blur streak lengths relative to median and maximum size droplet for superficial velocity values towards the middle of the RPI test facility's operational range [12]. A 5 m/s droplet speed was used in this table as a conservative estimate since this is towards the lower range of expected droplet speeds in annular flow at the RPI test facility and slower droplets cover less distance [10-12]. The minimum shutter time column helps estimate shutter speeds to test. Shutter speeds between 1/500 and 1/2,000 s are tested; however, different shutter speeds are used with different flow conditions depending on the droplet speed produced. More information about testing for the velocimetry methods is included in Chapter 5. Precise droplet size measurements are not the priority with this data but can be estimated to verify the size distributions.

*Table 3: Minimum Shutter Speed Times for Median and Maximum Droplets Traveling at 5 m/s for $j_g$ = 30 m/s and $j_f$ = 0.1 m/s [13].*

| Droplet Size | Target Streak Distance (Number of Diameters) | Distance Needed (mm) | Minimum Shutter Time (s) |
|---|---|---|---|
| Median Droplet (D = 0.2765 mm) | 5 | 1.4 | 2.77E-04 |
| | 10 | 2.8 | 5.53E-04 |
| | 20 | 5.5 | 1.11E-03 |
| Maximum Droplet (D = 0.8654 mm) | 5 | 4.3 | 8.65E-04 |
| | 10 | 8.7 | 1.73E-03 |
| | 20 | 17.3 | 3.46E-03 |

## 2.2 Camera Lens Selection

A variety of camera lenses and lens accessories are tested to find a combination that yields the theoretical magnifications needed as listed in Tables 1 and 2. Table 4 displays the tested camera attachments, encompassing macro lenses, teleconverters, and extension tubes. Despite the camera attachments having listed magnifications, these are not precise and must be tested to determine combinations for the present study. The lenses attach directly to the high-speed cameras followed by optional teleconverters and extension tubes to further increase and fine-tune magnification if desired.

*Table 4: Tested Camera Attachments.*

| | Model | Magnification Listed | Length of Attachment (cm) |
|---|---|---|---|
| Lenses | Tamron SP Di | 1:10 – 1:1 | 16.5 |
| | Venus Laowa | 1:2 – 2:1 | 9.25 |
| Teleconverters | Nikon AF-S TC-20EIII | 2x | 4.5 |
| | Tamron SP AF | 1.4x | 2 |
| Extension Tubes | Kenko | N/A | 3.6 |
| | Kenko | N/A | 2 |
| | Kenko | N/A | 1.2 |
| | Vello | N/A | 3.6 |

The cameras need to be placed in significantly different distances from the target. For maximum resolution images, the Venus Laowa lens focuses on images that are only between 2 and 6 cm from the end of the lens, depending on the magnification dial setting and if there are other attachments added. On the other hand, the Tamron SP Di allows for a much longer working distance of 20 to 35 cm depending on the magnification and if there are other attachments added for maximum resolution images. With the use of the other attachments, both lenses can reach all the desired magnifications. The Tamron lens is selected because of concerns of water droplets landing on the attachments if the Laowa lens is used due to its small working distance.

To select which teleconverters and extension tubes will be used with the Tamron lens, checkered calibration tape is used to determine the width of the image in focus for each tested configuration. The checkered calibration tape has squares that are 1 mm in width and height and is placed on a piece of transparent plastic. The camera, equipped with attachments, is turned on and directed towards the calibration tape and adjusted to the appropriate distance to achieve sharp focus on the tape as shown in Figure 5(a). Different lens, teleconverter, and optional tube extensions combinations are tested. The physical width of each configuration is measured by counting the number of checkers in a row on screen, as shown in Figure 5(b).

After experimenting with many attachment configurations, it was discovered that using the Tamron SP Di lens, the Tamron SP AF teleconverter, and a 2 cm extension tube will allow both cameras to reach target magnifications with only adjusting the magnification dial on the lens. Therefore, both cameras will be equipped with identical attachments. Table 5 shows information about the final camera and attachment configurations for both cameras to collect both size and velocity data. The only change between each configuration is slightly rotating the Tamron lens magnification dial. This table also includes measurement data for the distance from the target to

the lens and from the target and the camera sensor. These values are provided to RPI to ensure this equipment will fit in the test loop structure.

(a)

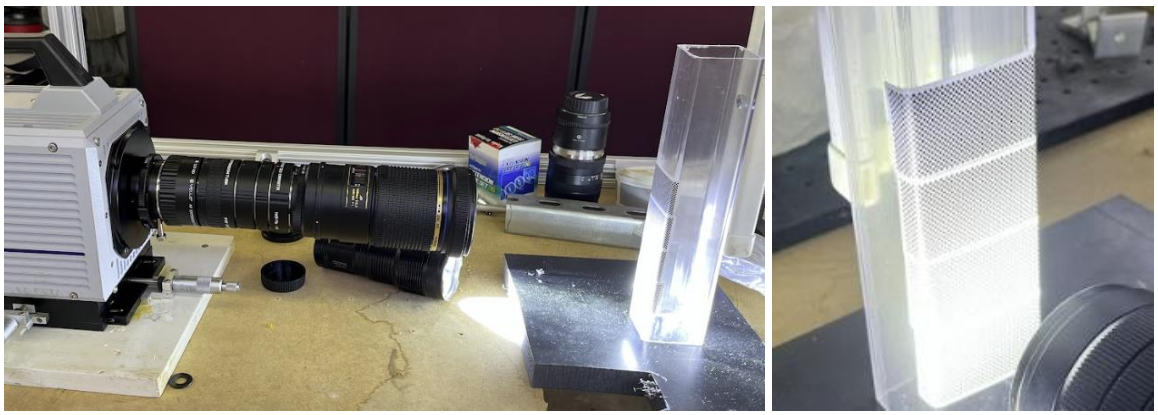

(b)

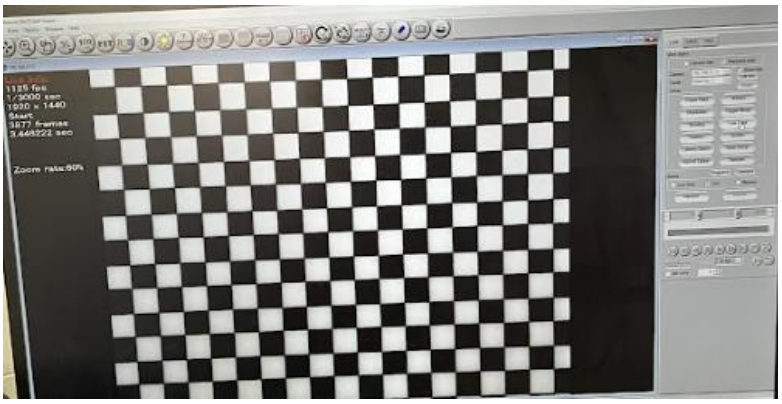

*Figure 5: Camera Attachment Magnification Testing (a) Physical Setup and (b) Camera View from Computer.*

*Table 5: Distances Required for each Final Camera Configuration.*

| **Camera** | **Lens Magnification Setting** | **Frame Rate** | **Lens to Target Distance (Working Distance)** | **Camera Sensor to Target Distance** |
|---|---|---|---|---|
| SA4 | 1:1 | 3,600 fps | 23.5 cm | 49.5 cm |
| SA6 | 1:1.1 | 1,125 fps | 24.0 cm | 50.0 cm |

The final attachment selections can be seen on the SA6 camera in Figure 6. Also pictured in this figure is a custom-made stand for the camera to keep the lens aligned vertically. The stand is made primarily from aluminum channels. Without the stand with the lens support, the camera attachments sag from their weight as seen in Figure 5(a). The camera is connected to the stand with a rigid plate. This plate is bolted into both the camera and stand through existing screw holes.

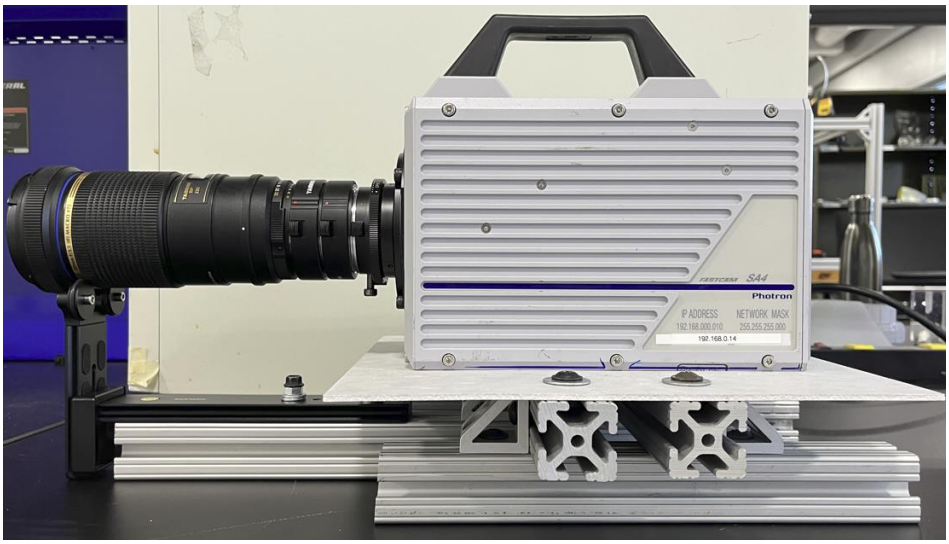


*Figure 6: Selected Camera Attachments on SA6 Camera Mounted to Custom Stand.*

## 2.3 Lighting Selection

A few different light sources are tested to find an ideal option to provide enough intensity to the camera to produce bright images that can be processed. The Nitecore TM15 light is the first light source tested and is pictured in Figure 7(a). This light source is in the form of a high-power flashlight. It is battery powered and contains an internal rechargeable battery. A benefit of this light source is that it is relatively small and easy to mount at almost any angle or direction. A downside of its battery powered power system is that the light slowly decreases in intensity when it is powered on. This decrease happens slowly over time and is hard to notice during experimental

runs. This results in significant differences in overall image brightness. For instance, the images in Figure 7(b) were taken only a few minutes apart with the same equipment and experiment configuration; however, they clearly have different brightnesses. The light source used for these images is the Nitecore TM15. Therefore, this is not a reliable light source. It is also not nearly as bright as the other light sources tested.

(a) (b)

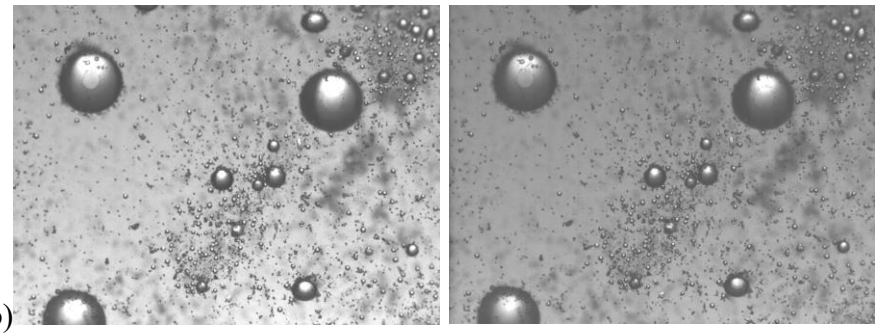

*Figure 7: (a) Nitecore TM15 Light and (b) Sample Images Captured using the TM15 Light.*

The second light source tested is the Godox VL200. This light source is powered directly by an AC power supply. Therefore, when it is turned on, the intensity is consistent. These first two sources were selected as potential options since they were already purchased for the Virginia Tech test facility prior to the current study. The Godox VL200 is the light source on the bottom of Figure 8. While the Godox VL200 is significantly brighter than the Nitecore TM15 at maximum intensity, it is still relatively dark at fast shutter speeds. To minimize motion blur, fast shutter speeds are required to collect accurate droplet size data.

A sample image of droplets taken with a shutter speed of 1/277,000 s that is illuminated by the Godox VL200 can be seen in Figure 9(a). It is hard to see any droplets. Since this image is so dark, a third light source is ordered and tested. The Godox VL200 has an illuminance of 89,000

lux at 1 m. The third tested light source is the SmallRig RC 450D, which has an illuminance of 172,000 lux at 1 m. This was brightest light source within budget. The SmallRig RC 450D is picture at the top of Figure 8.


*Figure 8: SmallRig RC 450D (Top) and Godox VL200 (Bottom) Light Sources.*

A sample image of droplets taken with a shutter speed of 1/277,000 s that is illuminated by the SmallRig RC 450D can be seen in Figure 9(b). One downside to this light source is that at its maximum brightness, the brightness is not completely consistent; however, the darker frames are still significantly brighter than the frames from experiments that utilize the Godox or Nitecore lights. These brightness fluctuations can be accounted for in the droplet identification program code through normalization. Since the SmallRig light is significantly brighter than the other options, it is used in future experimentation. The SmallRig light's brightness can also easily be adjusted directly on the light or with a smartphone application that connects via Bluetooth. This is

important because the size distribution data is collected at a much faster shutter speed, which requires significantly brighter light than the PSV data.

(a)  (b) 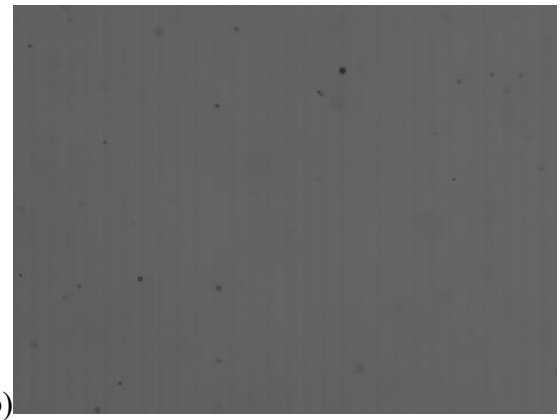

*Figure 9: Sample Images Taken with a 1/277,000 s Shutter Speed Illuminated by the (a) Godox VL200 and (b) SmallRig 450D.*

Besides the type of light source, there are a few other ways to improve the lighting in the high-speed cameras' images and thus, improve the image quality and minimize noise. One way is to position the lights as close to the droplet stream as possible to reduce the distance the photons have to travel from the light source to the camera. Light intensity decreases in proportion to the square of the distance between the light source and camera. Unfortunately, the position of the camera relative to the droplet stream is selected based on the desired image resolution and physical distance imaged so the camera can not be moved as close to the droplet stream as the light source.

A second key way to improve the lighting in the high-speed cameras' is to ensure that the center of each light source is centered both horizontally and vertically with the center of each camera. The cameras will be placed on the direct opposite side of the droplet stream as the light

sources so they will be centered horizontally already. On the other hand, additional equipment is used to ensure the cameras and light sources are centered vertically. Height adjustable platforms are used with the lights. Platforms are used with the lights instead of the camera since the lights are significantly less heavy.

The adjustable platforms with the optional mounting bases that were included with the lights can be seen in Figure 10(a). The mounting bases were connected with a bolt after a hole was drilled in the middle of each adjustable platform, which can be seen in Figure 10(b). Additionally, images of the lights attached to the mounting base and platforms can be seen in Figure 10(c). This figure also displays the maximum and minimum heights that the adjustable platforms can reach. Having vertical height flexibility is important since the camera and lights have different heights. Additionally, the RPI test facility was not designed to ensure that the lights and cameras are centered vertically with high precision.

A final piece of equipment that is used with the lights is diffusor paper attached to an acrylic block. This is placed in front of the light. The diffusor paper is used to make the lighting uniform and protect the camera from direct bright light, which can potentially damage the sensor. Each light will have one of these blocks with acrylic paper placed in front of them when the light is turned on. The acrylic block with diffusor paper in front of one of the SmallRig lights can be seen in Figure 11.

All of the pieces of equipment that are brought to the RPI test loop are listed in Table 6. The last two pieces of equipment, the calibration target and linear micrometer, are discussed in Chapter 3.

(a)

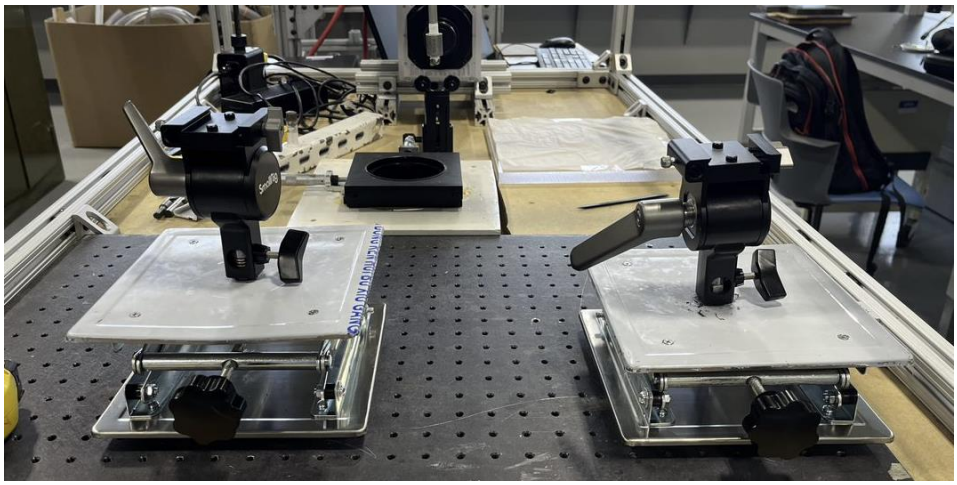

(b)

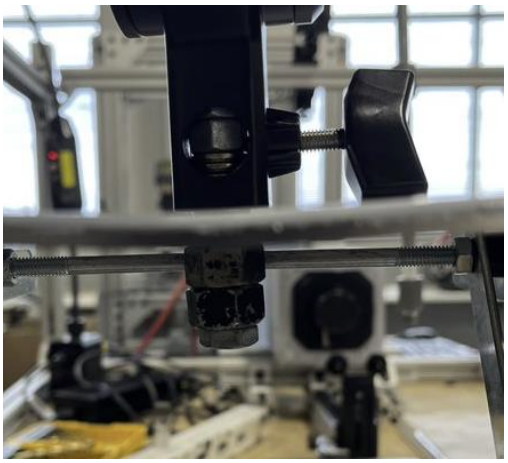

(c)

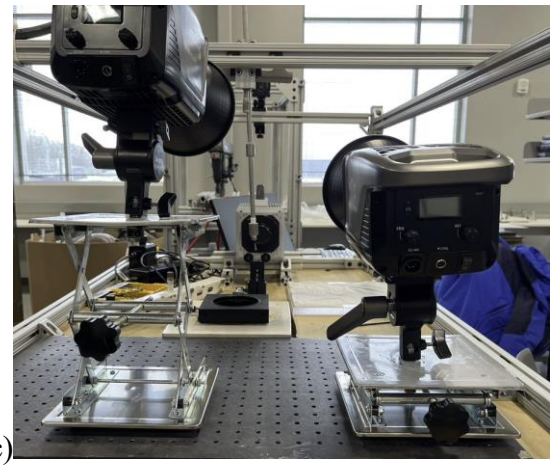

*Figure 10: (a) Adjustable Height Platforms with Camera Mounting Base, (b) Bolt Used to Connect to Platforms, and (c) Top and Bottom Range of Adjustable Height Platform.*

*Figure 11: Acrylic Block with Diffusor Paper in Front of Light.*

*Table 6: Final List of Equipment Brought to RPI.*

| Part | Quantity |
|---|---|
| Photron Fastcam SA4 | 1 |
| Photron Fastcam SA6 | 1 |
| Tamron SP Di Lens | 2 |
| Tamron SP AF Teleconverter | 2 |
| Kenko 2 cm Extension Tube | 2 |
| SmallRig RC 450D Monolight | 2 |
| Camera Mount | 2 |
| Adjustable Light Stand | 2 |
| Acrylic Blocks with Diffusor Paper | 2 |
| Calibration Target | 1 |
| Linear Micrometer | 1 |

# Chapter 3

# 3. Depth of Field Testing and Camera Calibration

A system for calibrating the cameras each test at the test facility is researched and experimented with for two key purposes. First, developing a calibration method allows for verification that the lighting conditions did not change significantly during the duration of testing. Second, it allows for differentiating between in-focus and out-of-focus droplets. This is important because droplets farther from the camera's focal plane appear larger than they physically are, which leads to more uncertainty in the results.

## 3.1 Calibration Procedure

A calibration method is used that is similar to calibration methods developed in the past to determine the focal plane of particles and bubbles [28,31]. Small particles are used instead of actual water droplets since individual particles can remain in the same vertical and horizontal position relative to the camera during calibration imaging. The particles are taped or glued to a transparent acrylic block. The plate with the particles only moves along the depth axis, getting closer to or farther away from the camera, to determine focal plane behavior.

During the calibration process, the calibration target is initially placed so its particles are in focus and centered in the imaging frame with the high-speed camera turned on and connected to the computer. An estimation for the in-focus distance is made by using the live camera feed. A

linear micrometer, as seen in Figure 12, is beneath the calibration target to allow for precise movements of the target. The micrometer allows for two degrees of movement and has markings on each dial corresponding to 10 μm of movement. One dial is used only to initially center the target in the imaging frame. The other dial is used to initially move to target in-focus and during the calibration process to change the distance from the camera to the calibration target. One of the SmallRig lights is turned on and placed behind diffusor paper on the side of the calibration target opposite the high-speed camera. The Photron Fastcam SA6 is used in testing different iterations of the calibration target due to its higher resolution. Both cameras use the same calibration procedure when collecting droplet data. The same camera attachments that are used when collecting droplet data are also used during calibration. A schematic of the equipment used during calibration is seen in Figure 13.

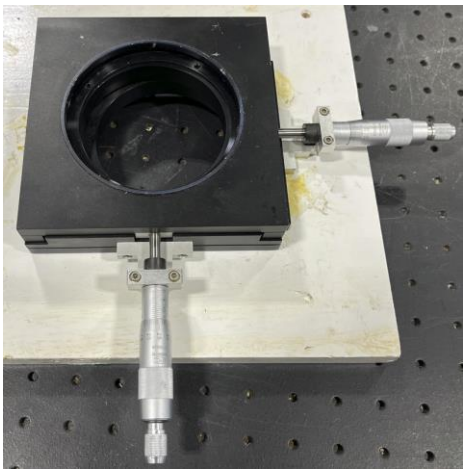

*Figure 12: Linear 2-Axis Micrometer Placed Beneath Calibration Target during Calibration Procedure.*

Once the equipment is setup and the calibration target is in-focus, the target is moved towards the camera 1 mm and an image is taken. Then, it is moved 50 μm away from the camera

a total of 40 times. Images are taken after each 50 μm movement for a total of 41 images spanning 2 mm. These images are saved to be analyzed in the depth-of-field calibration program. When droplet data is collected, the calibration process occurs before and after data collection. The two sets of data are compared to ensure they are not significantly different. If they are not significantly different, the droplet data is used, and the data from the calibration images are also used to determine the focal plane distance.

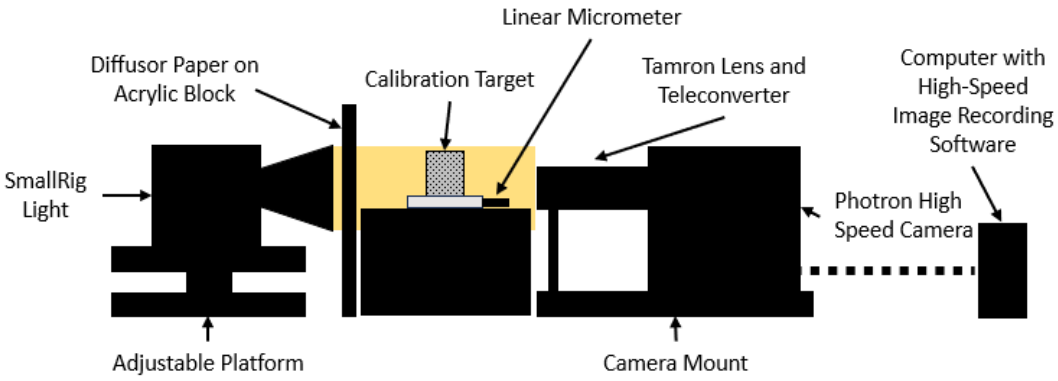


*Figure 13: Schematic of Equipment for Depth-of-Field Calibration.*

## 3.2 Depth-of-Field Calibration Program

A depth-of-field Matlab algorithm is developed to analyze data from calibration testing. The algorithm starts with users entering the coordinates of the particles to be analyzed. A random mixture of particles in different areas of the test section and of different sizes are selected. Additionally, particles near imperfections in the calibration target, such as glue smudges or air bubbles, are not selected.

After particles are located and images are read by the program, data about the intensity and intensity gradient of the pixels in the grayscale images are recorded for each particle. The intensity method compares how dark specific pixels in the particles are as the distance changes. The

intensity gradient method uses calculus to compare how large of a difference there is in pixel brightness between the edge of each analyzed particle and the background. This data is plotted with the distance from the estimated focal center as the x-axis. Figure 14 shows an example of particle intensity gradient data plotted. The subsequent plots in Figures 15-17 show the same dataset throughout the processing method.

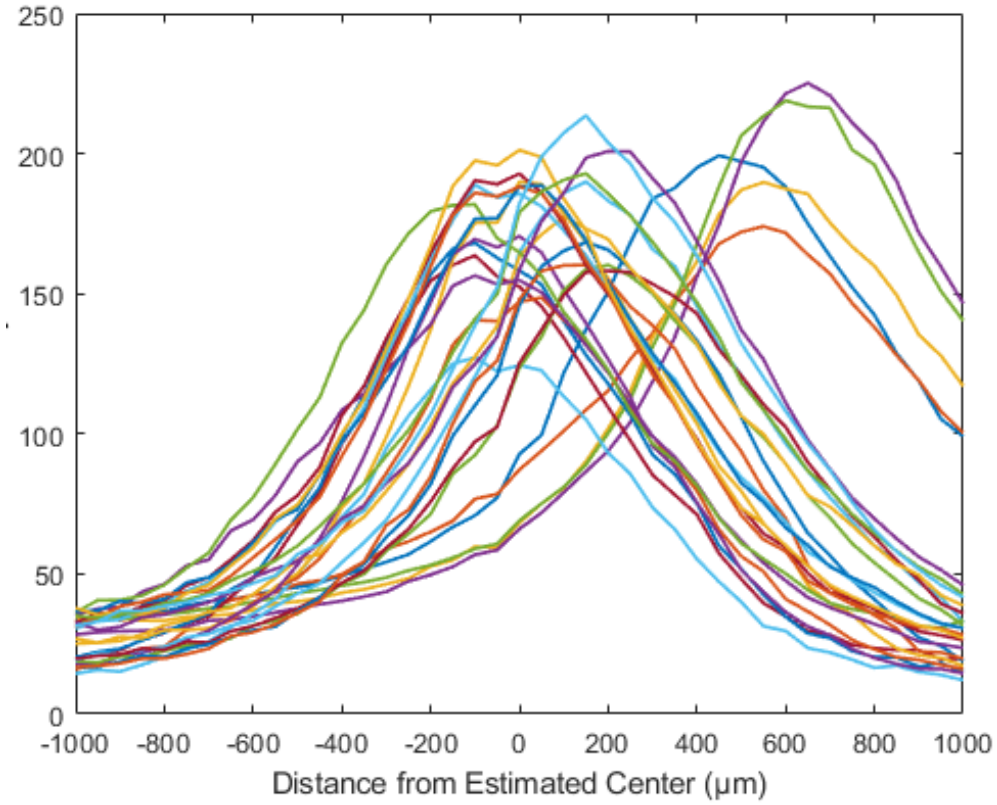


*Figure 14: Sample Absolute Particle Intensity Gradient Plot from a Calibration Test.*

Next, the program normalizes the intensity and intensity gradient data as shown in Figure 15 for particle intensity gradient data from the sample test. This step accounts for inconsistencies in light intensity that reach each particle and for particle intensity gradient differences between

different sized particles. The data is then reshaped to allow for all points to reach maximum values at a zero point on the x-axis, corresponding to the center of the focal plane as shown in Figure 16 for the sample test. This step accounts for different size particles. Larger particles will appear in focus when the calibration target is farther from the camera since the particles extend further from the surface of the acrylic block.

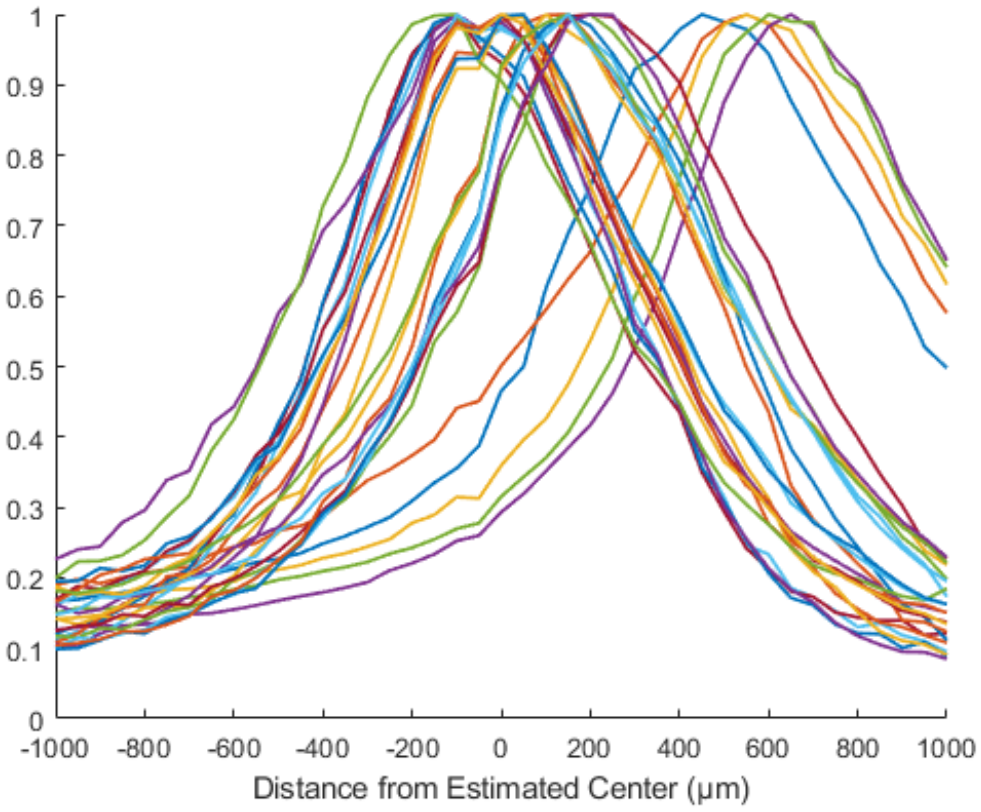


*Figure 15: Sample Normalized Particle Intensity Gradient Plot from a Calibration Test.*

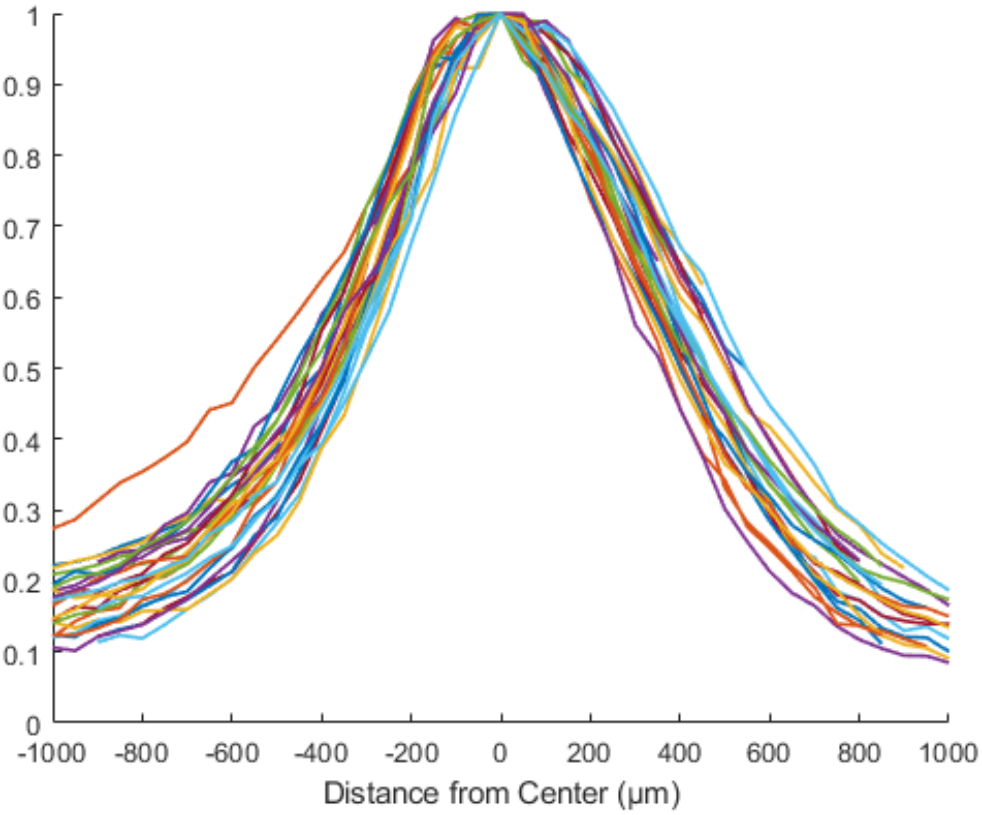


*Figure 16: Sample Centered Normalized Particle Intensity Gradient Plot from a Calibration Test.*

Statistical values such as the mean and standard deviation at different locations away from the middle of the focal plane are recorded and plotted as shown for the sample test in Figure 17. Potential particle intensity gradient thresholds are also plotted. This helps analyze the slope of intensity and intensity gradient behavior, which helps determine thresholds to use in the droplet identification program to filter out out-of-focus droplets as discussed in Chapter 4. A higher threshold will have less uncertainty in droplet size, but a lower threshold will result in more data processed. A higher threshold will also correlate with a more narrow focal plane depth.

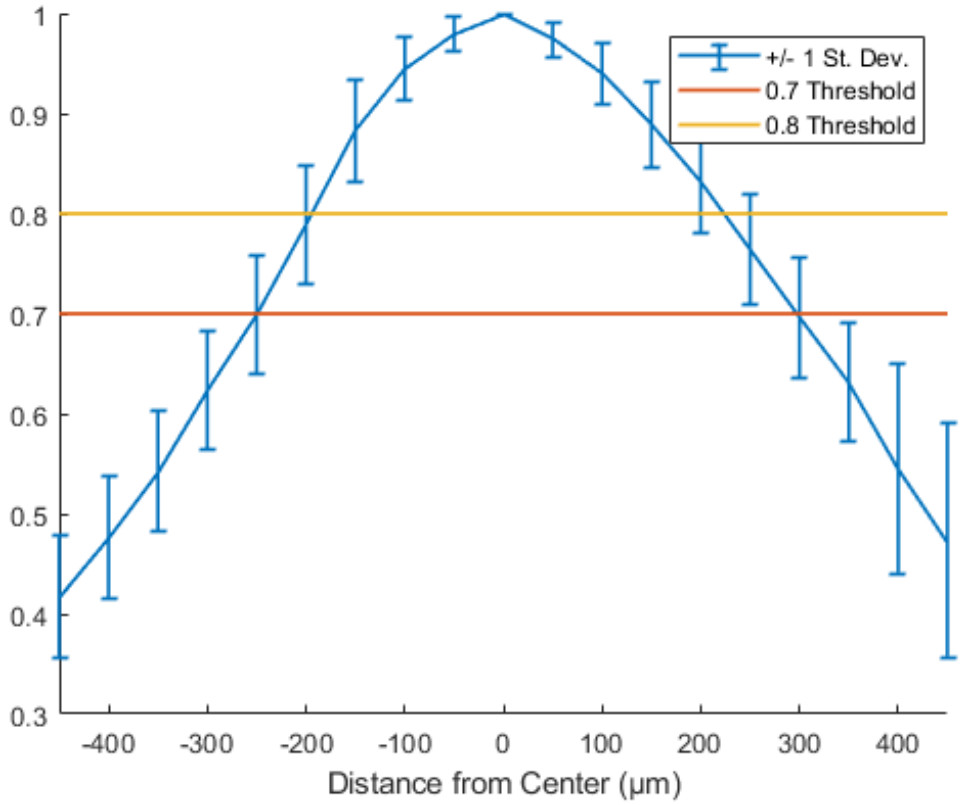


*Figure 17: Sample Mean Normalized Particle Intensity Gradient Plot with Potential Thresholds.*

## 3.3 Calibration Target Creation

For the calibration target, stationary particles with a similar index of refraction to water are used to represent droplets. Since the acrylic block they are attached to is clear, this setup sufficiently simulates how light interacts with water droplets in air. Initially the particles tested are all 50 μm in diameter randomly sprinkled and then taped to an acrylic plate. An image in-focus from the SA6 camera of the plate is shown in Figure 18, with randomly selected particles for analysis with a blue surrounding box.

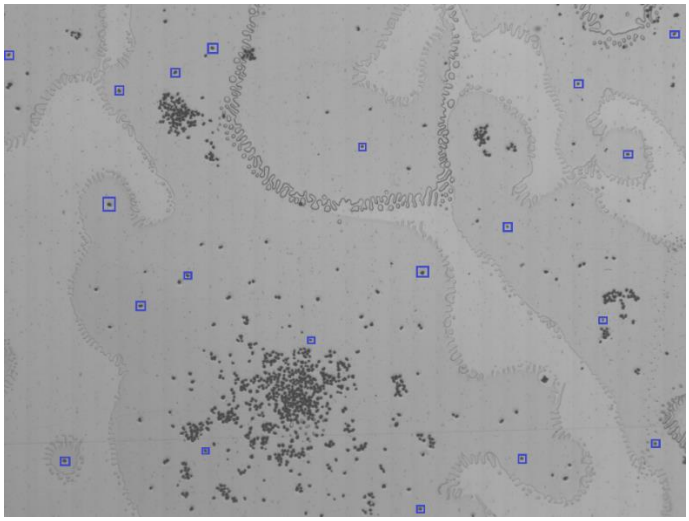

*Figure 18: Image of Particles Captured with High-Speed Imaging System from First Calibration Test with Randomly Selected Particles for Calibration Program.*

A total of 41 images of this test section are collected as described in the calibration procedure. A comparison between the in-focus image and an image when the camera was moved 1,000 μm in one direction is shown in Figure 19. The images are analyzed in the depth-of-field program to study the focal plane behavior of the initial calibration target iteration. Figure 20 shows each of the particles with a blue box from Figure 18 plotted individually. As shown in Figure 20, the particle intensity gradient method resulted in graphs with significantly less noise than the particle intensity method. Therefore, this method is used in future analyses.

a) 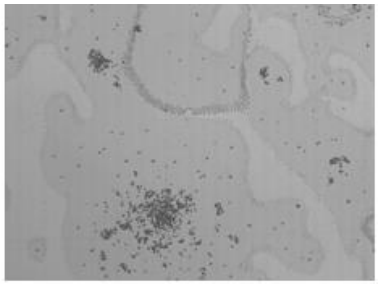 b) 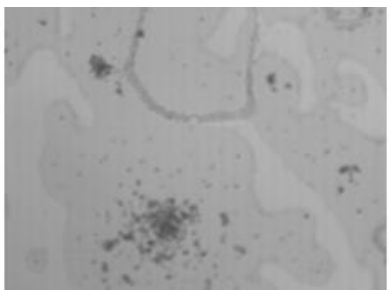

*Figure 19: Comparison of Sample Images when Target is (a) In-Focus and (b) 1,000 μm from Focal Plane from First Calibration Target.*

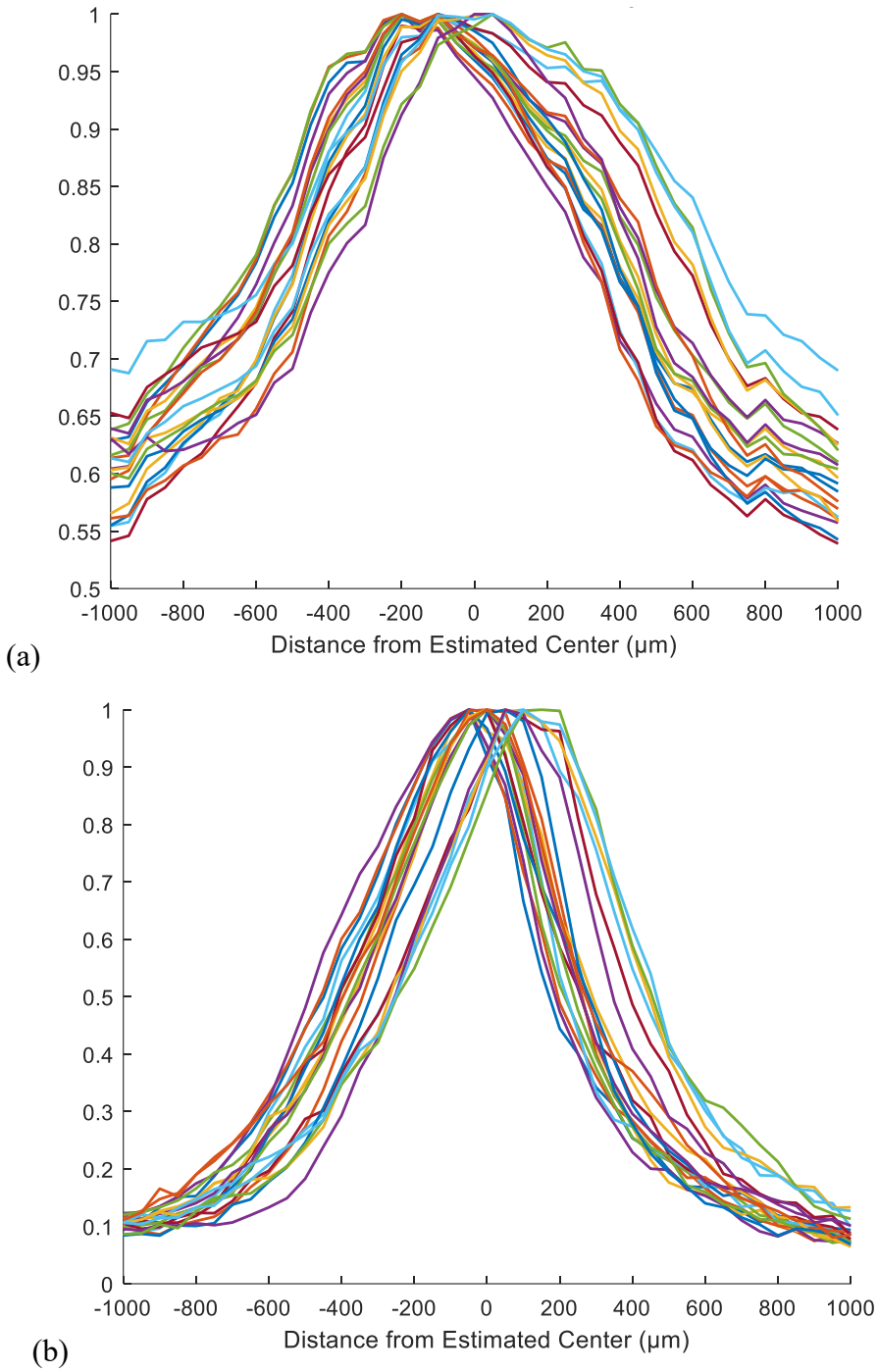


*Figure 20: (a) Normalized Particle Intensity and (b) Normalized Particle Intensity Gradient as Distance from Camera to Calibration Target Changes from First Calibration Target.*

It can be noticed that there is variation in the peak locations of the individual graphs. Theoretically, each line should peak at the same location since each particle is the same size and extend the same distance off of the calibration target, which is parallel to the camera lens. It is hypothesized that this inconsistency is a result of the lens not being completely horizontal due to having no support and the calibration plate not being perfectly parallel with the lens. Further analysis is conducted to study this discrepancy in peak location.

The testing image from the first calibration target iteration is divided into four quadrants, as shown in Figure 21. A new normalized particle intensity gradient graph with averages of each quadrant is created and shown in Figure 22. A few conclusions can be made from this analysis. First, while the red and blue lines on the graph, corresponding to the two top quadrants, have similar behavior and peak at the same location. Similarly, the yellow and purple lines, corresponding to the bottom two quadrants, also have similar behavior and peak at similar locations. However, the lines corresponding to the lower quadrants are shifted noticeably leftwards of the upper quadrants. Therefore, it is likely that the lens not being perfectly horizontal is causing an effect. This is addressed in future testing by the inclusion of a camera mount that is displayed in Figure 6 but was not part of the setup during the first calibration target iteration testing. The discrepancies from leftward quadrants against rightward quadrants is less significant and is accounted for by the calibration program's centering step.

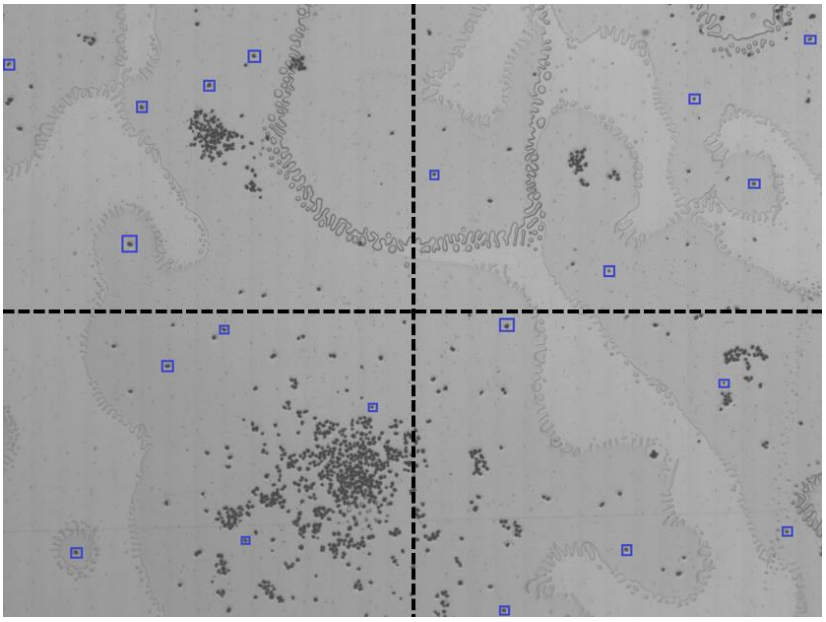

*Figure 21: Calibration Image from First Calibration Target Divided into Quadrants.*

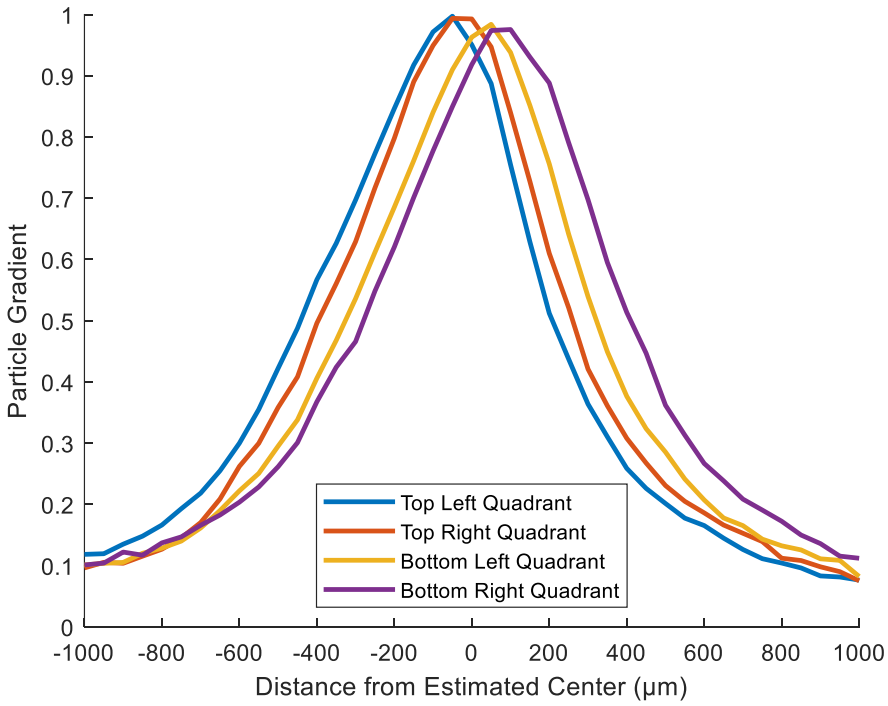


*Figure 22: Normalized Particle Gradient with Quadrant Averages from First Calibration Target.*

A second calibration test is conducted with improvements from the first test. First, a much larger variety of particle sizes are used to simulate more of the estimated droplet sizes that will exist in the test loop according to the droplet size distribution model proposed by Kataoka et al. [13]. Particles with diameters of 50, 150, 300, 550, and 1600 μm are now included. The particles are glass and have an index of refraction of 1.5 [32]. This is close to the index of refraction of water, 1.33. The larger particles cause light to be refracted through the particles unlike the 50 μm that only experience scattering [33]. All the particles tested are shown in Figure 23(a). The particles are all taped on the acrylic plate. An image of the particles captured by the high-speed camera while in-focus are shown in Figure 23(b). Additionally, the camera mount with lens support is used in this and all future iterations.

a) 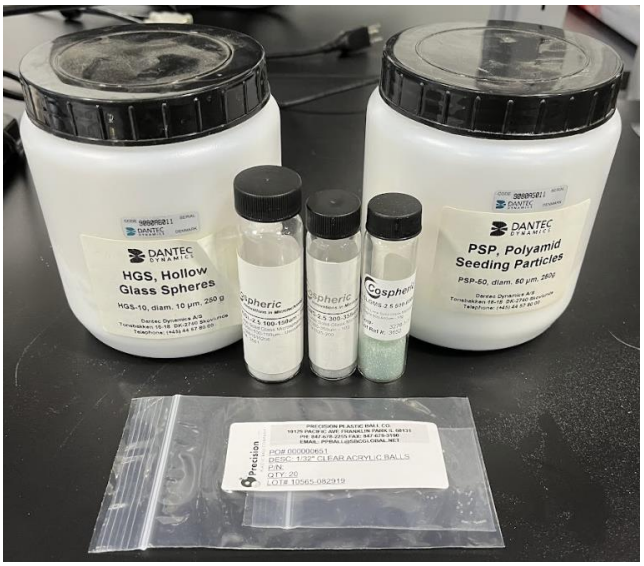

b) 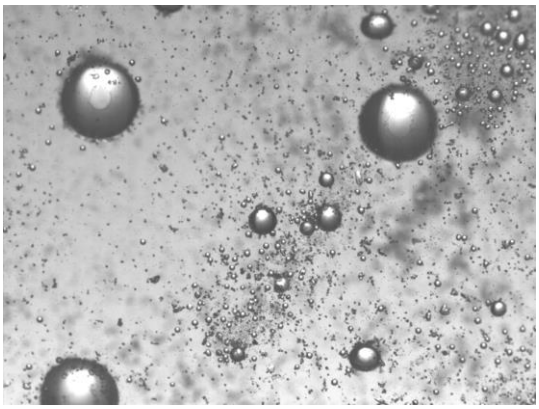

*Figure 23: Particles used in Second Calibration Target Iteration.*

The second calibration test also led to some useful conclusions that are used in future tests. First, it validated that the new camera mount system removes vertical inconsistencies. Second, it is hard to isolate individual large particles in the computer analysis due to small particles in contact with big particles. In the future, fewer particles will be placed, and the small particles will not contact the large particles. Third, the lighting source dimmed slightly during the experiment, which caused a significant drop on the gradient graph around the -100 µm distance. This can be clearly seen in Figure 24, which analyzes four of the 150 µm particles, around the -100 µm location. This test used the TM15 light and demonstrated the need for an upgrade to the SmallRig light source.

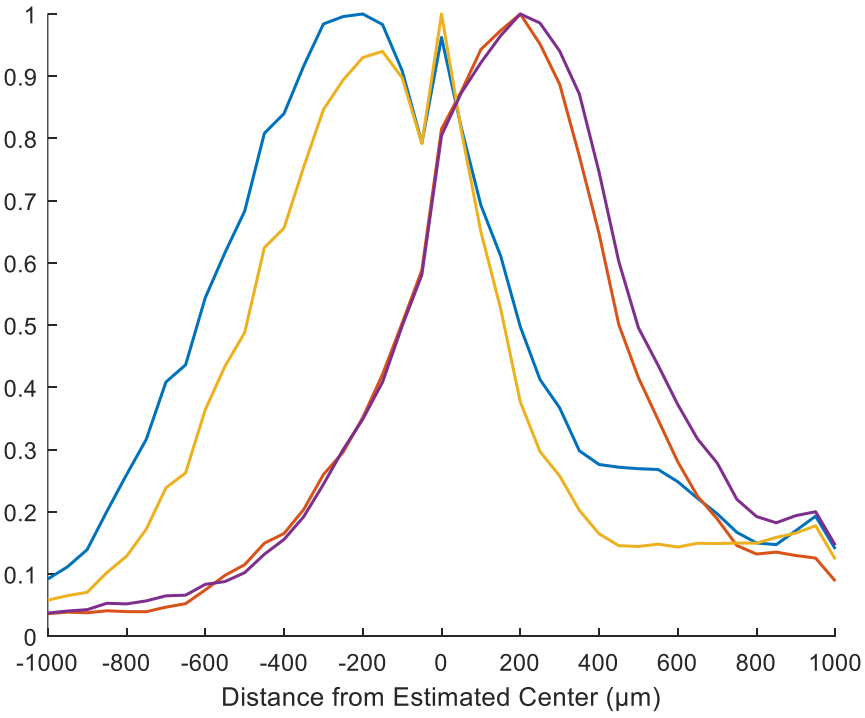


*Figure 24: Normalized Particle Gradient of Four 150 µm Particles with Clear Drop in Intensity Gradient at -100µm on Second Calibration Target.*

A third calibration test is conducted using the results from the second test. First, fewer particles are used and the larger particles are isolated. Particles with diameters of 50, 150, 300, 550, and 1600 μm are included again. The new acrylic plate with taped particles can be seen in Figure 25, both from an image using a cell phone camera and one from the high-speed cameras. Second, a translucent plate that is not completely transparent is tested to see if it led to more uniform lighting.

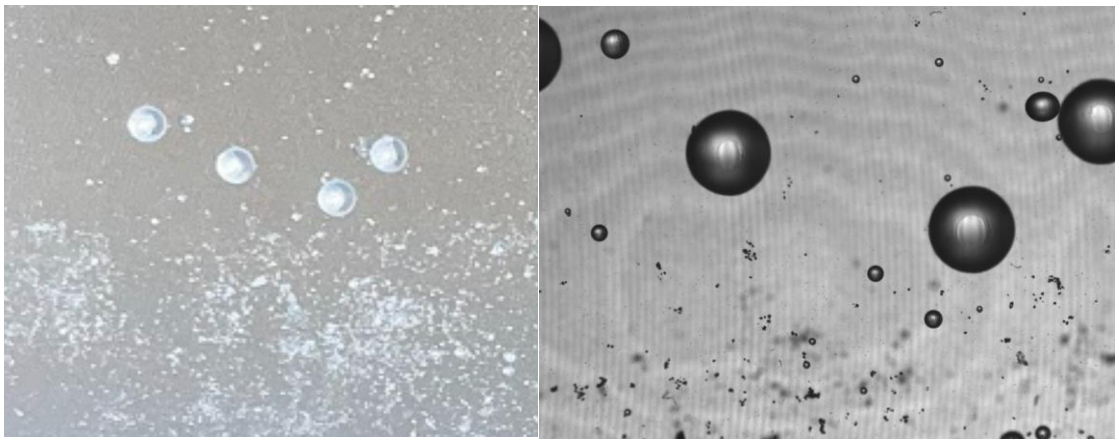

*Figure 25: Particles Used in Third Calibration Test from a Cell Phone Camera (left) and the SA6 High-Speed Camera (right).*

The results of the third calibration test lead to more useful insights. First, there is an increase at the right part of the intensity gradient curve, as seen in Figure 26. This is due to a pattern on the translucent block coming into focus so this type of acrylic will not be used in the future. Second, there is a secondary peak for some particles. This is a result of a small air bubble on the larger particles coming into focus. In the future, the larger particles will be glued to the acrylic, while the smaller particles will still be taped.

A fourth calibration target is created based on the results from analyzing the third target. To avoid air bubbles, all particles are glued to the acrylic block. A thin layer of glue is spread on a

portion of the block and then particles are carefully placed on the glued area. Particles with diameters of 50, 150, 300, 550, and 1600 µm are included again. The 1600 µm particles are large enough to be placed individually by using tweezers. This allows for placement away from areas where the other particles are sprinkled. A transparent block is used similar to the first two iterations of the target. The fourth target is pictured in Figure 27.

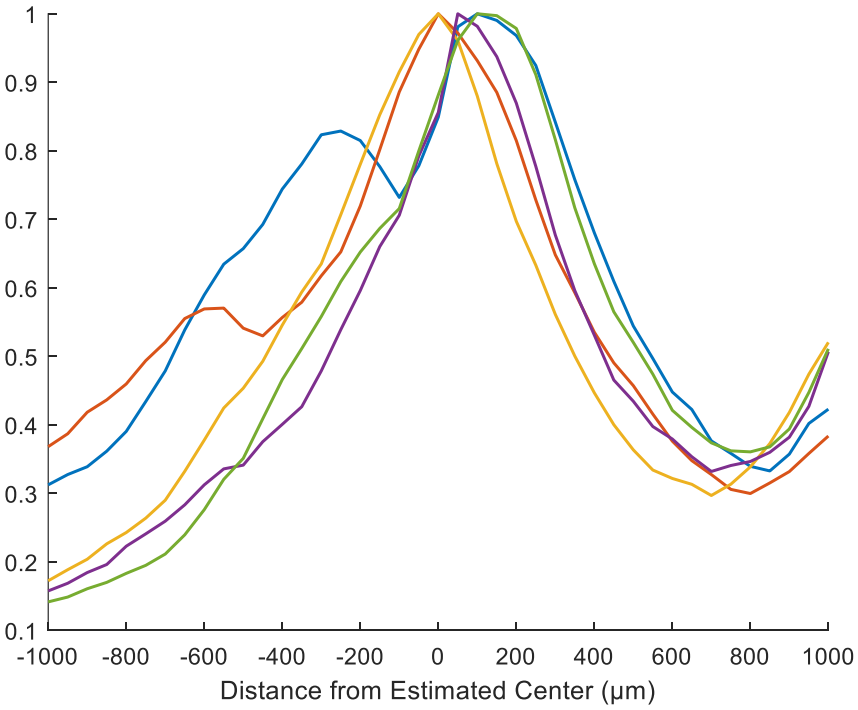


*Figure 26: Normalized Particle Gradient of Randomly Selected 300-600 µm Particles on Third Calibration Target.*

A few key conclusions are made from the results from the calibration testing with the fourth iteration of the calibration target. Just from looking at the images, it is observed that the layer of glue causes the background of the images to change color. This can be clearly seen in Figure 28, which shows the edge of the region of the target where glued is applied next to bare surface of the

acrylic. This causes the target to no longer be transparent, which is a worse replication of the background of actual droplet images.

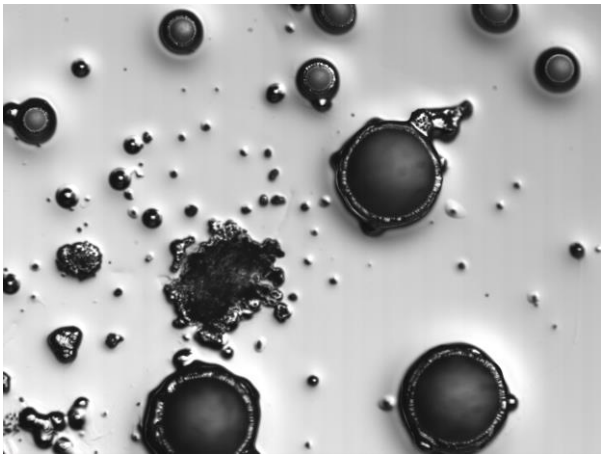

*Figure 27: Particles Glued on Fourth Calibration Target Iteration.*

*Figure 28: Border of Glued Region of Fourth Calibration Target.*

Analysis in Matlab leads to more conclusions from this target iteration. The smaller particles yielded desirable results. For instance, Figure 29(a) shows that the 50 μm particles all have similar results with one intensity gradient peak. On the other hand, the larger particles did not

perform well. Figure 29(b) shows that the 1.6 mm particles experience multiple intensity gradient peaks. This is due to the air bubbles that formed in the glue surrounding the large particles, as seen in Figure 27. This provides a second reason against using layer of glue beneath the particles.

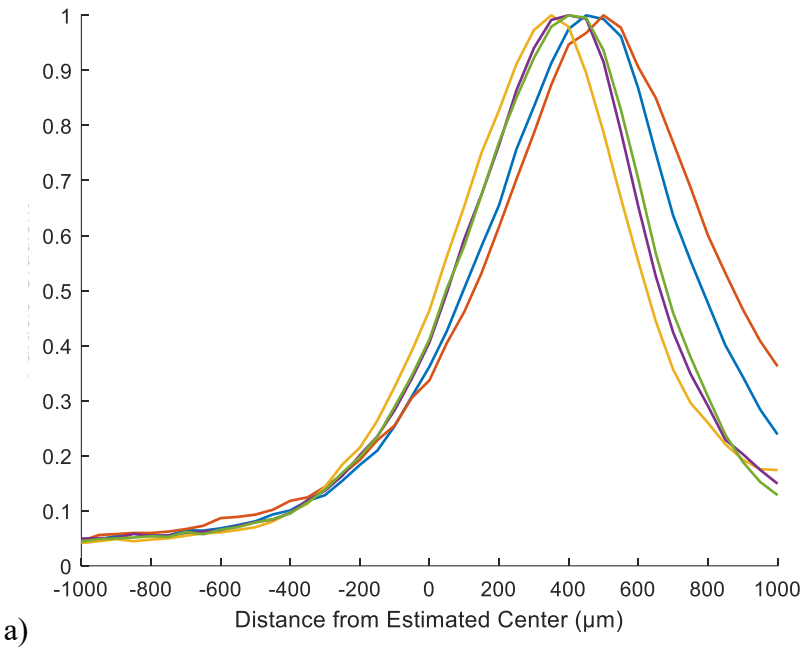


a)

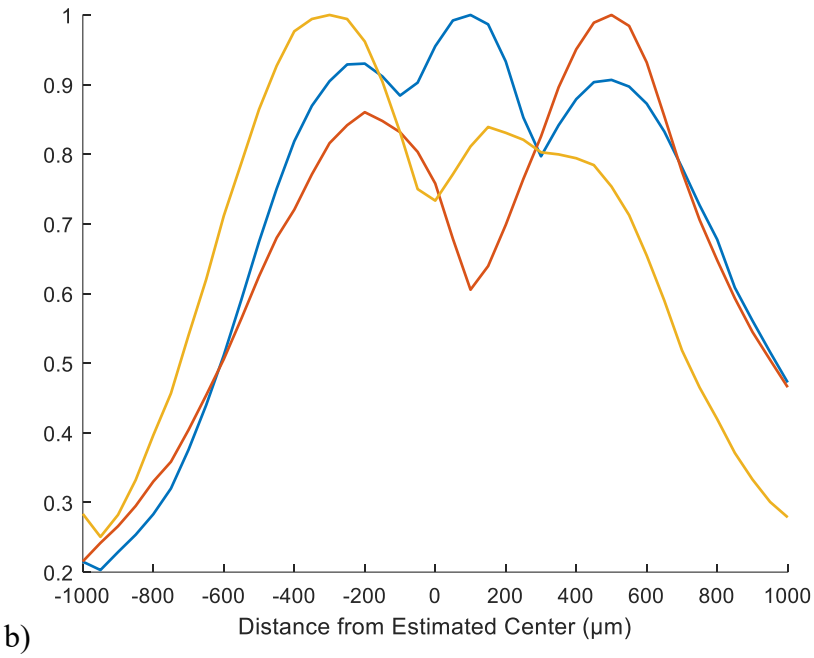


b)

*Figure 29: Normalized Particle Intensity Gradient for (a) Small 50 µm Particles and (b) Large 1.6 mm Particles on Fourth Calibration Target.*

A fifth calibration target is created using the insight gained from previous iterations. A layer of glue is avoided. Since the small particles did not have any noticeable air bubbles in calibration target iterations that used tape, the fifth target uses tape above the small particles, 50 and 150 µm. The large 1.6 mm particles are carefully dipped in glue and placed on the target by using tweezers. This ensures that glue does not appear around the large particles and form small air bubbles, which skew the calibration data. The 300 and 550 µm particles are not used because they are too small to be picked up by tweezers but too large to be placed beneath tape without air bubbles. The fifth calibration target is shown in Figure 30.

(a) 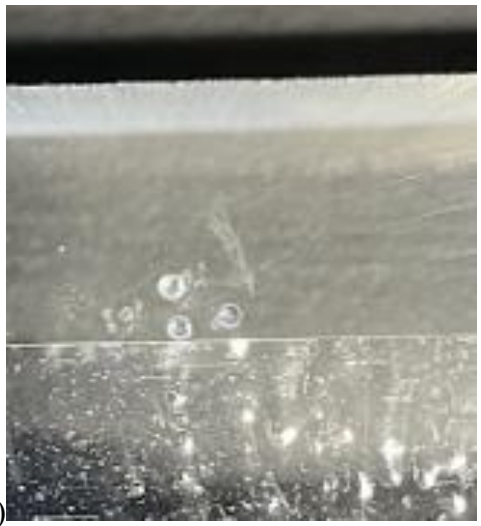 (b) 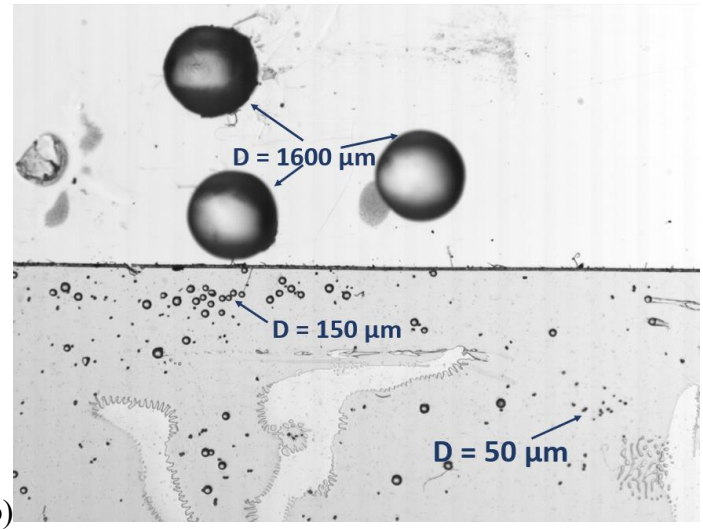


*Figure 30: Particles in Final Calibration Target (a) from a Cell Phone Camera (b) and the SA6 High-Speed Camera.*

Analysis of the fifth calibration target produces promising results. Regions of the 1,600 µm particles are analyzed rather than the entire particles to avoid small glue smudges and other imperfections in the surrounding areas. The regions that are selected for analysis in the large

particles on this calibration target are shown in Figure 31. Figure 32 shows the intensity gradient plot for a random selection of the 50 and 150 particles and the regions from Figure 31. This plot shows that each tested particle experiences one clear peak. Additionally, the 50 and 150 μm particles experience their peaks in a significantly different location than the large particles as expected. This is a result of the large particles appearing closer to the camera since they come farther off of the calibration target. This effect is also observed for the 50 and 150 μm particles to a smaller extent accounting for some of the variation in peak location for the smaller particles.

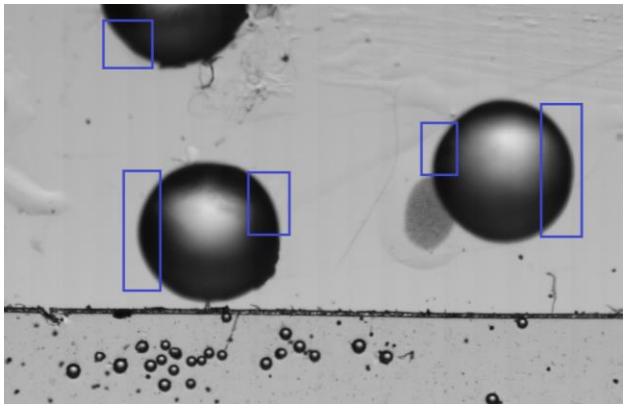

*Figure 31: Regions Analyzed of 1,600 μm Particles in Calibration Program.*

The differences in distance of peak location of intensity gradient for each particle due to particle size difference is accounted for by centering all the peak locations in Figure 33. This plot shows that the slopes of the intensity gradient plots of the different size particles are very similar. It can be concluded that intensity gradient behavior is independent of particle size. These results also provide evidence that the fifth calibration target works well with the calibration program. This target will be used in future droplet testing.

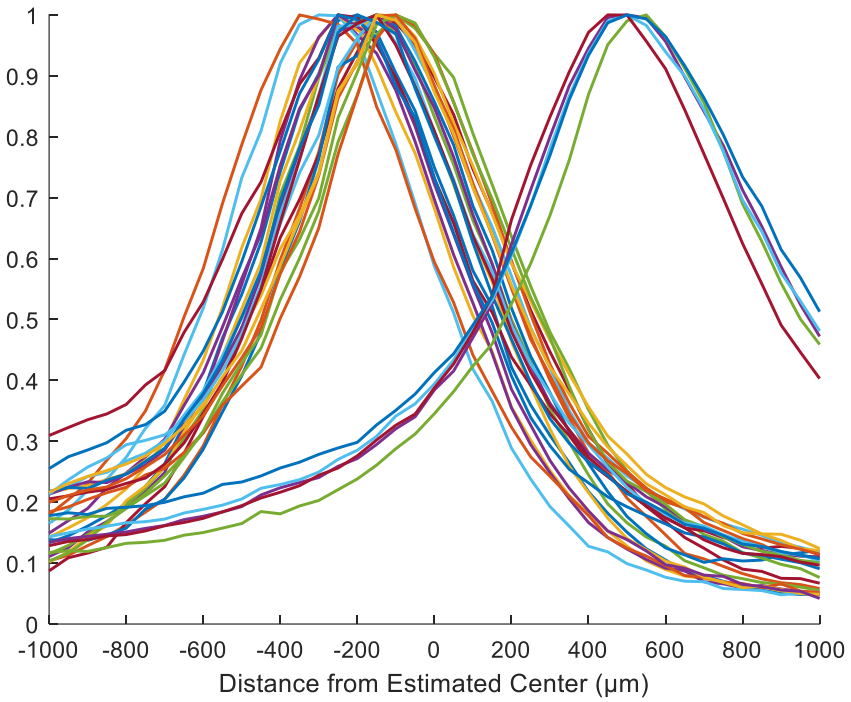


*Figure 32: Normalized Intensity Gradient for Fifth Calibration Target.*

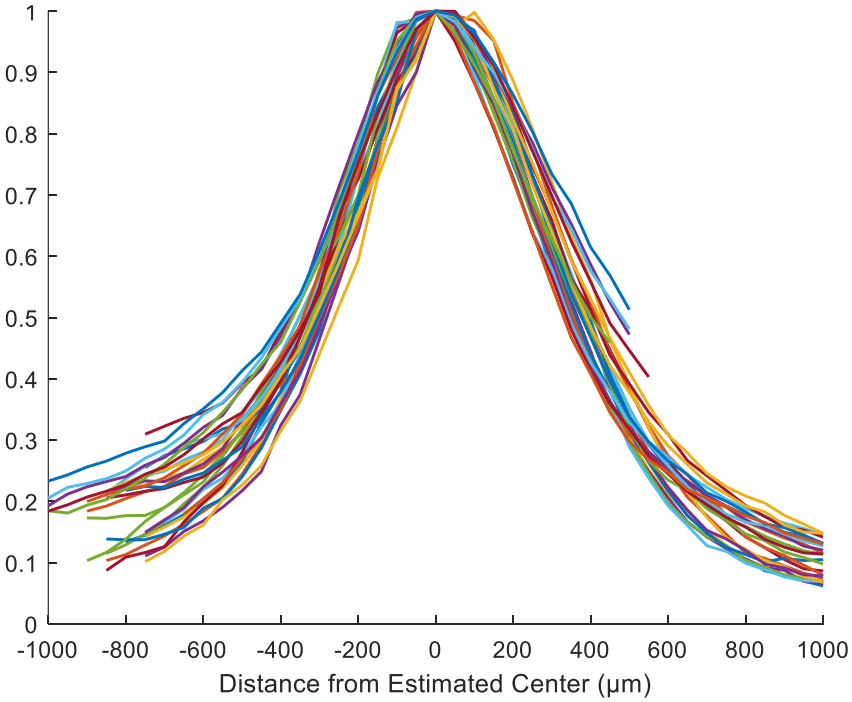


*Figure 33: Centered Normalized Intensity Gradient for Fifth Calibration Target.*

Figure 34 shows the mean values of the centered particle intensity gradient plots with standard deviations and two potential particle gradient thresholds. If this data were collected for actual droplet testing, these thresholds could be used in the droplet identification program to filter out droplets that are not in the focal plane. The 0.7 threshold would correspond to a focal plane of about 400 µm and the 0.8 threshold would correspond to a focal plane of about 300 µm.

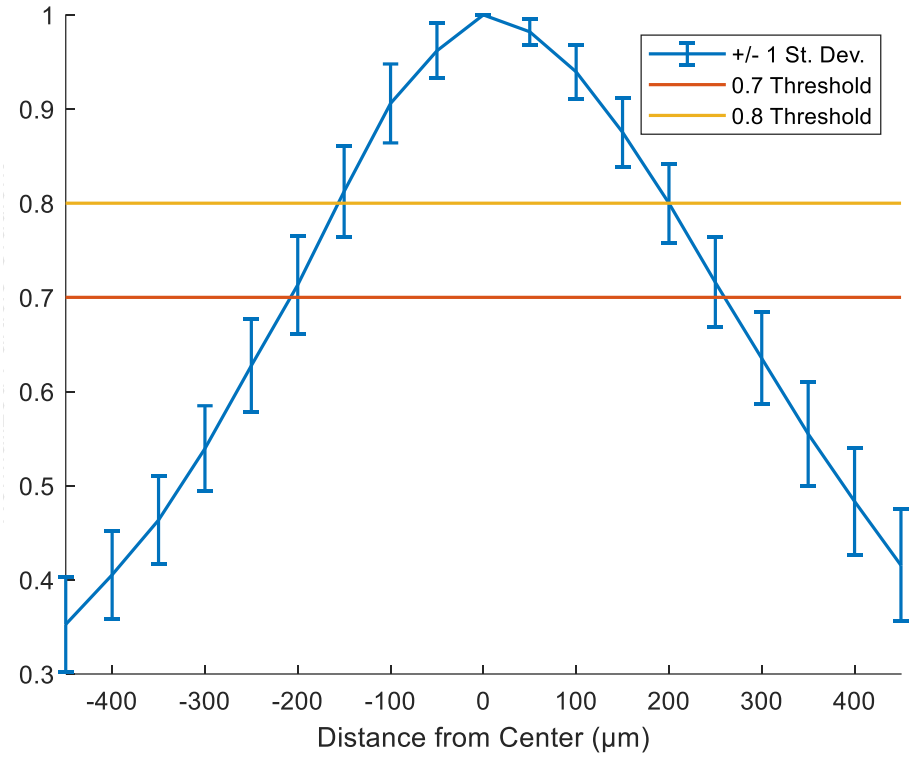


*Figure 34: Mean Normalized Particle Gradient for Fifth Calibration Target Testing.*

## 3.4 Shutter Speed Effect on Depth of Field Calibration

Previous experimentation to analyze and develop the depth of field calibration target used shutter speeds of 1/1000 second; however, actual experimentation with water droplets uses

significantly faster shutter speeds up to 1/367,000 second. These faster shutter speeds lead to darker images since less light is able to reach the lens per frame recorded. Since the Matlab codes used to analyze the images from depth of field experiments use pixel intensity gradient data that is later normalized, it was hypothesized that the depth of field calibration results will be independent of shutter speed besides a reduction in noise if slower shutter speeds are used since more light can enter the lens. A small experiment is then conducted to test this hypothesis.

The SA6 camera is setup identical to previous depth of field experiments with the final calibration target on the linear micrometer stage. Two shutter speeds were selected to compare the change in normalized particle gradient of different particles on the plane for shutter speeds of 1/102,000 and 1/277,000 seconds. In focus images for both of these speeds are shown in Figure 35. Figure 36 shows the small particles and regions of the large particles that are analyzed in this experiment for both shutter speeds.

(a) 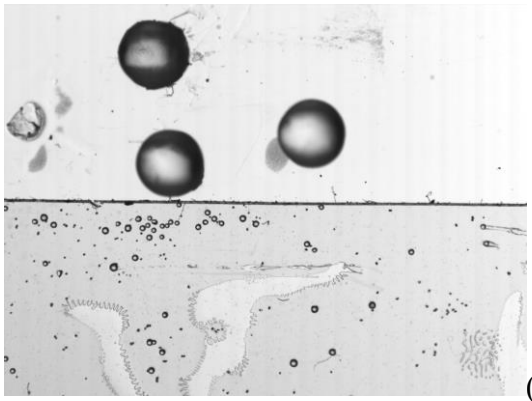 (b) 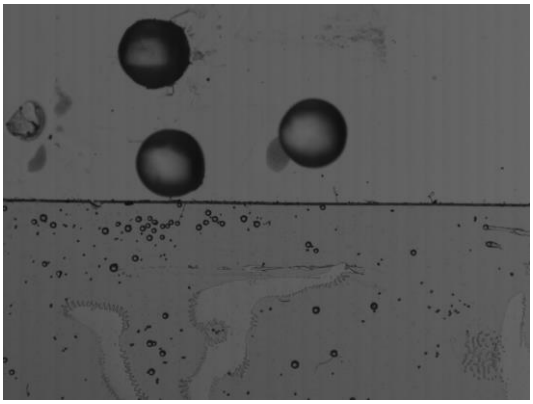

*Figure 35: (a) In-Focus Image at 1/102,000 s Shutter Speed and (b) In-Focus Image at 1/277,000 s Shutter Speed.*

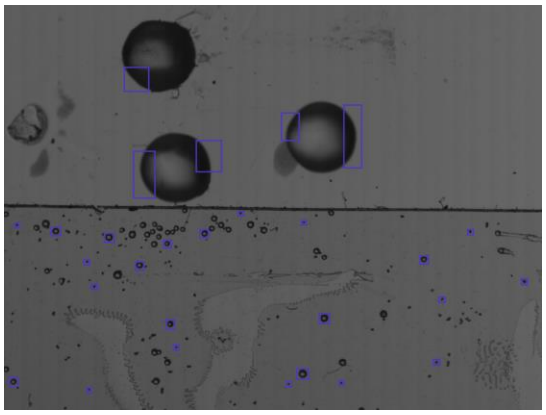

*Figure 36: Regions Tested in Shutter Speed Comparison Experiment.*

The results of this experiment support the initial hypothesis. Similar to previous depth of field data analysis, a plot was created to display the normalized particle gradient for each tested region from Figure 36. This time, each region was plotted twice, for each of the two tested shutter speeds. Figure 37 displays this plot, with the images taken at 1/277,000 second shutter speed in red and images taken at 1/102,000 second shutter speed in blue. As shown on the graph, the data for both shutter speeds is similar. They both have similar slopes throughout the plot as well as similar spreads and centers. Therefore, it will be safe to use slower shutter speeds moving forward for camera calibration, despite the actual droplet images being taken with faster shutter speeds.

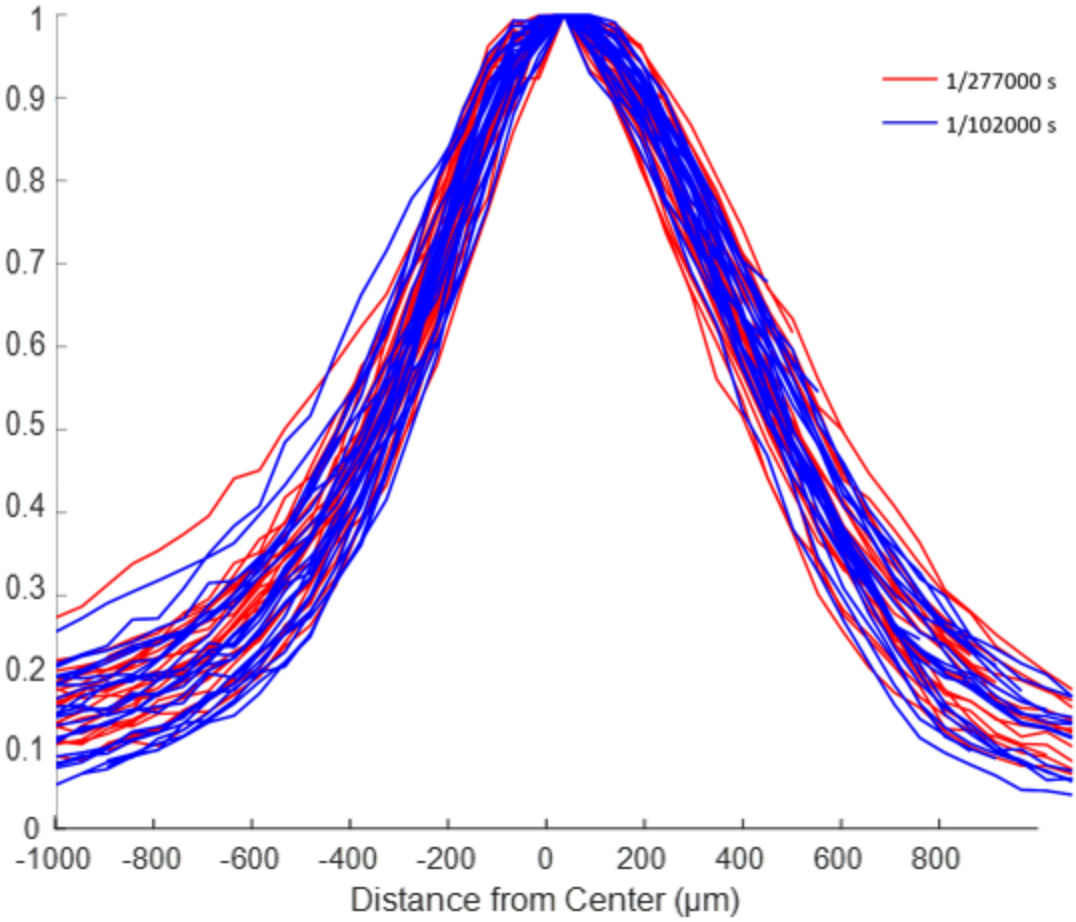


*Figure 37: Normalized Intensity Gradient Plot for Two Shutter Speeds.*

## 3.5 Resolution Effect on Depth of Field Calibration

One of the original potential velocimetry methods, PTV, requires images to be taken at higher frame rates, which results in lower resolution. Therefore, the effect of lower resolution images on the calibration procedure is studied. If there is not a significant difference in results, then calibration can be taken before PTV data is collected in the same camera orientation. This would save time and reduce the chance of inconsistencies if the calibration results are sufficient.

For this experiment, images are taken at a resolution of 512 by 384 pixels with the SA6 camera. This resolution corresponds to the specifications of SA6 camera at a frame rate of 8,000 frames per second since it is the lowest frame rate that is estimated to record at least four frames of each droplet according to Table 2. A sample image from this calibration testing is shown in Figure 38.

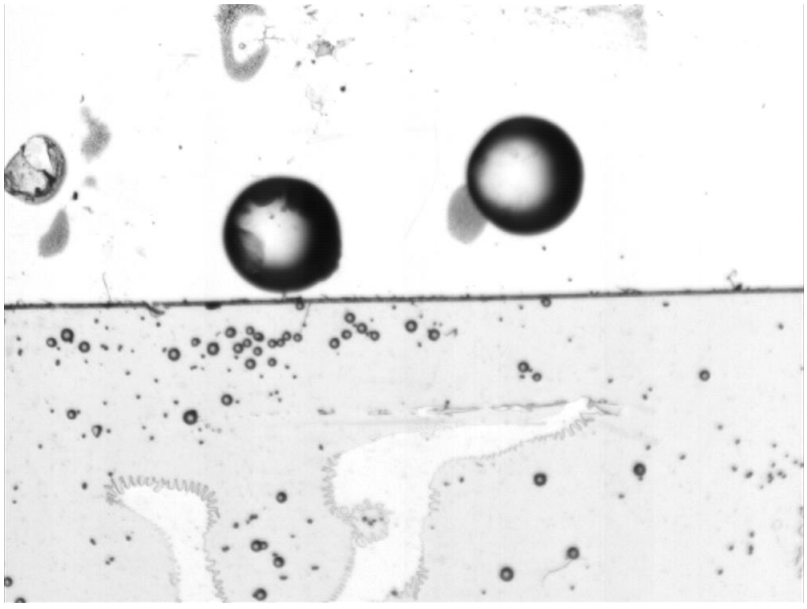

*Figure 38: Image from Calibration Testing at a Lower Resolution.*

The results of this experiment show that calibration testing can not be completed at significantly lower resolutions. Due to the lower resolution, the relative difference between particle gradients as the distance changes is not significant. As shown by the mean normalized intensity gradient plot in Figure 39, the standard deviation for this data is too large to create any meaningful thresholds. This would make approximations for focal plane depths meaningless and result in not effectively filtering out droplets that are not in-focus. Calibration data will only be taken at the maximum resolutions of the high-speed cameras when collecting droplet data. Since the PTV method for velocity data is not selected for collecting velocity data, this is not an issue. PSV data is collected at relatively low frame rates, and thus, maximum resolution.

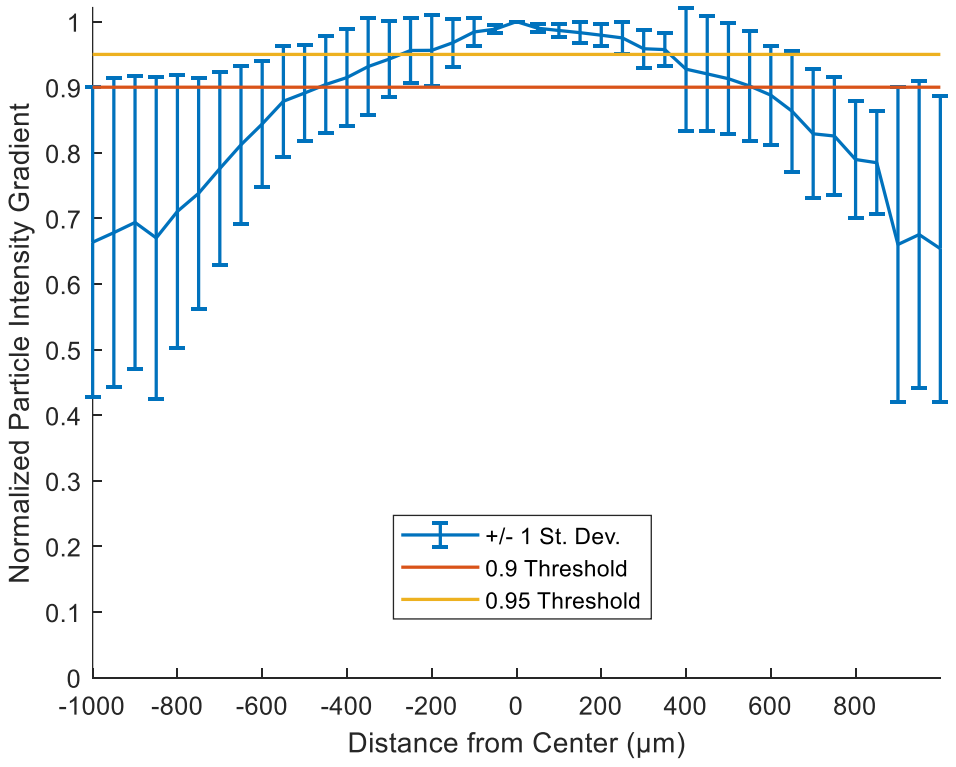


*Figure 39: Mean Normalized Intensity Gradient for Images Captured at Lower Resolution.*

# Chapter 4

# 4. Droplet Identification Program

A series of Matlab algorithms were developed to analyze two different types of raw droplet images. The first set of codes are used to measure the size of each individual droplet in each frame from images at high shutter speeds with no blur. This is used to create droplet size distributions. These distributions are also made spatially in the radial direction. The second set of codes are used to analyze the images with intentional motion blur at lower shutter speeds. These are used to provide velocity distributions, which can also be created spatially in the radial direction. Both sets of codes are created by modifying previously developed algorithms intended to measure different objects than droplets [22, 28]. A full list of codes developed for the present study are listed in Appendix A.

## 4.1 Droplet Size Distribution

A droplet identification program was developed using Matlab, inspired by a similar program designed for analyzing gas bubbles in water during bubbly flow [22]. The primary distinction between these two applications lies in the size difference between bubbles and droplets. Identifying overlapping bubbles, a concern uncommon with droplets due to their smaller sizes and fractions, was important for the original program. Conversely, droplets being out of focus, which is not a major concern for bubbles, prompted the addition of intensity gradient controls to filter out

out-of-focus droplets. The code was further enhanced to facilitate the identification of smaller ellipses and updated to account for the different camera configurations for the present study.

The droplet identification program commences by inputting a series of images from a single experimental run. Each image is then processed individually, and the image processing steps for an enlarged section of a sample frame are illustrated in Figure 40. After inputting the raw image (Figure 40(a)), a comparison with the background image generates a pre-processed image (Figure 40(b)). Subsequently, pixels with an intensity gradient exceeding the predetermined thresholds from the depth of field calibration are identified (Figure 40(c)). The image is then reversed, and small ellipses, indicative of either noise or droplets too small for accurate measurement, are filtered out (Figure 40(d)). The identified droplets are filled in and numbered from left to right (Figure 40(e)), and statistical information regarding their sizes is recorded (droplet 3 is situated outside of the enlarged section of the overall frame shown throughout Figure 40). Finally, the generated outlines are superimposed onto the original raw image (Figure 40(f)). The droplet identification program also generates overall size distribution data and graphs after all the images are processed.

Figure 41 displays the complete frame from which the enlarged section depicted in Figure 40 was extracted. Figure 41(a) shows the complete raw image, which came from one of the atomization experiments in Chapter 5. Figure 41(b) shows the same image with every identified in-focus droplet outlined. It's evident that the program effectively avoids identifying blurry droplets that are out of focus. The number of droplets filtered out depends on the programmed intensity gradient threshold determined from calibration.

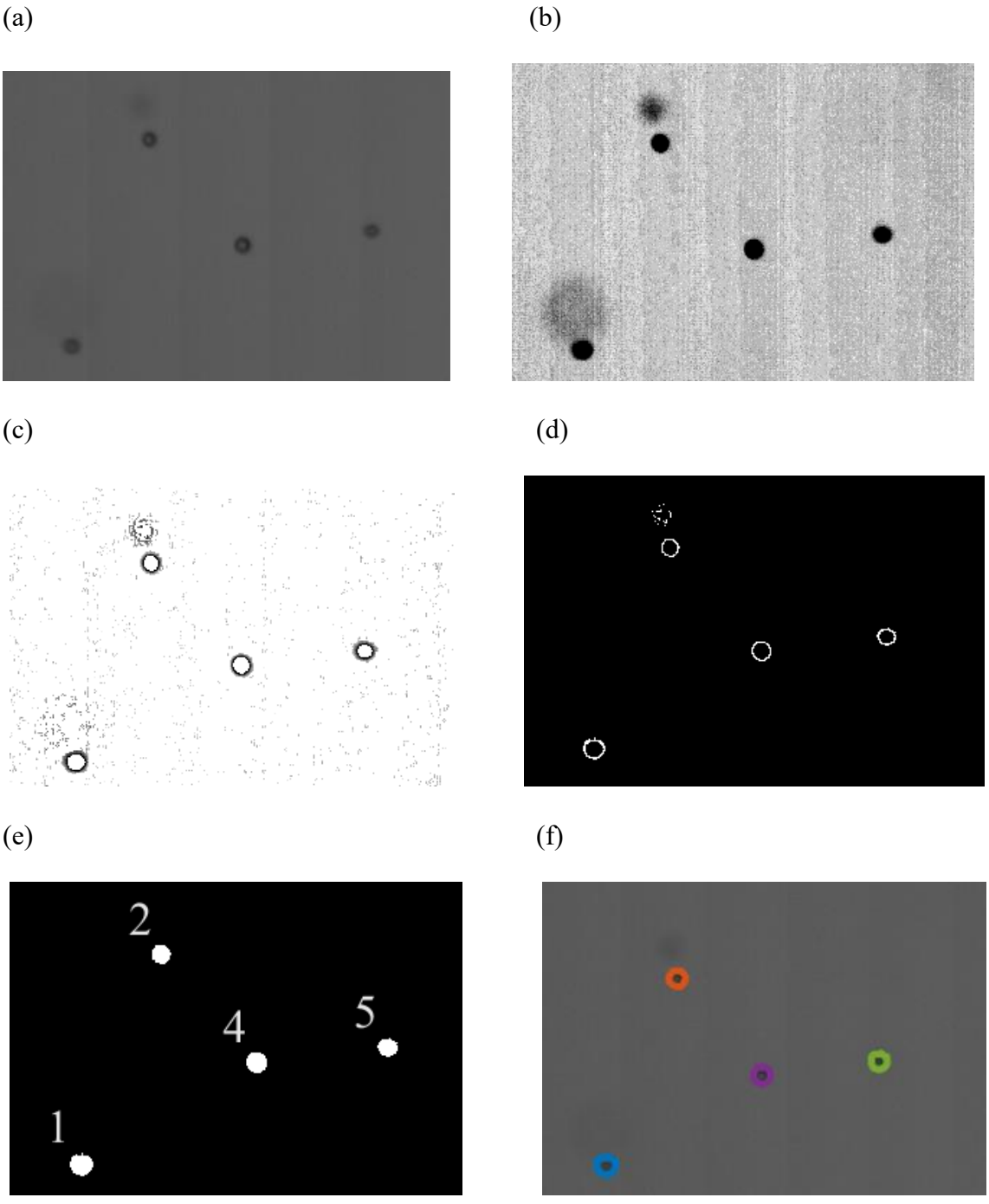


*Figure 40: Steps for an Enlarged Section of a Sample Frame in Droplet Identification Program, Including (a) the Raw Image, (b) the Pre-Processed Image, (c) the Intensity Gradient Filter, (d) the Noise Reduction Filter, (e) the Final Droplet Identification, and (f) the Identified Droplets Plotted over the Initial Raw Image.*

(a)

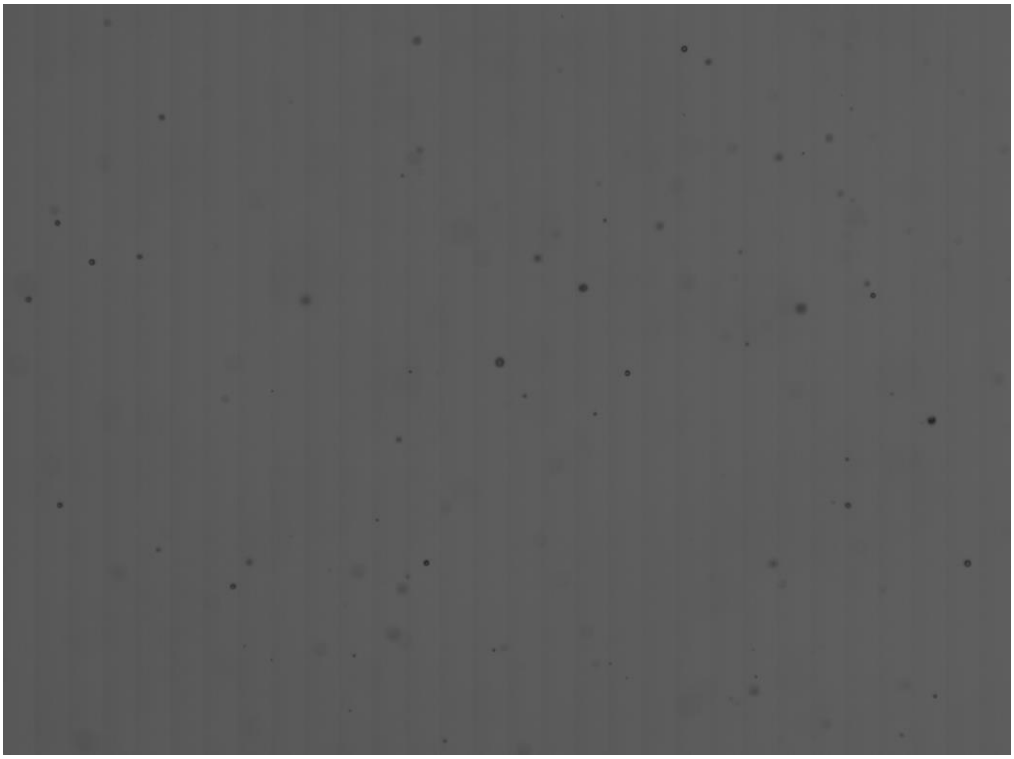

(b)

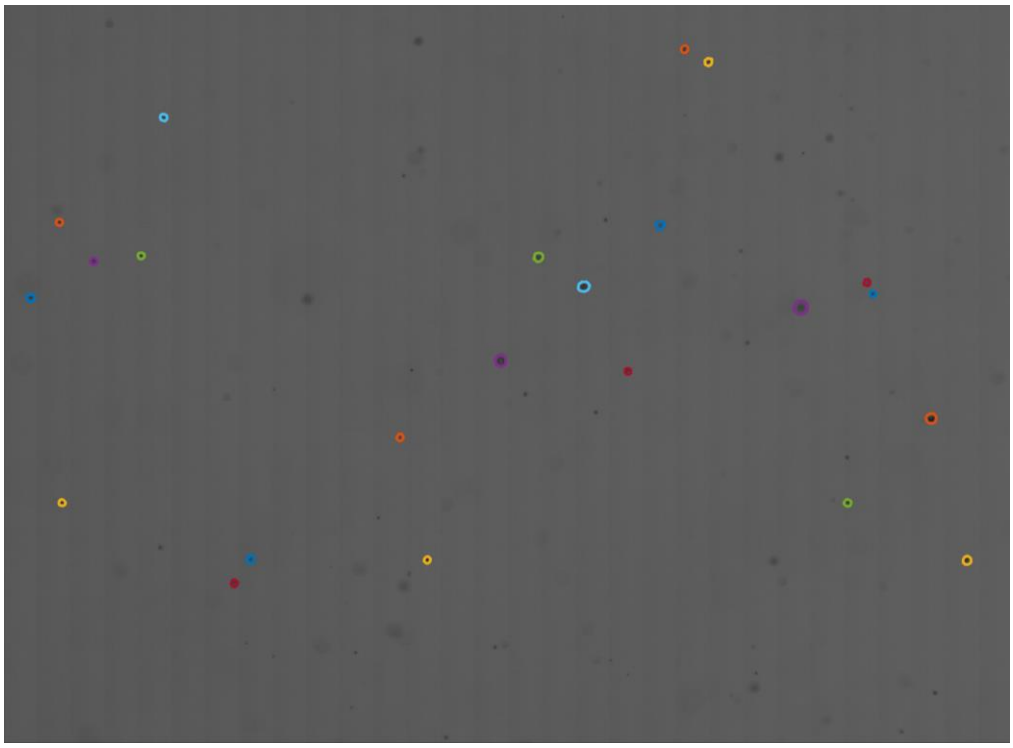

*Figure 41: Entire Sample Frame (a) Raw Image and (b) with Identified Droplets Outlined.*

## 4.2 Droplet Velocity Distribution (PSV)

A droplet PSV program was developed using Matlab, inspired by a similar program designed for analyzing small moving solid particles [28]. The literature also included similar program for PIV and PTV methods for analyzing particle velocity, but these two methods do not work well for some annular flow conditions to record droplet velocity. This is explained further in Chapter 5. For this PSV program, raw images taken at low shutter speeds to cause intentional motion blur are required. The program calculates the distance of a droplet's streak, which is how far it traveled during the exposure duration, to determine the droplet's velocity.

The PSV program allows users to set an intensity threshold as well as input a few different maximum and minimum size parameters. These settings allow the program to filter out droplets that are significantly out-of-focus and other noise. Figure 42 shows an entire sample image and an enlarged portion of this image processed through the PSV program. Figure 42(a) shows the initial raw image. As seen in the enlarged portion, there appears to be two relatively darker droplet streaks in the middle of this image along with many faint additional streaks in the image. Figure 42(b) shows the pre-processed image after the raw image is compared to the background image. While many streaks appear, the two streaks mentioned in the previous enlarged portion still appear much brighter than other streaks in the image.

Figure 42(c) shows the identified rectangular regions with droplet streaks after the image is processed through intensity and size filters. These regions contain droplet streaks that end in two of their opposite corners, which is used to calculate the distance the droplet traveled. The width of the streak is the droplet's diameter, which is subtracted from the total distance between opposite corners to find the distance travelled during the shutter speed time and thus, individual droplet velocity. Finally, Figure 42(d) shows the final identified and recorded droplet streaks within the

regions identified in 42(c), including the two previously mentioned streaks in the enlarged portion of the image. The PSV program also generates overall velocity distribution data, as well as vertical and horizontal components, and graphs after all the images are processed.

(a)

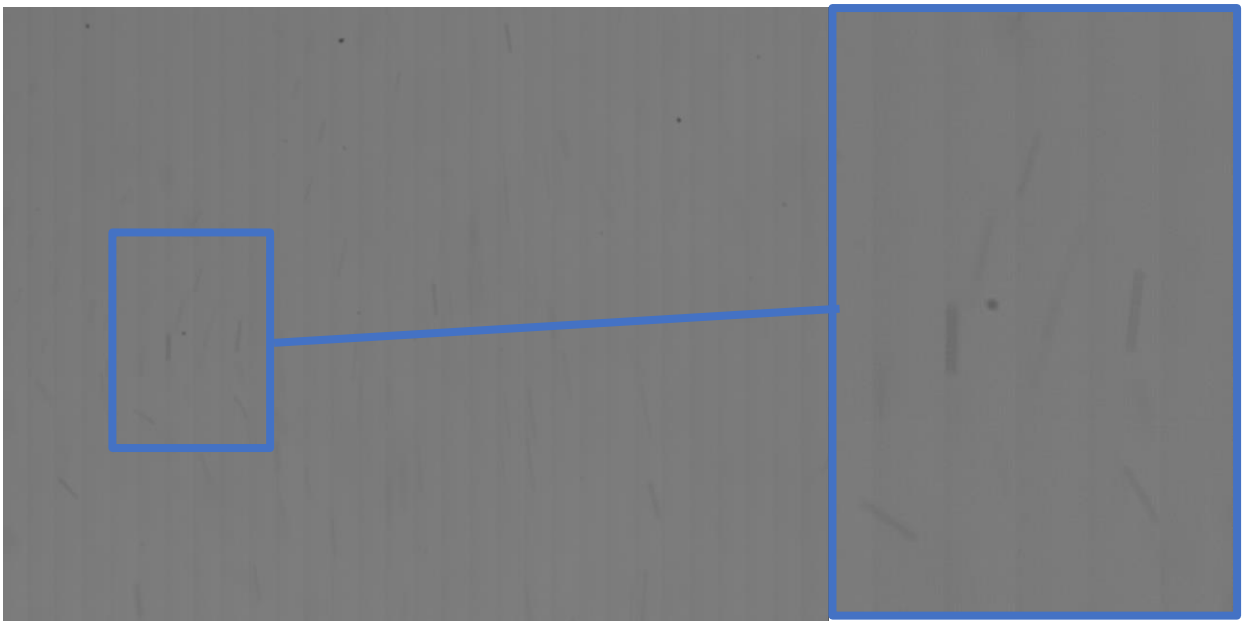

(b)

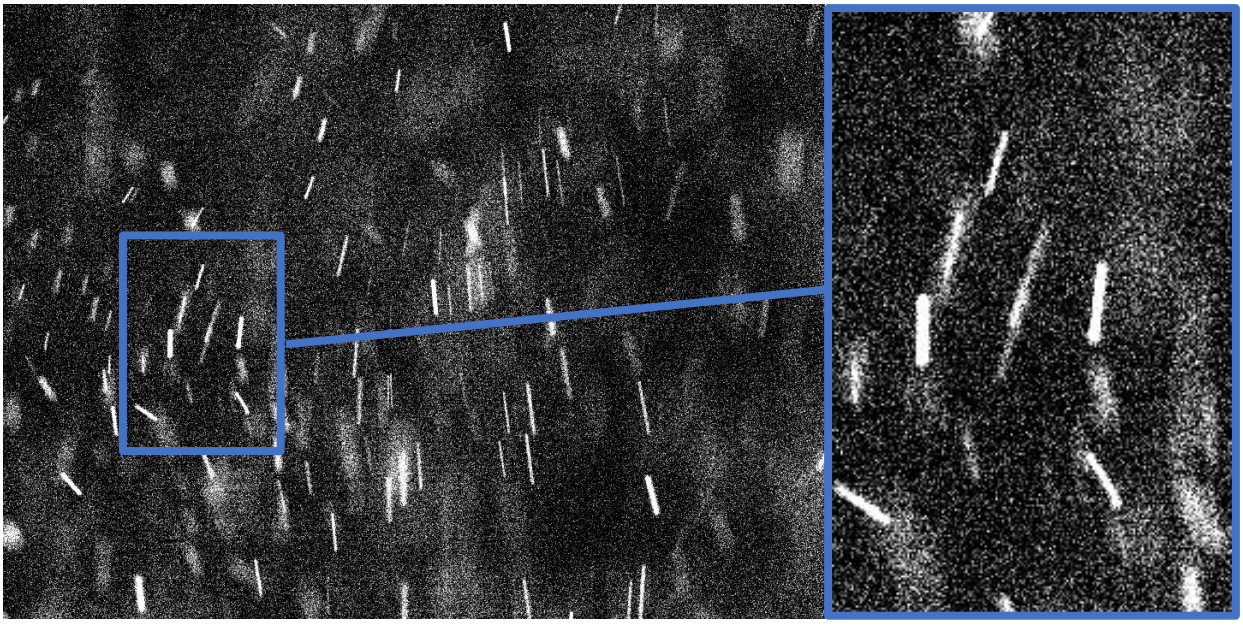

(c)

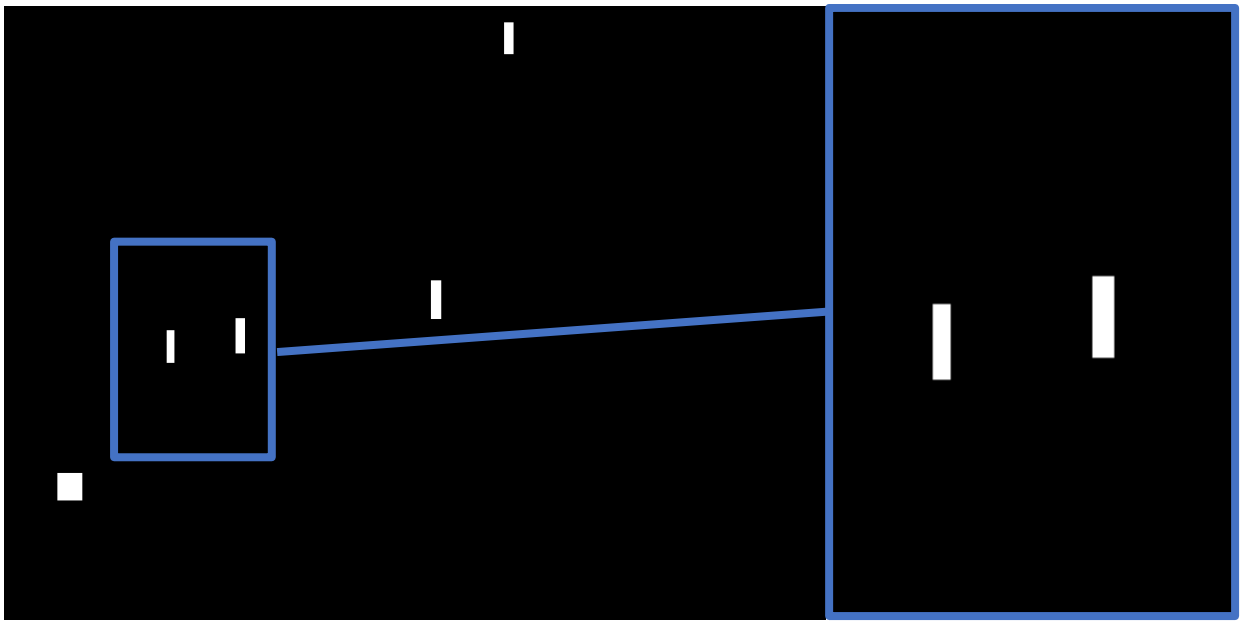

(d)

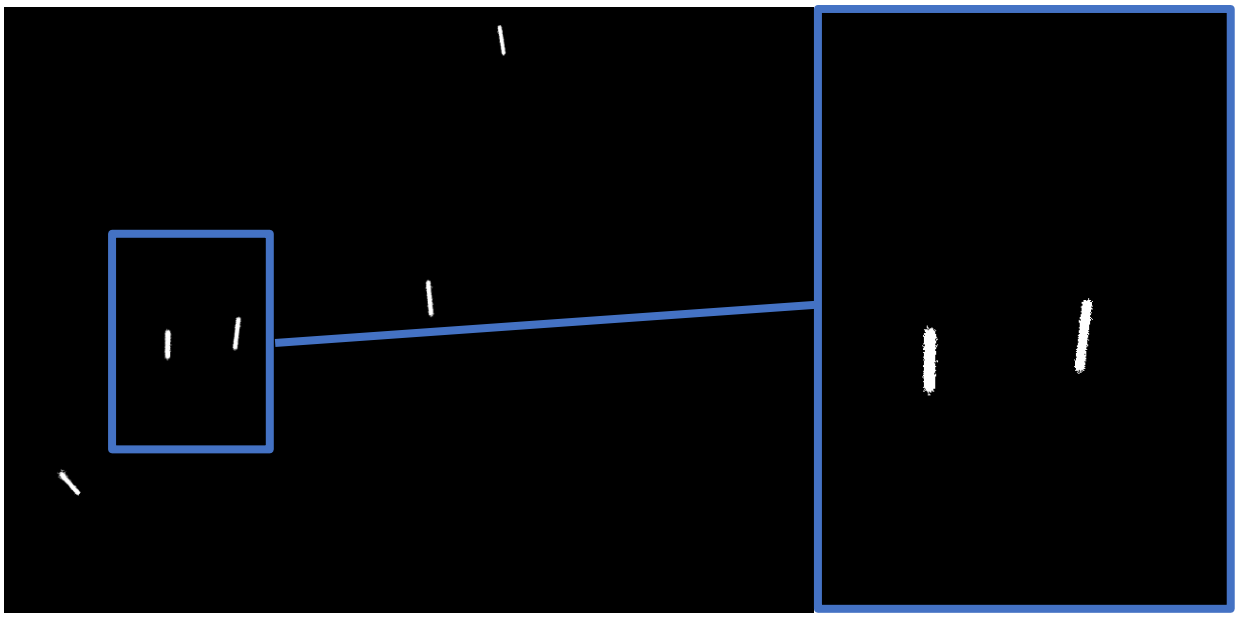

*Figure 42: Steps for a Sample Frame, with Enlarged Portion on Right, in Droplet PSV Program, Including (a) the Raw Image, (b) the Pre-Processed Image, (c) the Intensity and Size Filters, and (d) the Final Identified Droplet Streaks.*

# Chapter 5

# 5. Droplets from Atomization Experimentation

To test the droplet identification program and equipment to be used at RPI, a series of experiments are conducted at the Virginia Tech facility. Since the time available to collect data at RPI is limited and travel is required, it was important to ensure the data acquisition method works ahead of time and practice with the procedure. The applicable steps in the data acquisition process at the RPI test facility are the same in this atomization experiment or updated where appropriate. The atomization experiments help test and eliminate some issues with the original procedure plans.

## 5.1 First Atomization Experimental Setup and Procedure

In this experiment, droplets are generated by a downward-facing nozzle designed for droplet generation through atomization. The Photron SA6 camera is used with the same lens, teleconverter, and light previously discussed. Only one camera and one light are used in this experiment. An acrylic block with diffusor paper is placed between the lights and area where the droplets will flow. The diffusor paper is used to make the lighting uniform and protect the camera from direct bright light, which can potentially damage the sensor. The light's stand is aligned so the center of the light and the center of the camera are at the same height. A schematic of this setup can be seen in Figure 43. Images of the light source behind nozzle spraying droplets and high-speed camera with attached lens and teleconverter can be seen in Figure 44.

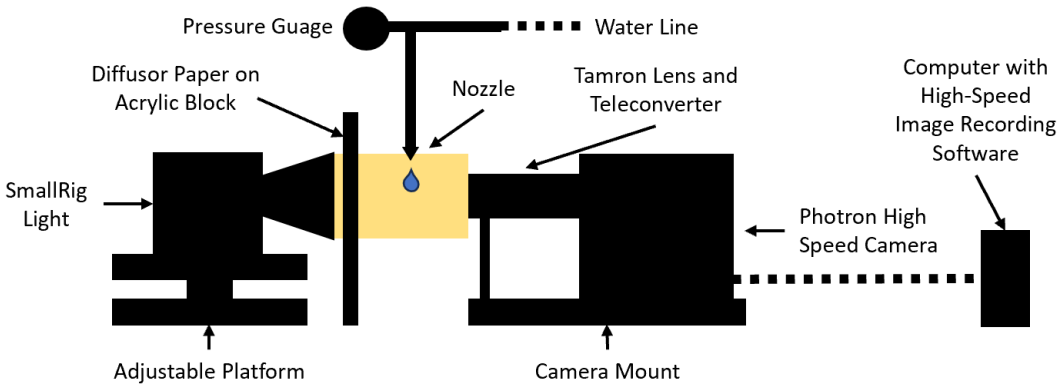


*Figure 43: Schematic of Experimental Setup at Virginia Tech Facility for Atomized Droplets.*

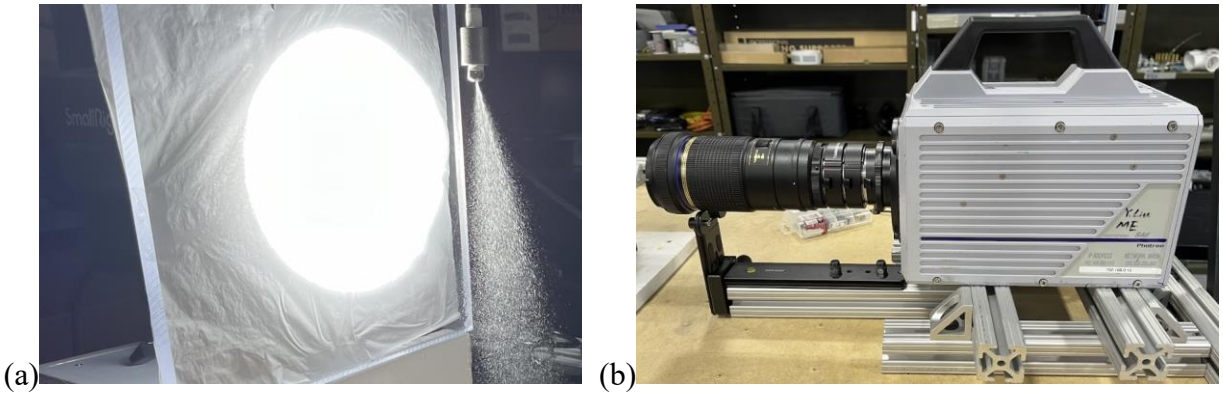


*Figure 44: Images of (a) Light Source and (b) High-Speed Camera during Atomized Droplet Data Collection.*

Once the light source and cameras are setup and turned on, the first set of calibration data is collected in the same manner as with each depth of field experiment. The final iteration of the calibration block is placed in focus with all three sizes of particles in the camera's frame. To prevent excessive brightness in the captured images, the high-intensity light was set at 50% brightness, since a relatively slow shutter speed was employed during the image capture process. The linear micrometer is beneath the calibration block to allow for precise movement. The

calibration block is then moved 50 μm at a time to cover 1 mm in each direction, for a total of 41 frames. Images are recorded at each location.

After the initial calibration is complete, the calibration block and micrometer are removed. A bucket is placed below the nozzle to collect the water after it sprays out. The nozzle is connected to a pipe that is connected to a pipe tee fitting. This fitting has a pressure gauge connected on one side and a hose connected to the lab water line on the other side. To start the droplet flow, the water supply line is turned on. Once the supply line is turned on, the pressure is recorded. For this experimental facility, the pressure is 60 psi. With droplets flowing out of the nozzle, data can be collected by using the high-speed camera software on the computer that the camera is plugged into with an ethernet cable. For this experiment, three different sets of data are collected for shutter speeds of 1/17,000 s, 1/159,000 s, and 1/277,000 s. Faster shutter speeds lead to images with less motion blur but less brightness. Different shutter speeds were tested to determine an ideal tradeoff between minimizing blur and maximizing brightness. Images were taken at 1,125 fps for all sets of data at the maximum resolution of 1,920 by 1,440 pixels. 2,000 images at the camera's maximum resolution were collected for each shutter speed. A viewing window of 11 mm was used since this is the same width that will be used at the RPI test facility.

Following the droplet data collection, a post-experiment calibration was performed after the water is turned off. This was performed identically to the calibration before the water was turned on, with the same linear micrometer and calibration target. The calibration data will be used to ensure that the testing condition did not change during the experiment. If the conditions change, the data needs to be collected again. If the conditions do not change, the calibration data can be used to determine an appropriate pixel intensity gradient threshold for the droplet identification

program to select a reasonable focal plane depth. This same procedure is used at the RPI test facility to calibrate the cameras to determine the depth of the focal plane.

## 5.2 Data from First Atomization Experiment

Prior to analyzing droplet data, the calibration data is analyzed to ensure that the testing conditions did not change during the experiment. Similar plots are generated to those created to study the different calibration target iterations. The blue regions pictured in Figure 45 are analyzed to determine how their intensity gradient changes as the distance from the camera's sensor changes. These regions account for all three sizes of particles and are randomly distributed around the target. Since the 1,600 μm particles are much larger relative to the other two particle sizes, only a portion of the particle is analyzed for their applicable test regions. Another reason for this is to avoid the imperfections around the larger particles, which cause noise in the data if they are included in the regions analyzed. The normalized particle intensity gradient for each of the 41 images taken 50 μm apart are plotted for the sets of images taken before and after the experiment in Figure 46.

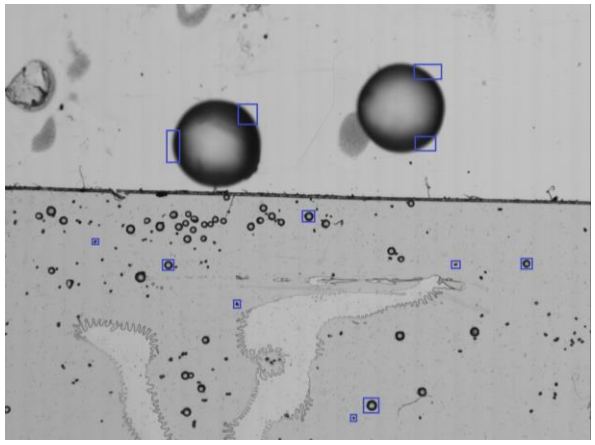

*Figure 45: Regions Analyzed on Calibration Target for First Atomization Experiment.*

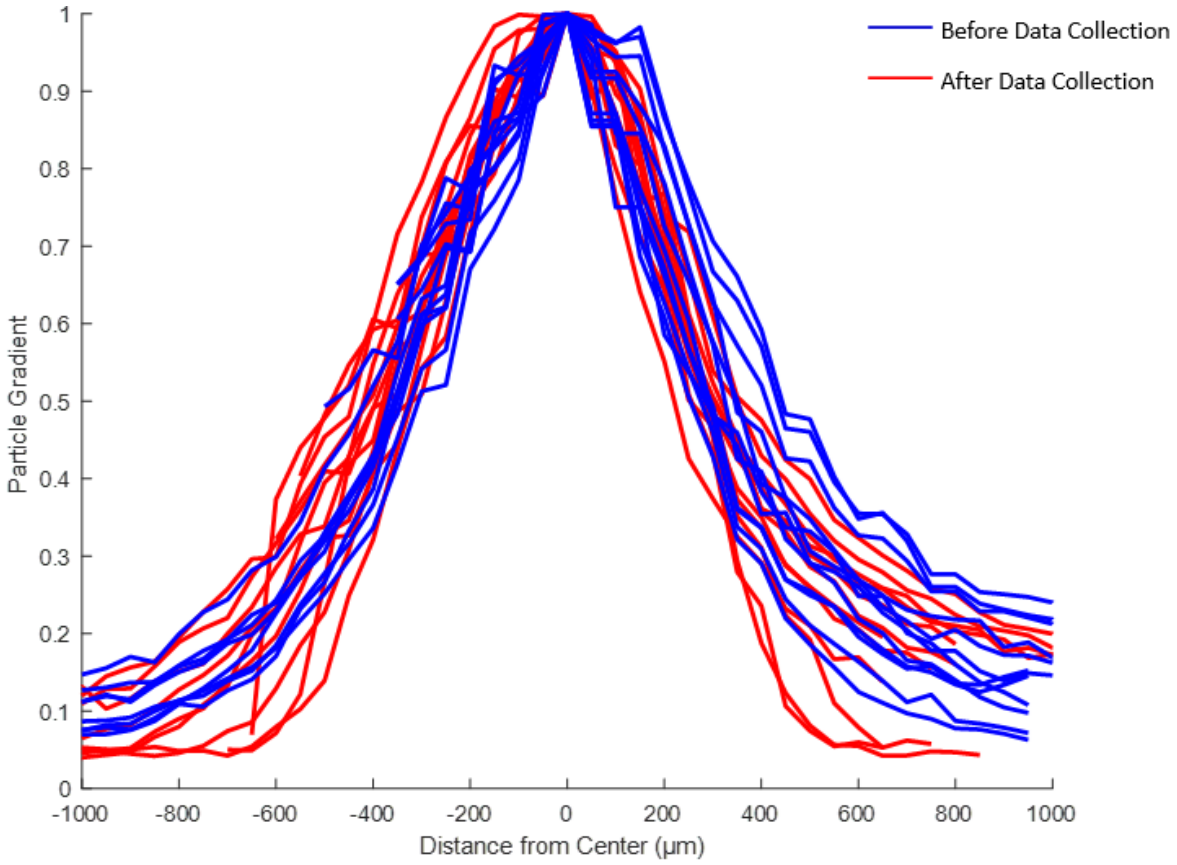


*Figure 46: Normalized Particle Gradients Before (in blue) and After (in red) Data Collection for First Atomization Experiment.*

The slopes and center of distributions of both the before and after calibration data are similar. This validates that there was not a significant change in lighting conditions during the course of this experiment. This data can also be used to determine a particle intensity gradient threshold for the droplet identification program to analyze data collected during this experiment. Figure 47 shows the mean and standard deviation of the calibration data at each recorded location. It also shows two potential thresholds that could be used in the code. The threshold in orange, 0.7 of the maximum intensity gradient, corresponds to a focal plane that is about 450 μm deep. The threshold in yellow, 0.8 of the maximum intensity gradient, corresponds to a focal

plane that is about 350 μm deep. These two potential thresholds occur where the slope is steep, meaning the estimated distance has lower sensitivity to changes in intensity gradient, as compared to where the slope is flatter. There are more random fluctuations in the data than previous calibration data, and this is probably attributed to reduced light intensity. In future iterations, the light brightness will be at 100% and the shutter speed will be increased to prevent the images from becoming too bright. This will likely keep the light intensity more consistent.

The data from fastest shutter speed tested in this experiment, 1/277,000 s, is analyzed first. A total of 2,000 frames were recorded, and each frame was analyzed in the droplet identification program. The program results in final processed images of each raw frame with an outline of identified droplets, as well as plots showing overall data from all frames. Figure 48(a) shows a sample processed image with identified droplets. Figure 48(b) shows an enlarged portion of the same image and the original portion of its respective raw image. These images show that the program does a good job of identifying the sizes of in-focus droplets in the size range that exist in these frames. The droplet identification program filters out smaller droplets, below a minimum projection area as specified by the user, which is why some of the smaller droplets are not identified. Droplets that are small have too high of an uncertainty with their diameter and area measurements due to camera resolution limitations. This is why the small droplet on the top right of Figure 48(b) is not identified, despite appearing in focus.

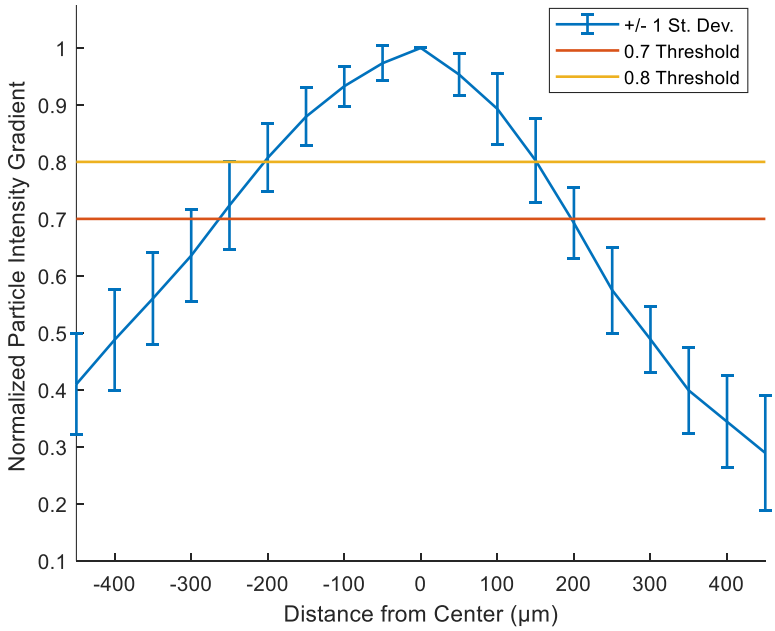


*Figure 47: Mean Normalized Particle Intensity Gradient with Two Potential Thresholds.*

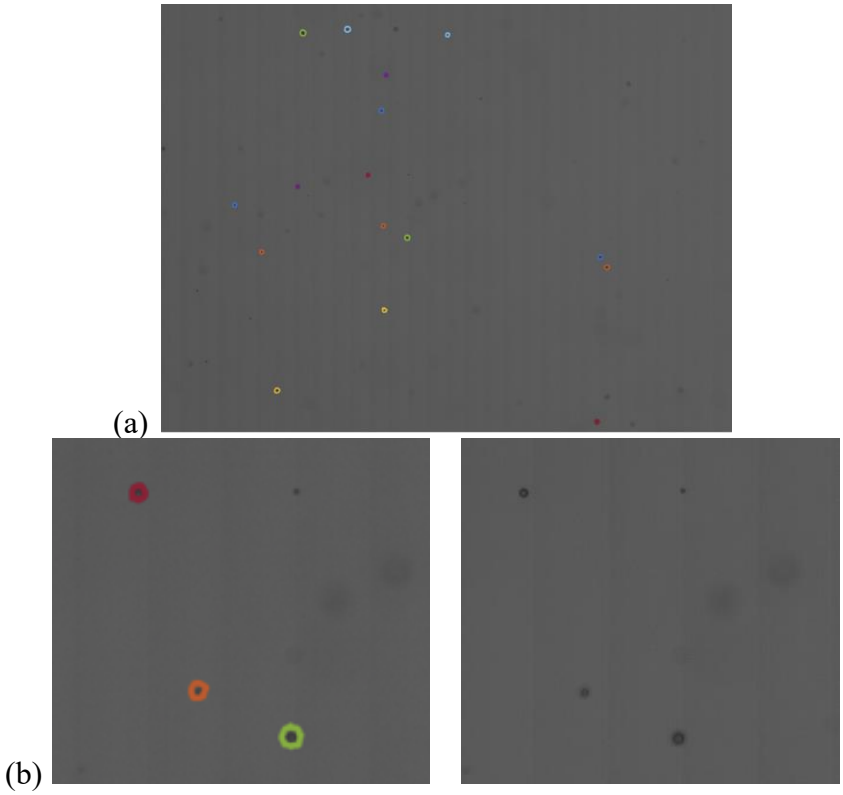


*Figure 48: (a) Sample Full Frame and (b) Enlarged Portion of Frame Compared to Raw Image from 1/277,000 s Shutter Speed Experiment.*

A variety of figures are created once each frame of droplet data is processed through the droplet identification program, such as Figure 49, which displays a histogram of the droplet size distribution for this experiment. The majority of droplets are between 0.1 and 0.2 mm, which makes sense because a commercial atomization nozzle is used in the experiment. It would be expected that a commercial atomizer would have a relatively narrow range of droplets produced.

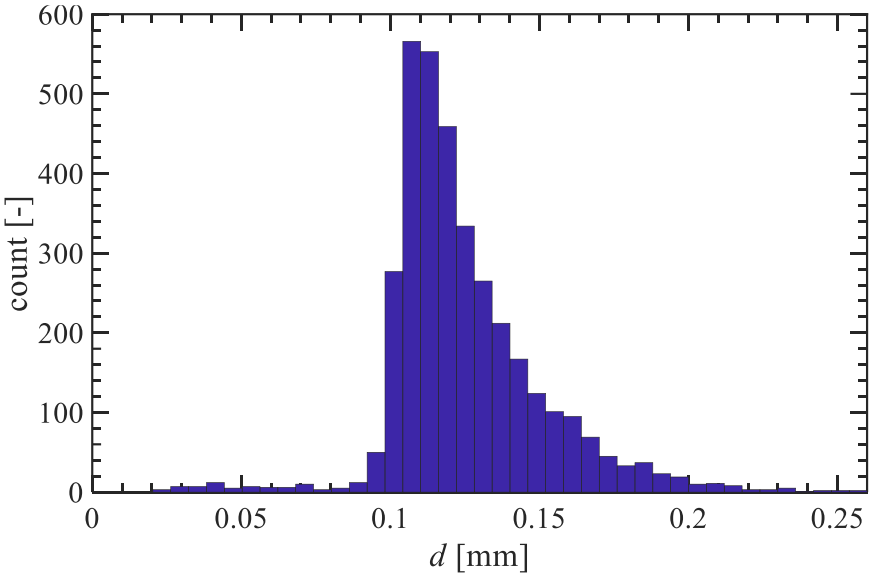


*Figure 49: Droplet Size Distribution from First Atomization Experimental Data taken at 1/277,000 s Shutter Speed.*

Other figures that the droplet programs can display include some which display spatial distributions of different droplet parameters. For instance, Figures 50 and 51 present distributions of droplet number density and droplet fraction, $\alpha_{d,}$ in the horizontal direction across the 11 mm wide frame. While these figures display significant fluctuations, they appear to be random across the image frame suggesting a uniform nozzle spray pattern. The fluctuations are likely due to only using 2,000 frames for this specific experiment and the relatively low droplet fraction.

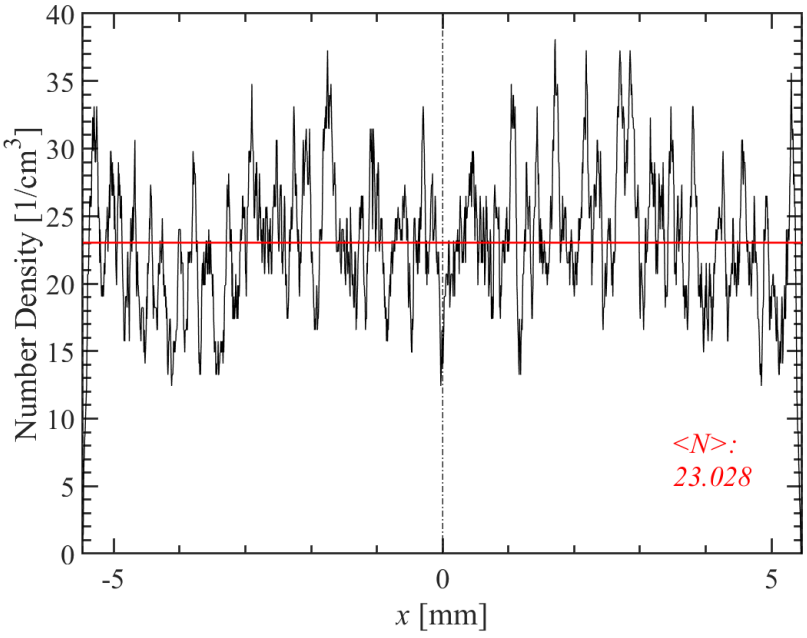


*Figure 50: Distribution of Droplet Number Density in the Horizontal Direction, with Area-Average in Red.*

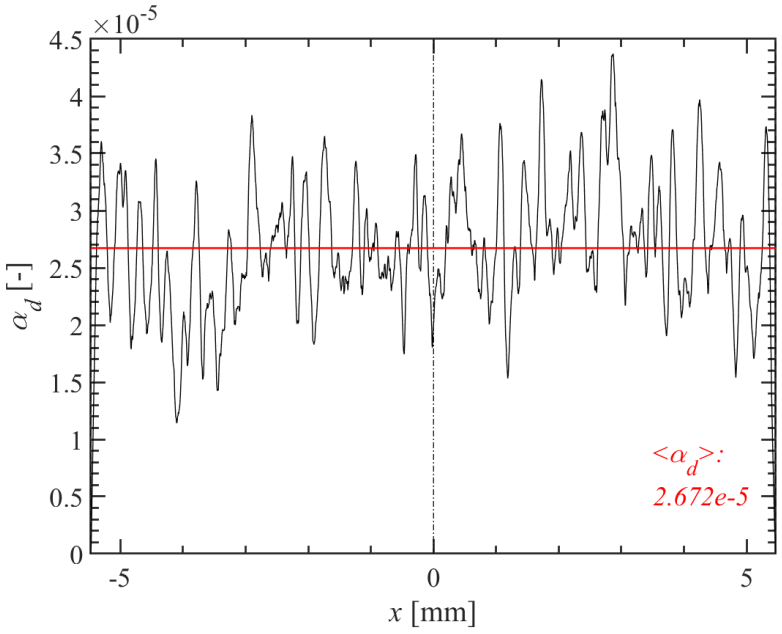


*Figure 51: Distribution of Droplet Fraction in the Horizontal Direction, with Area-Average in Red.*

The data and figures from the 1/277,000 s shutter speed experiment can be compared to data collected by the other shutter speeds to assess if they are still accurate. The slower shutter speeds are more likely to have more significant occurrences of motion blur. However, if the data is similar, the slower shutter speed images will have less background noise due to more light reaching the camera sensor. Figure 52 shows a histogram comparing the droplet size distribution of the data from the 1/277,000 s shutter speed experiment and the 1/159,000 s shutter speed experiment. 2,000 images were taken and processed for both shutter speeds. Also, the testing configuration and conditions were identical for both datasets, besides the shutter speeds used. Therefore, the actual sizes of the droplets can be assumed to have the same size distributions for both datasets. A few key parts of Figure 52 provide evidence that the 1/159,000 s shutter speed data is significantly different and likely less accurate. First, many more droplets were identified by the 1/159,000 s data set by the droplet identification program, since each bin of the 1/159,000 s histogram contain a higher count. Second, the 1/159,000 s distribution includes droplets of larger sizes that did not exist in the 1/277,000 s distribution. Third, the median droplet diameter of the 1/159,000 s distribution is 0.144 mm compared to 0.130 mm for the 1/277,000 s distribution, an 11% increase.

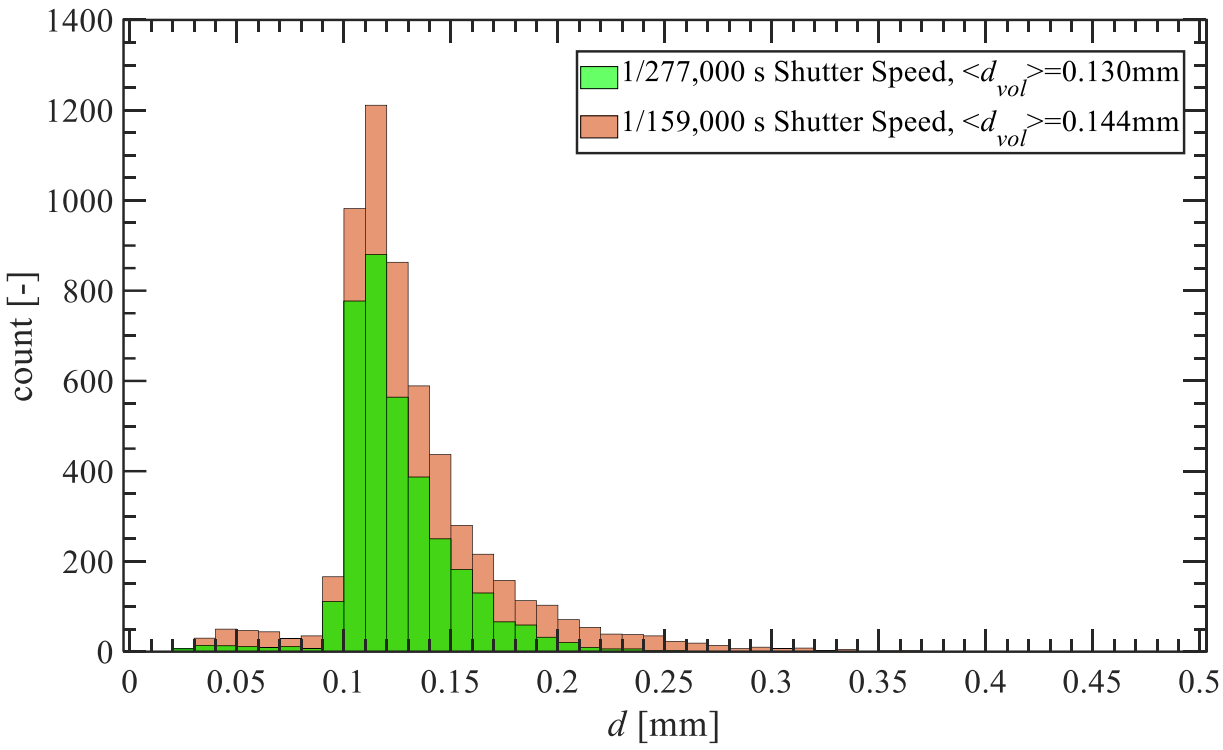


*Figure 52: Droplet Size Distribution Histogram for 1/277,000 s and 1/159,000 s Shutter Speeds.*

There are a few reasons for these differences in the size distribution. First, some of the droplets recorded at this slower shutter speed exhibit motion blur that was insignificant for the faster shutter speed. As seen in Figure 53(a), one of the droplets in a sample image taken with the slower shutter speed that appears to be within the focal plane experiences motion blur. The motion blur is not seen in the faster shutter speed image in Figure 53(b). Motion blur causes the droplets to appear to the droplet identification program as larger than they actually are, hence, the median diameter is larger and larger droplets were identified for the slower shutter speed.

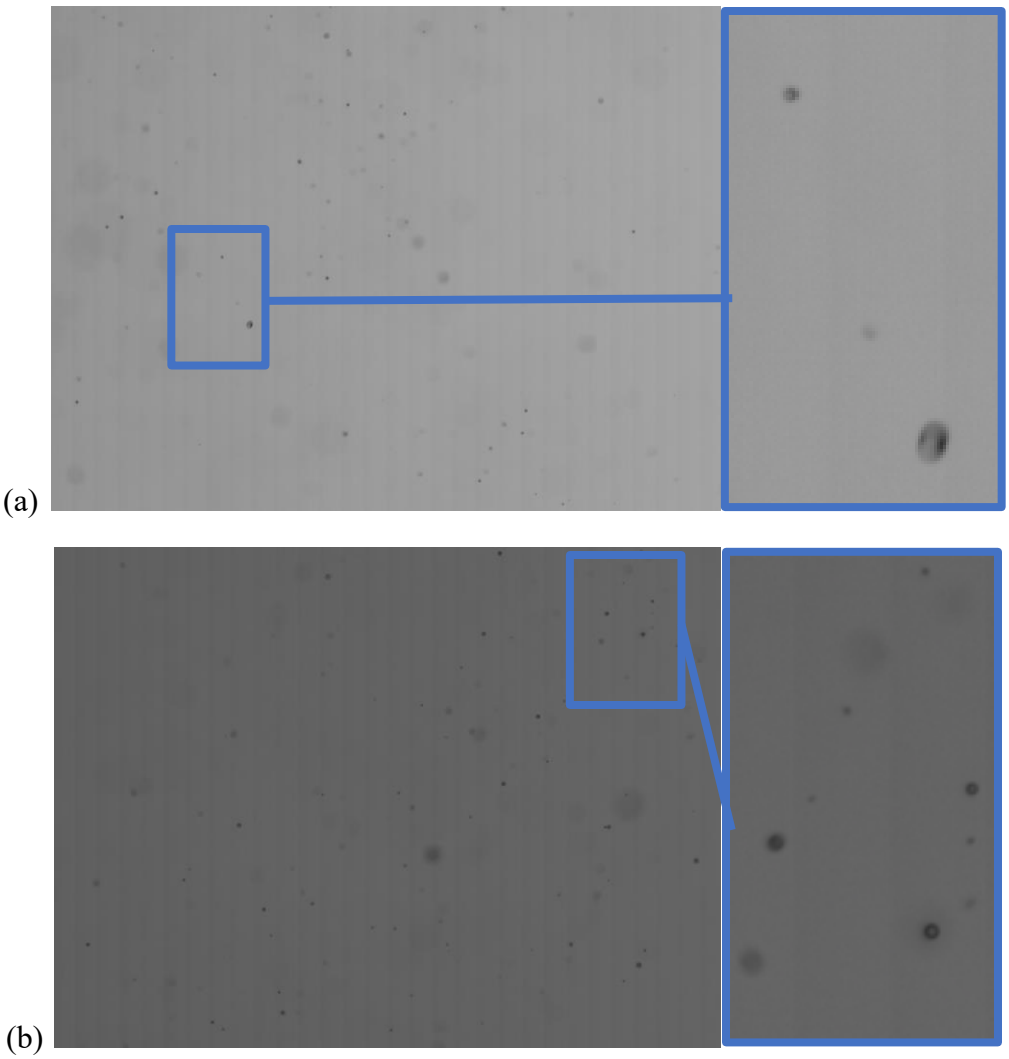


*Figure 53: Sample Frames with Enlarged Sections taken at (a) 1/159,000 s and (b) 1/277,000 s Shutter Speeds.*

Second, since motion blur exists for some of the in-focus droplets, the droplets do not appear as dark relative to the out-of-focus droplets. Therefore, more droplets that should be filtered out as out-of-focus are included in the size distributions created by the droplet identification program. This explains why the distribution in Figure 52 includes significantly more droplets for the slower shutter speed in each bin on the histogram. Even with the intensity gradient filter, many out-of-focus droplets have similar intensity gradients as the in-focus droplets that are blurred. Two

examples from enlarged portions of sample frames taken with the slower shutter speed of 1/159,000 s can be seen in Figure 54. The raw image is compared to the final droplets identified by the identification program. In both sample frames, it is clear that out-of-focus droplets are inaccurately identified. Furthermore, it is evident that the program records the outlines of the in-focus droplets, particularly the one outlined in blue in Figure 54(a), as larger than their true sizes due to motion blur in the images. Shutter speeds of 1/159,000 s and below will no longer be used for collecting droplet size data.

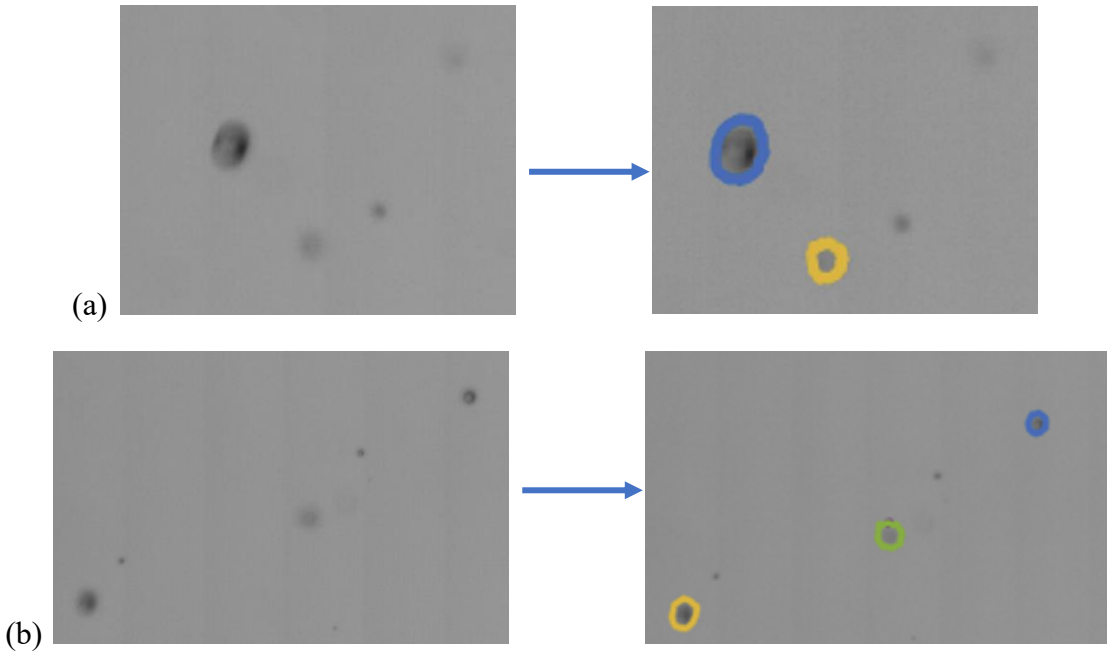


*Figure 54: Enlarged Portions of Sample Frames Taken at 1/159,000 s Before and After Processing by the Droplet Identification Program.*

## 5.3 Developing Flow Experiment

A second experiment with the atomization nozzle is conducted similar to the first, but with a new objective. The first experiment showed that for the 1/277,000 s shutter speed, the droplet identification program identifies small droplets well, especially those between 0.1 and 0.2 mm in diameter. Collecting data of larger droplets would allow for further assessment of the program's capabilities. Therefore, data is collected with the nozzle lowered to allow the camera to record close to the nozzle outlet. This will allow the camera to record larger droplets since droplets are larger closer to the nozzle's outlet before they separate into smaller droplets and before the flow is fully developed. The same equipment from the previous atomization equipment is used. A total of 2,000 images are collected at the highest three shutter speeds options for the highest resolution, which are 1/186,000 s, 1/277,000 s, and 1/367,000 s. One of the images taken in this configuration with a shutter speed of 1/277,000 s is displayed in Figure 55.

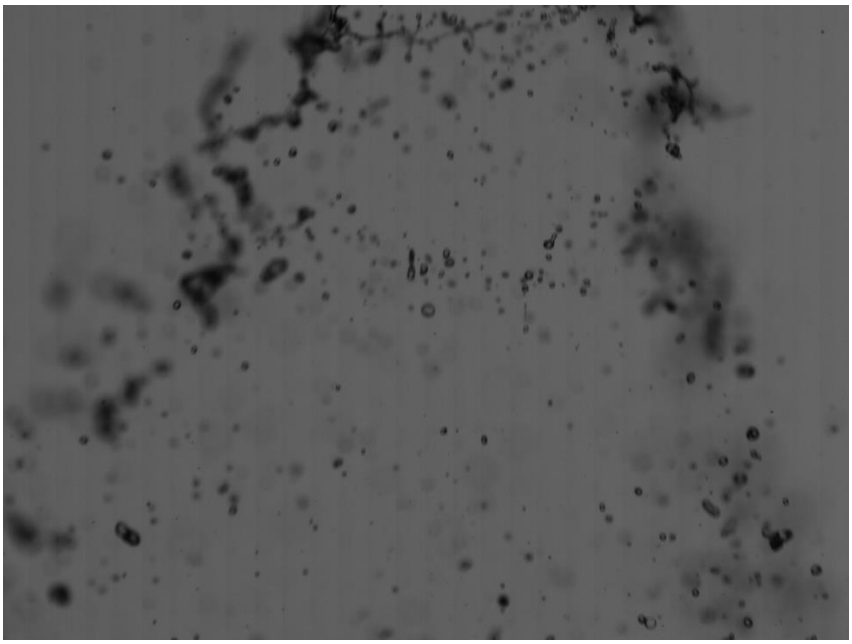

*Figure 55: Sample Image of Developing Flow Near Nozzle Outlet.*

After processing these images through the droplet identification program, it is clear that developing flow can not be accurately processed by this program. The program is unable to successfully filter out developing droplets that are not elliptical. Instead, the program tries to identify the large ligaments as potential elliptical or circular droplets with a diameter, which will skew any statistical results. The sample frame from Figure 55 is processed in Figure 56, which includes an enlarged section of one of the ligaments that the algorithm has trouble processing, despite passing through all of the normal programmed filters. The ligament should be filtered out since the program is intended to record elliptical droplets. It is concluded that the input images to the droplet identification program must consist of fully developed droplets.

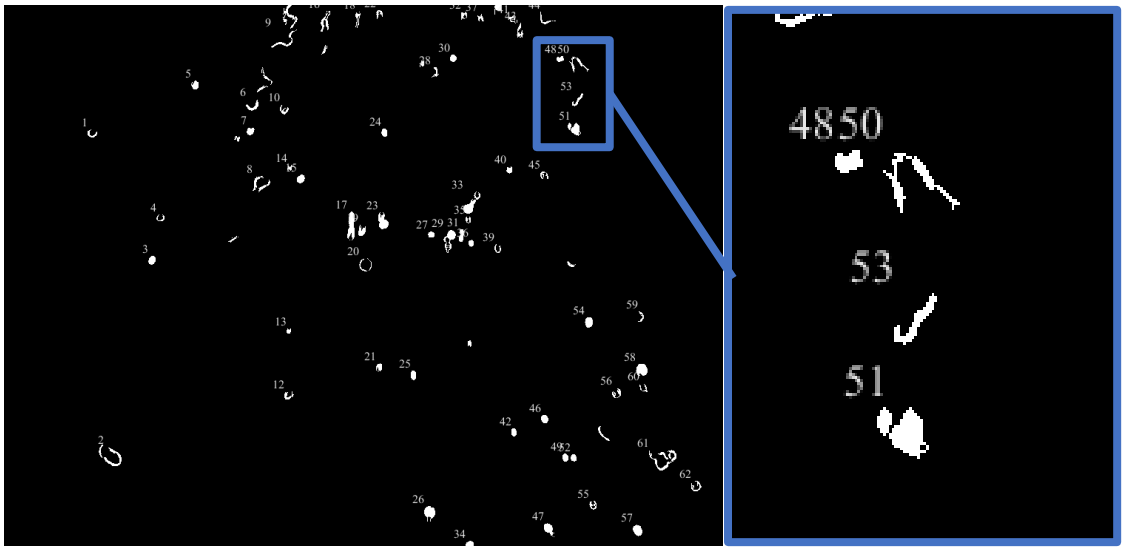


*Figure 56: Developing Flow Processed through Droplet Identification Program.*

## 5.4 PTV and PIV Image Capturing Experiment

Another atomization nozzle experiment is conducted to collect data that can be used to analyze the velocity distribution of droplets, with a similar experimental setup as the previous experiments. For this type of data, individual droplets are tracked between multiple images. The change in distance between successive images divided by the shutter speed determines the particles velocity for the PTV method. The images are also used to test the PIV method.

To collect velocity images, the SA6 camera's frame rate is increased from 1,125 fps to 8,000 fps. At 8,000 fps the resolution is decreased to 512 by 384 pixels and 30,000 images are collected for shutter speeds of 1/202,000 s and 1/277,000 s. This frame rate was chosen since it is the lowest frame rate that is predicted to collect over four frames per droplet, as shown previously in Table 2. If a higher frame rate is chosen, the resolution will decrease even further. The intensity of the light source is decreased to account for the change in frame rate since there is significantly more time for light to enter the camera.

The reduced resolution images allow for the collection of more images at once compared to high-resolution images, due to the reduced memory requirements. The camera is moved further from the nozzle and the magnification is decreased on the Tamron lens to account for the change in resolution. The nozzle is also raised three inches for this velocity test, so the data collected is more developed than right below the nozzle outlet. It is hard to track droplets that are still separating into smaller droplets. The physical size of the frame remains 11 mm.

An example of three successive frame taken with a shutter speed of 1/277,000 s is shown in Figure 57. It is easy to notice some droplets travelling downwards between frame, such as the one emphasized with a black box around it in each frame. The number of pixels that the droplet

travels between each frame can be divided by the shutter speed to determine the velocity of each droplet for the PTV method of analyzing velocity. The PIV method is also tested with this data.

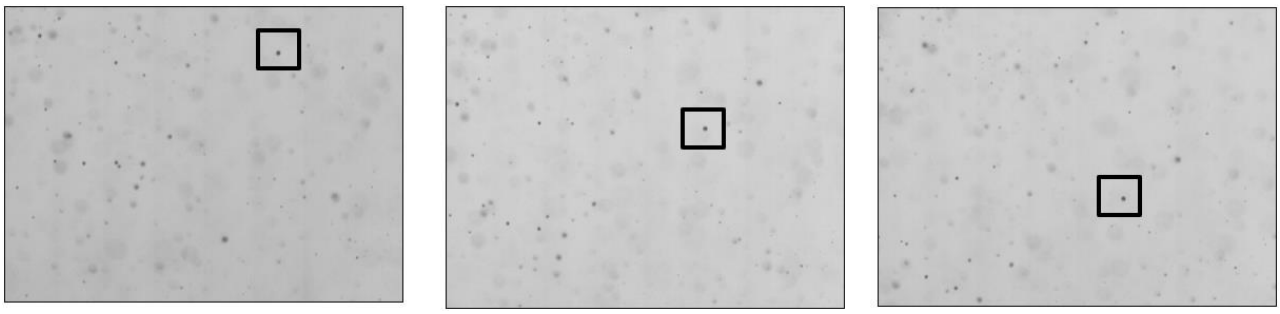

*Figure 57: Three Successive Frames Captured at 8,000 fps with the Same Droplet Marked.*

After the data is saved, it is uploaded to Matlab PIV and PTV programs similar to ones used in the literature [28]. The PIV program enables users to specify the number of subregions into which to divide the overall frame. The program then finds the instantaneous velocity of each subregion by tracking clusters of particles and provides a plot with velocity vector maps in each subregion. PIV algorithms perform well with dense particles since all particles in the frame are analyzed together. Unfortunately, the images processed in the present study resulted in too much noise to produce useful results. The velocity vectors experienced significant and constant fluctuations between frames. This is likely due to the relatively low droplet fraction.

On the other hand, PSV programs perform well with sparse particles, so it is easier to track individual particles across multiple frames. Even though the average droplet appears on a few successive frames, the PTV algorithm has trouble tracking the same droplet between frames due to their relatively fast speeds. Since the physical height of each image is only about 8 mm, many droplets travel through a significant portion of the height between frames. Since the droplets are fairly sparse, the PSV method is tested next. Sparse particles are also a requirement for PSV.

## 5.5 PSV Image Capturing Experiment

Since the PIV and PTV methods for analyzing droplet velocity do not work well for the images produced in the present study, a PSV method is tested. This method requires a different camera configuration than in the experiment to collect images for PIV and PTV analysis. Instead of tracking particles between frames, this method involves creating intentional motion blur in each frame. Therefore, a slower frame rate is used, and a higher resolution no longer needs to be sacrificed. Images for this experiment are taken at the maximum resolution with the lens settings used in the experiments for size data. The camera is also moved back to its original location, closer to the nozzle. A benefit for using the PSV method instead of the PIV or PTV methods is that the cameras and lenses can remain in the same configuration to collect both size and velocity data, which makes the data collection process easier and more consistent. This is especially helpful at the RPI test facility, where the cameras are placed on platforms 4 m above the ground.

For this experiment, images are collected at frame rates of 1/500 s, 1/1,000 s, and 1/2,000 s at the maximum resolution of 1920 by 1440 on the SA6 camera. The intensity of the light source is decreased again to account for the change in frame rate, which is slower than any of the previous experiments. Images are taken at a few different low light intensities. A total of 1,000 images are taken with each configuration. Sample images at each shutter speed with the SmallRig lights turned to low intensity settings are displayed in Figure 58. The slower the shutter speed, the longer the streak of a droplet since there is more time for the droplet to travel.

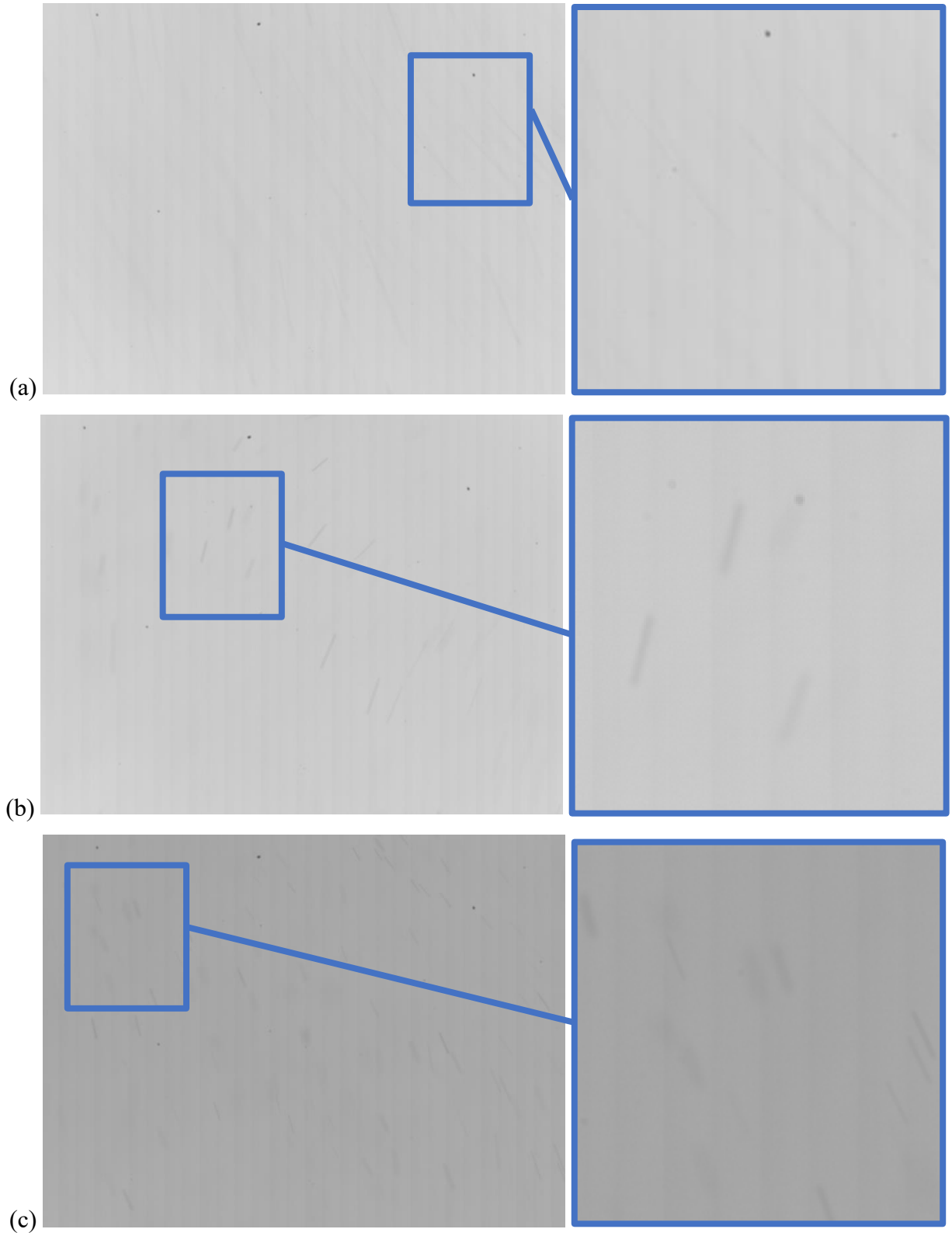


*Figure 58: Sample Droplet Frames Captured at Slow Shutter Speeds of (a) 1/500 s, (b) 1/1,000 s, and (c) 1/2,000 s.*

A few key observations can be made from these images in Figure 58. The streaks at the slowest shutter speed are very faint and hard to see, even in the enlarged portion of the image. While the focal plane affects how dark the streaks appear, exposure time is another key factor. Shorter streaks appear darker, which can be observed when comparing the long faint streaks in Figure 58(a) to the darker, but shorter streaks in Figures 58(b) and (c). Another downside of longer streaks is the higher percentage of droplet streaks that overlap. Overlapping streaks are difficult to process. On the other hand, shorter streaks have a disadvantage despite being easier to distinguish between other streaks and the background. Shorter streaks lead to more uncertainty in measurements of the distance travelled. Each streak distance consists of two parts: the change of position and droplet diameter. The droplet diameter is measured by the width of the streak. To find the droplet displacement, the droplet diameter is subtracted from the overall streak length. The higher the streak length to diameter (or width) ratio, the lower the uncertainty in displacement measurement, and thus, the lower the uncertainty in velocity measurement. In short, longer exposure times result in lengthier streaks that may blend more with the background or other streaks, making them harder to discern; however, they also reduce uncertainty for streaks that can be distinguished, compared to shorter exposure times.

Raw images from all three shutter speeds are processed in the PSV program described in the second section of Chapter 4. For the slowest shutter speed, 1/500 s, the PSV program did not produce meaningful results because the program was not able to distinguish the streaks from the background since they are too faint. Similarly, the program is not able to distinguish many streaks in the images taken at a shutter speed of 1/1,000 s from droplets produced by the atomization nozzle. Many frames had no identified streaks. Some frames with identified streaks had trouble identifying some of the streaks and contained a lot of noise in the final processed images. For

example, Figure 59 shows a sample raw image captured at a shutter speed of 1/1,000 s. Two of the droplet streaks in the image are enlarged so they can be seen easier. When this image is processed in the droplet PSV program, Figure 60 is the result. Two boxes are added to Figure 60 to show the results of the two droplet streaks enlarged in Figure 59. Although there is a little noise on the bottom left, the program does a good job isolating the top droplet streak. On the other hand, the program struggles to isolate the bottom droplet streak. This occurs on many of the frames analyzed at this shutter speed.

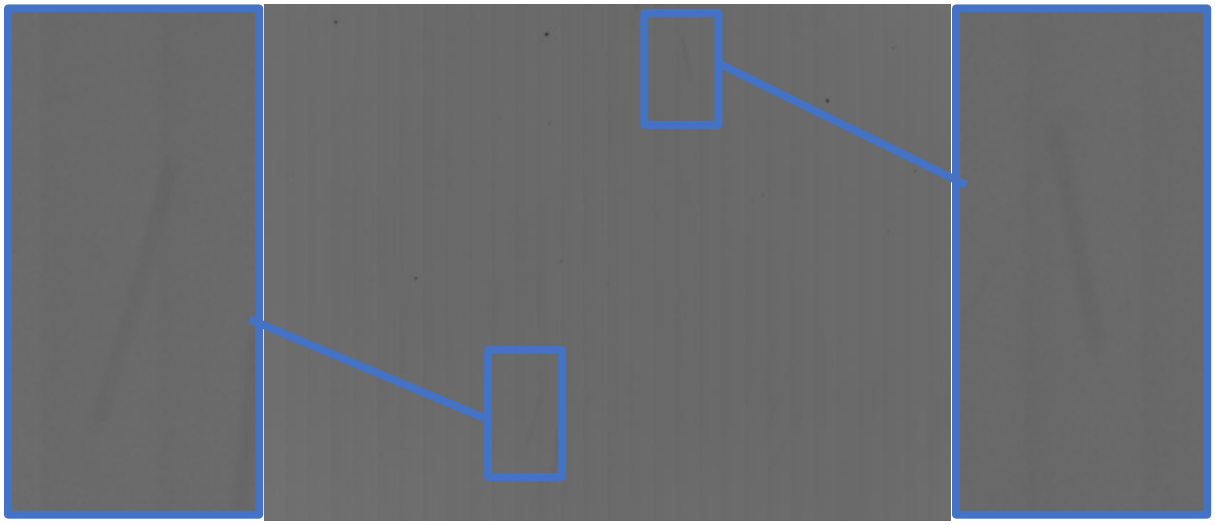

*Figure 59: Raw Sample Image with Two Enlarged Droplet Streaks from Atomization Test with a Shutter Speed of 1/1,000 s.*

Finally, the raw images taken at a shutter speed of 1/2,000 s are analyzed in the droplet PSV program. A sample image from this shutter speed is shown in Figure 61. Droplet streaks on the right side of the image can be seen much easier, even without enlargement, compared to the streaks in Figure 59. The droplet streaks are shorter, but darker and do not blend into the

background. The images processed at this shutter speed result in more identified droplets with minimum background noise. The processed result of Figure 61 in the droplet PSV program is shown in Figure 62. The final streaks are precise, leading to data that can be used for statistical analysis.

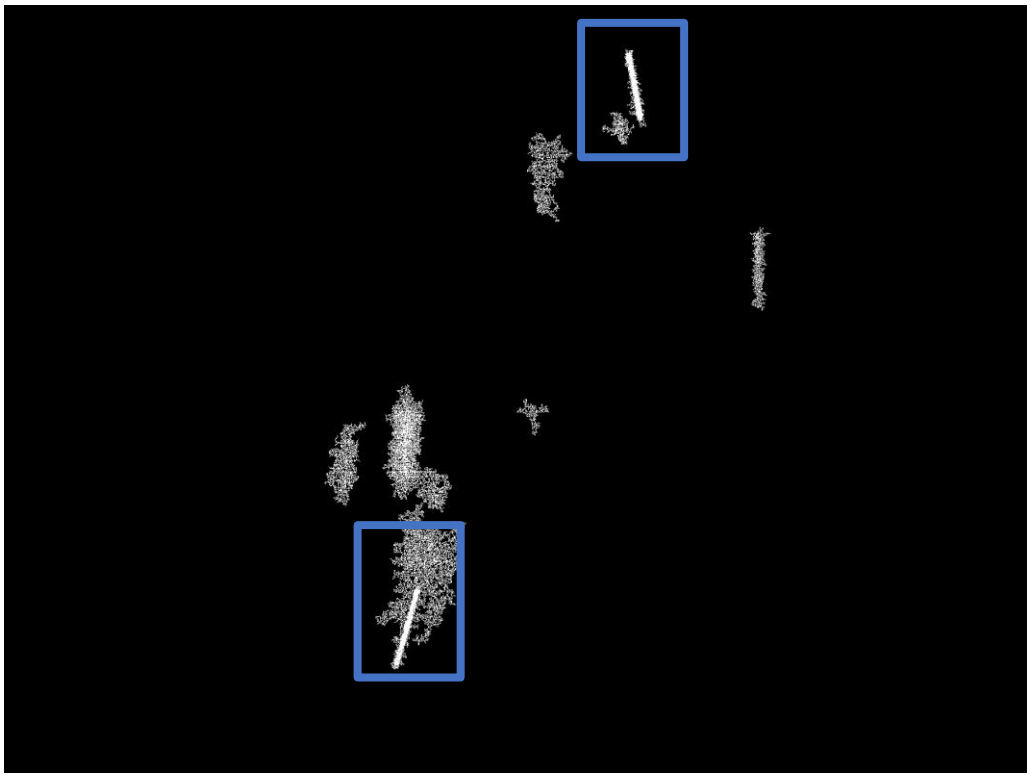

*Figure 60: Processed Sample Image from Atomization Test with a Shutter Speed of 1/1,000 s.*

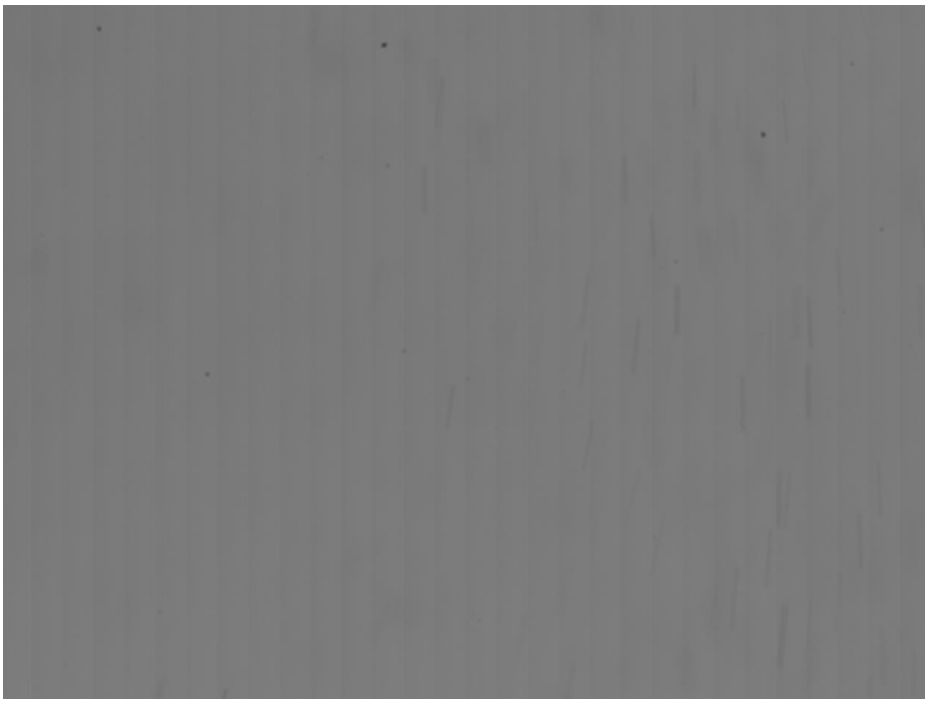

*Figure 61: Raw Sample Image from Atomization Test with a Shutter Speed of 1/2,000 s.*

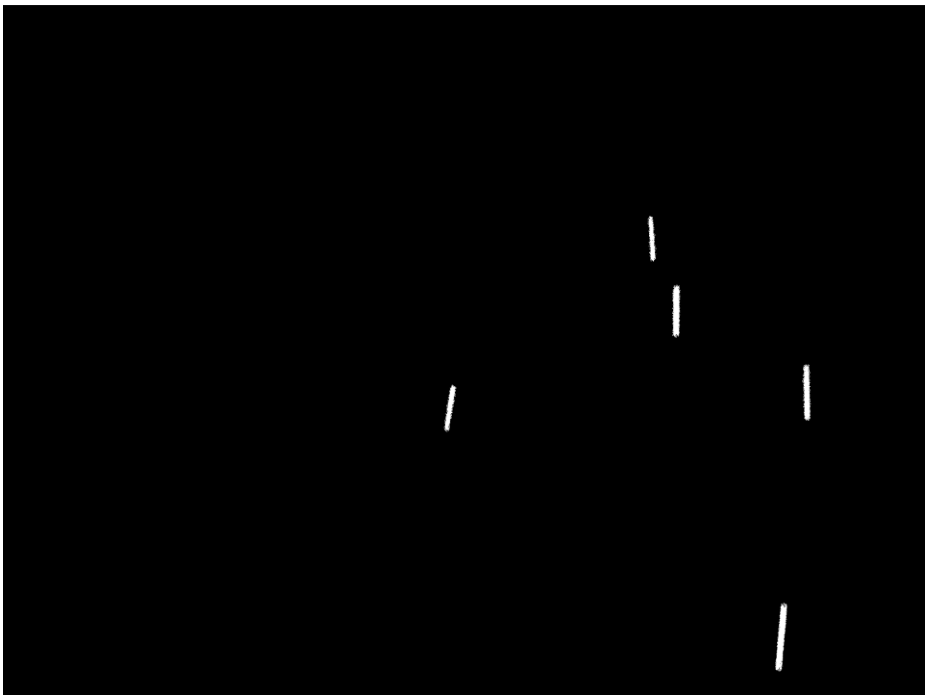

*Figure 62: Processed Sample Image from Atomization Test with a Shutter Speed of 1/2,000 s.*

After each image is processed and droplet streak data is saved a variety of figures can be created to analyze the velocity distribution of the data. Data is saved for total velocity magnitude, as well as vertical and horizontal components. For this atomization experiment, Figures 63-65 provide examples of different radial distributions. Figure 63 displays a plot of the horizontal speed component for each identified droplet across each of the 1,000 analyzed frames for the shutter speed of 1/2,000 s. Figure 64 displays a radial distribution of the average total speed. Figure 65 displays radial distributions of the vertical components of speed for droplets at different vertical elevations. Each of these figures could be made for the vertical component, horizontal component, or total velocity.

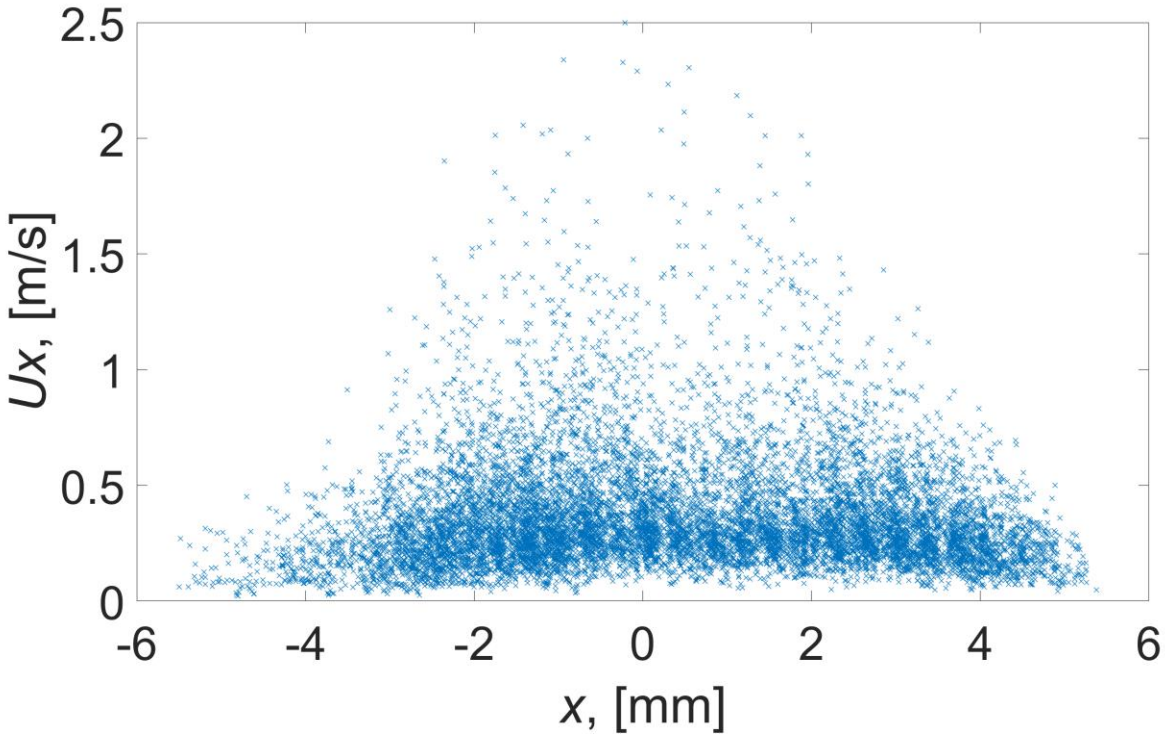


*Figure 63: Radial Location and Horizontal Speed for each Droplet.*

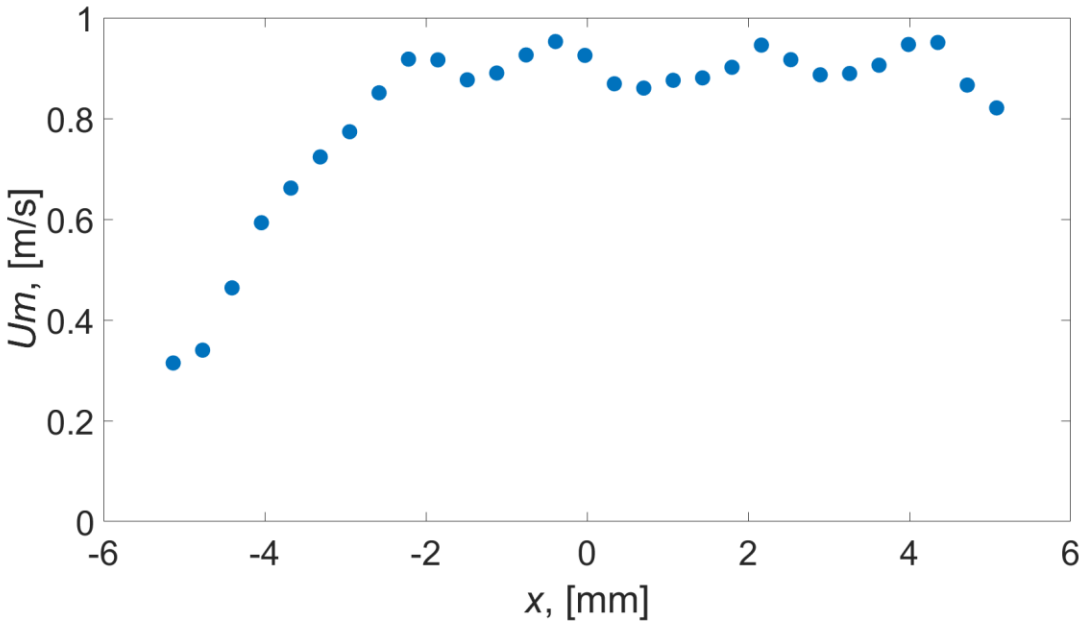


*Figure 64: Radial Distribution of Total Droplet Speed.*

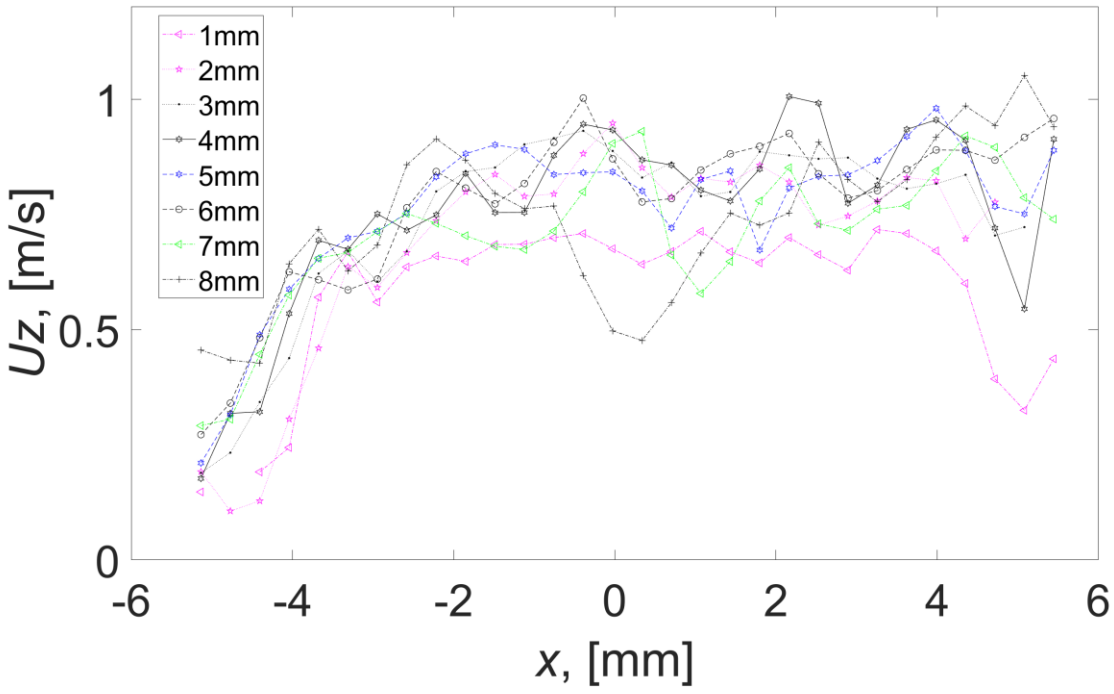


*Figure 65: Radial Distributions of Vertical Component of Droplet Speed at Different Elevations.*

While Figure 63 has a small percentage of outlier datapoints with relatively high horizontal speeds up to 2.5 m/s, the majority have speeds below 1 m/s across the frame. The droplets appear to become less dense in the leftmost quarter of Figure 63. Figures 64 and 65 also show a uniform magnitude for the majority of the frame except on the left. The left quarter of the frame appears to not capture the significant part of the droplet flow, meaning the camera is not perfectly centered. For these preliminary images, perfectly centering the camera is not critical since the images are used to test the droplet identification programs and not for creating a database. Additionally, Figure 65 does not show any significant differences in vertical velocity as vertical location changes, as shown by the different lines. While Figures 64 and 65 have random fluctuations, there are no clear peaks.

These preliminary results from the Virginia Tech facility for atomized droplets have demonstrated the capability of the droplet PSV program to identify and measure droplet velocity from intentional droplet streaks induced by a slow shutter speed. The PSV method works better than both the PIV and PTV methods due to the relatively low droplet fraction and fast droplet speed. The droplets are not dense enough for the PIV method to work well and the droplets move too fast to consistently track them between frames for the PTV method.

A false conclusion from the last atomization experiment and PSV program's preliminary results would be that 1/2,000 s is the ideal shutter speed for collecting velocity data to use in the PSV program. While it works well for the atomization setup, the RPI test facility produces droplets with much faster velocities and a range of velocities depending on the conditions tested. Therefore, when collecting velocity data, the high-speed cameras' live feeds must be monitored to determine an ideal shutter speed for each condition. The most important priority is to make sure the droplet

streaks are dark enough that they can easily be seen and do not blend into the background. Other goals with taking raw velocity images are to minimize the amount of overlapping droplets while maximizing the lengths of each streak. Faster shutter speeds lead to darker droplets and less droplets that overlap. Shorter shutter speeds lead to longer droplet streaks. This is a significant tradeoff to remember when collecting droplet velocity data.

# Chapter 6

# 6. Droplets in Annular Two-Phase Flow Experimentation

During March 2024, the high-speed imaging equipment listed in Table 6 was brought to the RPI annular flow test facility. The facility is built to operate water flow between 0.1 and 0.5 gallons per minute (gpm) and to operate air flow between 150 and 300 standard cubic feet per hour (scfh). While it is planned for at least 30 combinations of flow rates to eventually be tested, the present study collects data for nine combinations due to time constraints. The combinations of data collected in the present study are every combination of 0.1, 0.3, and 0.5 gpm of water with 180, 220, and 260 scfh of air. The water flow rate measurements have an uncertainty of 0.005 gpm and the air flow rate measurements have an uncertainty of 10 scfh. These values cover the whole range of water flowrate and most of the range of air flowrate. 180 scfh of air is chosen as the lowest tested value because lower values fail to produce many droplets. More precise correlations to determine if a significant number of droplets will be entrained based on the conditions is found in the literature [34]. An air flow of 260 scfh is chosen as the highest tested value because higher values result in droplet images with many overlapping droplets and fast droplets that induce motion blur even at the highest shutter speeds of the SA6 camera.

Superficial velocities are calculated based on the flowrate values for each run along with temperature, pressure, and pipe diameter. The internal diameter of the pipe is 9.525 mm, machined with a tolerance of 0.254 mm. The $j_f$ values are straightforward to calculate since water does not have a significant change in density for any of the relatively low pressures tested. Therefore, $j_f$ is

calculated by dividing by the pipe's internal cross-sectional area. From these calculations, the $j_f$ values for conditions tested range from 0.089 to 0.44 m/s.

The $j_g$ values are a little more complicated to calculate. They require converting the measured flow rate ($Q_1$) to the flow rate at standard condition ($Q_2$) with a formula from the Dwyer flowmeter's manual [35]. The standard flow rate is calculated as

$$Q_2 = Q_1 * \sqrt{\frac{P_1 * T_2}{P_2 * T_1}} \tag{9}$$

where $P_1$ is the actual pressure at the outlet of the flowmeter, $P_2$ is the standard pressure (14.7 psi), $T_1$ is the measured air temperature, and $T_2$ is the standard temperature (530 R). $P_1$ is calculated by adding the measured gage pressure to the atmospheric pressure at the RPI test facility. The measured pressure from the pressure gauge has an uncertainty of 0.5 psi. The atmospheric pressure is determined from weather data in Troy, New York during the time of testing. The atmospheric pressure did not change significantly during data collection and was 14.5 psi [36]. The compressed airline at RPI has a constant temperature of 70°F, or 530 R, so the temperatures can be cancelled out since they are the same, to simplify the equation as

$$Q_2 = Q_1 * \sqrt{\frac{P_1}{P_2}}. \tag{10}$$

Then, this standard flow is converted to the local flow rate ($Q_3$) by using the ideal gas law. Temperature can be assumed to remain constant and an equation for $Q_3$ can be written as

$$Q_3 = Q_2 * \frac{P_2}{P_3} \tag{11}$$

where $P_3$ is the pressure at the droplet measurement port. This pressure is equal to the atmospheric pressure of 14.5 psi since the pipe is open to the environment at this port. Equations 9-11 can be combined with 14.7 inputted for $P_2$ and 14.5 inputted for $P_3$ to be written as

$$Q_3 = 0.264 * Q_1 * \sqrt{P_1}. \quad (12)$$

Finally, to calculate the $j_g$ values, the calculated $Q_3$ value for each trial is divided by the pipe's internal cross-sectional area.

The $j_g$ values for the conditions tested range from 22.0 to 39.4 m/s. The superficial velocity combinations tested at the RPI test facility are plotted with red dots on the two-phase flow regime map in Figure 66 and are listed in Table 7. The uncertainties in Table 7 for $j_f$ are calculated based on the water flow rate uncertainty and pipe inner diameter tolerance. The uncertainties in for $j_g$ are calculated based on the pressure gauge uncertainty, air flow rate uncertainty, and pipe inner diameter tolerance. All of these points fall within the predicted entrainment portion of the annular flow regime on the map. This makes sense because all of the tested conditions produced droplets. Further, at slightly lower values for $j_g$ with the minimum $j_f$ tested, significant droplet entrainment did not occur. This observation is consistent with the prediction of the onset of entrainment model as shown in Figure 66 [11-12].

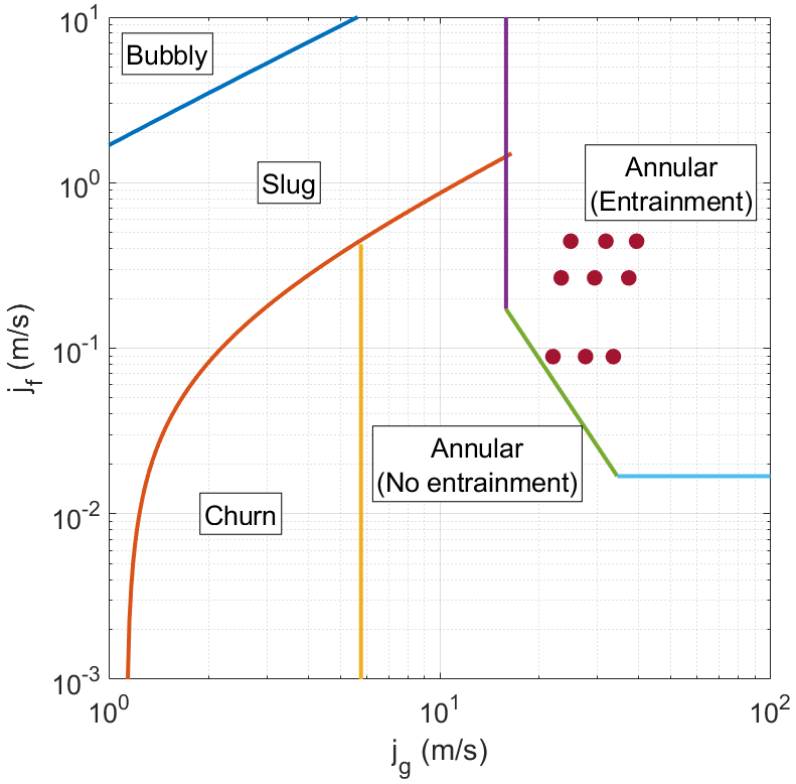


*Figure 66: Two-Phase Flow Regime Map with Tested Superficial Velocity Combinations Indicated with Red Points [10-11].*

*Table 7: Superficial Velocity Combinations Tested at RPI Test Facility.*

| Run | Liquid Superficial Velocity ($J_f$) (m/s) | Gas Superficial Velocity ($J_g$) (m/s) |
|---|---|---|
| 1 | 0.089 ± 0.009 | 22.0 ± 2.7 |
| 2 | 0.089 ± 0.009 | 27.6 ± 3.1 |
| 3 | 0.089 ± 0.009 | 33.5 ± 3.5 |
| 4 | 0.27 ± 0.019 | 23.3 ± 2.8 |
| 5 | 0.27 ± 0.019 | 29.4 ± 3.3 |
| 6 | 0.27 ± 0.019 | 37.3 ± 3.8 |
| 7 | 0.44 ± 0.028 | 24.9 ± 3.0 |
| 8 | 0.44 ± 0.028 | 31.8 ± 3.5 |
| 9 | 0.44 ± 0.028 | 39.4 ± 4.0 |

## 6.1 Test Facility at RPI

An overall schematic of the RPI test facility is displayed in Figure 67. The RPI annular flow test facility includes a vertical pipe with concurrent flow of air and water that flows upward. Air flows through the bottom of the two-phase injector unit in the perforated tube as seen in Figure 68. Water flows through opposite sides of the bottom of the two-phase injector unit and then up through the perforated tube as also seen in Figure 68. The water flow rate is adjusted with a needle valve and the air flow rate is adjusted with a ball valve. Both valves have flow meters and temperature sensors nearby. Additionally, the air inlet has a pressure gauge attached. The air pressure and temperature are important for calculating the local flow rate, which is needed to calculate $j_g$.

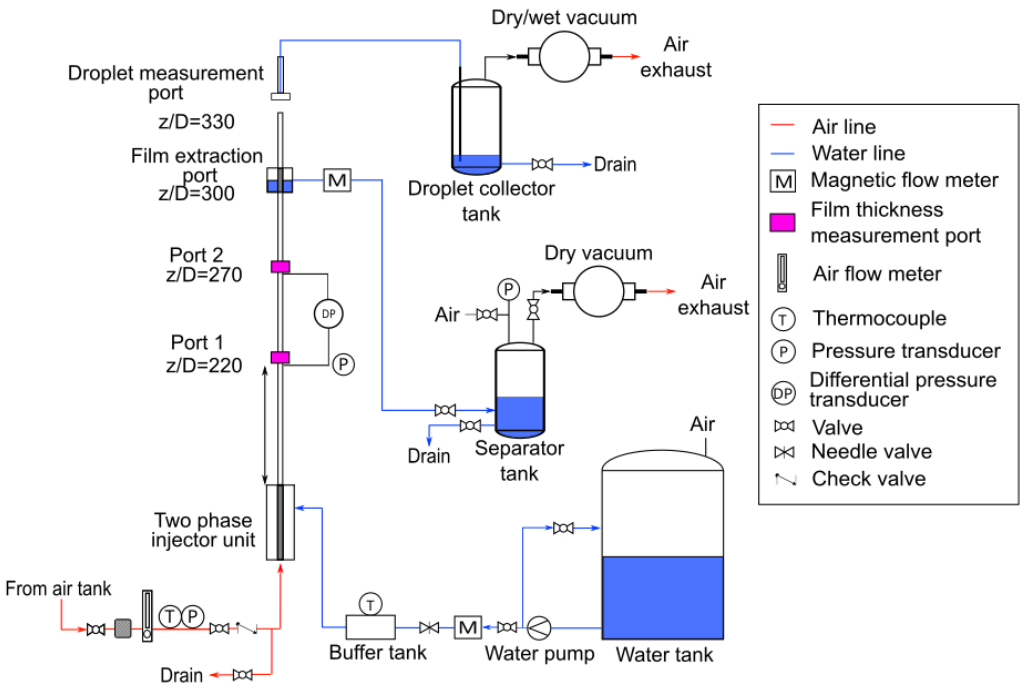


*Figure 67: Schematic of RPI test facility [12].*

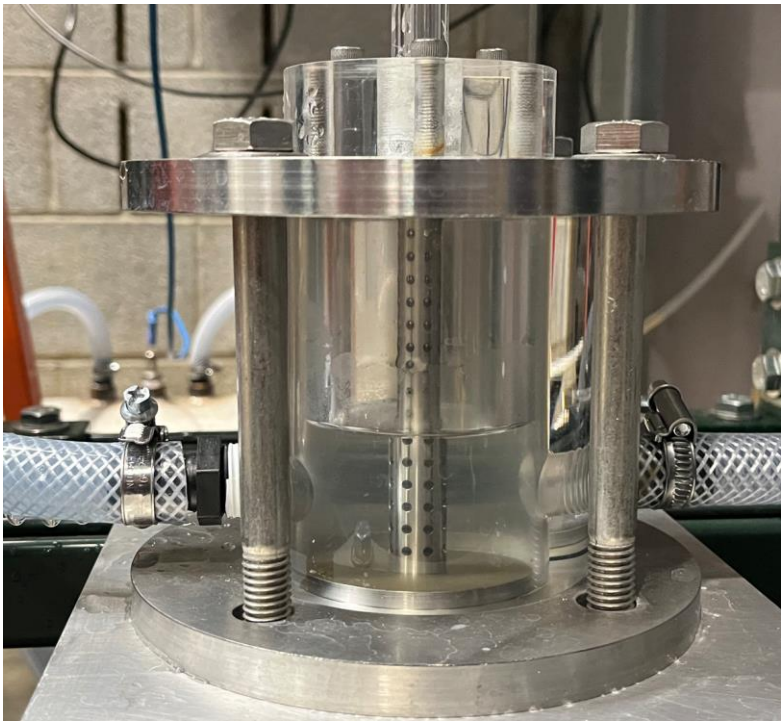

*Figure 68: Two-Phase Injector Unit.*

After the water and air enter the main pipe through the injector unit, the two-phase flow travels upward to film extraction port, pictured in Figure 69. Inside the film extraction port, the same perforated tube from the injector unit is used to allow the water from the film to escape. This tube is wrapped with steel mesh and a vacuum sucks water from the chamber. This setup allows the film to be removed without affecting the inner droplets. The tube that is connected to a vacuum pump can be seen at the bottom of Figure 69.

*Figure 69: Film Extraction Port.*

Right above the film extraction port is the droplet measurement port. The high-speed camera and lights are positioned at this height. A small section of tube comes out of the film extraction port leads to a small opening allows for image recording, as seen in Figure 70. This figure clearly shows the inner droplet stream. There also exists some larger droplets around the stream. These larger droplets are a result of a very thin film that forms in the short distance between the film extraction port and the opening where droplet deposition occurs. Figure 71 shows how the cameras and lights are aligned to record the droplet measurement port. The SA4 and SA6 cameras are placed 90 degrees apart and each have a light with diffusor paper on the opposite side of the droplet measurement port. The droplet measurement port is a distance of 330 $z/D_h$ or about 4 m above the ground.

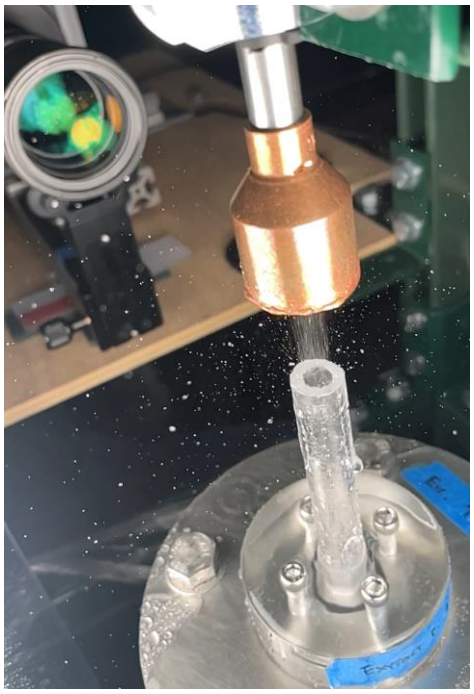

*Figure 70: Outlet of Film Extraction Port with Isolated Droplets.*

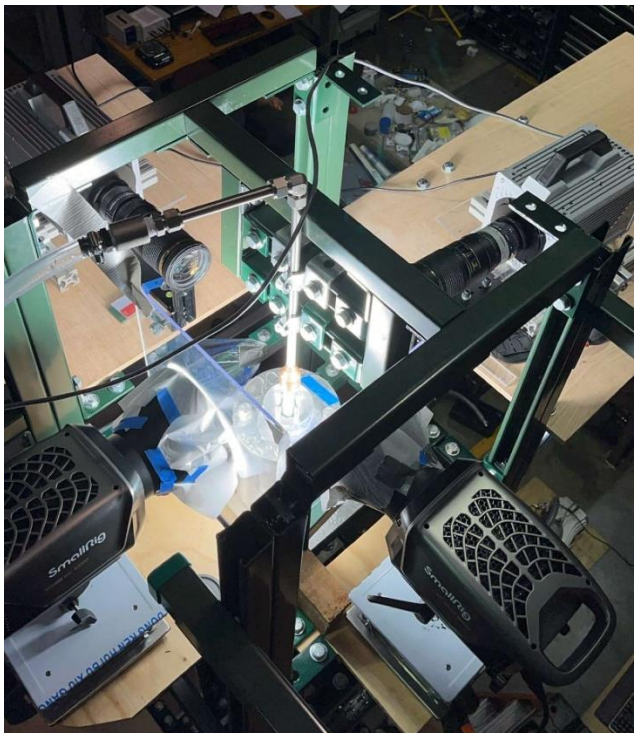


*Figure 71: High-Speed Cameras and Lights Recording Droplet Measurement Port.*

## 6.2 Annular Flow Droplet Calibration

Before and after collecting droplet data, the calibration process described in Chapter 3 is conducted. The calibration target is moved in 50 μm intervals a total of 41 times to span 2 mm centered around the approximated center of focus. This process is completed for both cameras. Figures 72 and 73 show the small particles and regions of the large particles analyzed for the SA4 camera and SA6 camera's calibration. Particles are chosen throughout different areas of the frame.

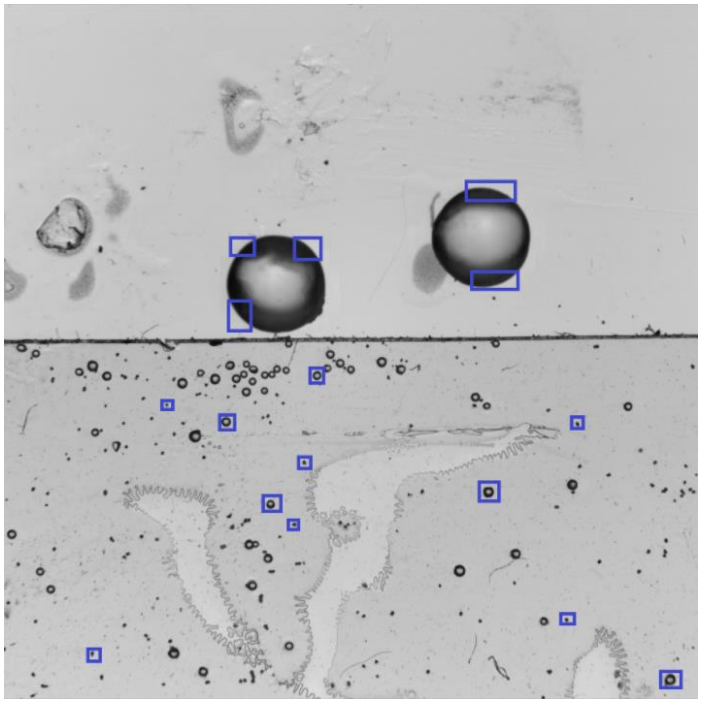

*Figure 72: Particles Analyzed in Depth-of-Field Calibration Testing for SA4 Camera.*

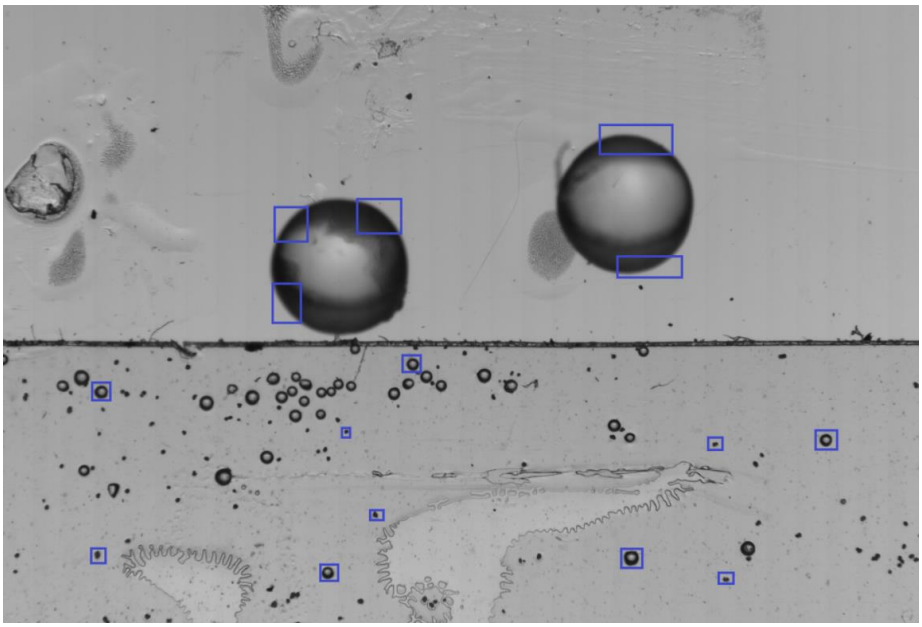

*Figure 73: Particles Analyzed in Depth-of-Field Calibration Testing for SA6 Camera.*

The results of the calibration process are important for three reasons. First, the calibration process helps ensure the cameras are centered and focused on the center of the droplet stream. This happens since the portion of the calibration target recorded is placed directly above the droplet outlet. The target is placed so the surface of the acrylic calibration target is above the middle of the outlet pipe. Second, the calibration process validates that the lighting conditions did not change significantly during the droplet data collection. Figures 74 and 75 show a comparison of the calibration results from before droplet testing (in blue) and after droplet testing (in red). Both of these plots show that the intensity gradient behavior of the calibration particles is similar for each camera before and after testing. Therefore, it can be concluded that the lighting conditions did not significantly change.

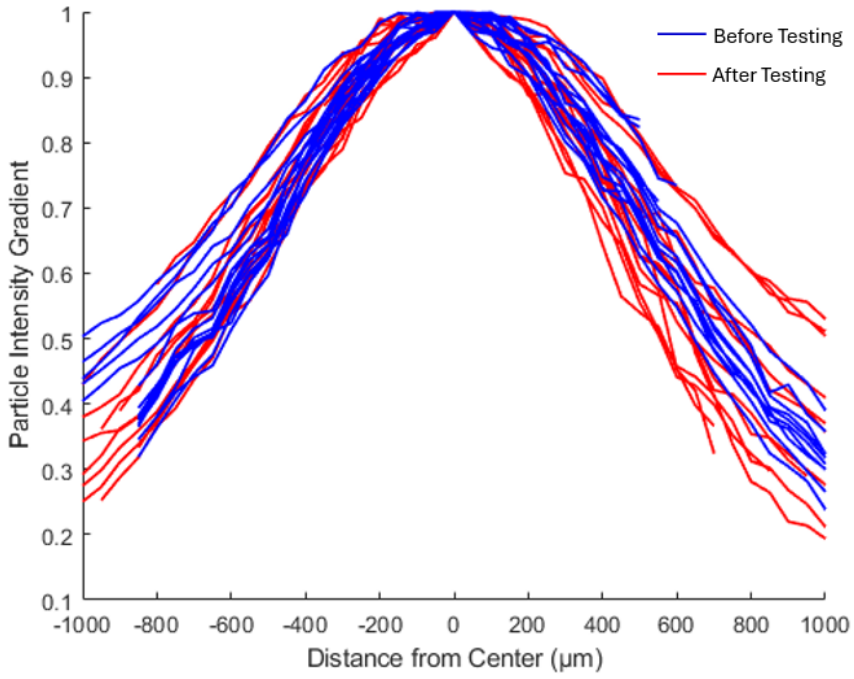


*Figure 74: Centered Normalized Particle Intensity Gradient of Particles on Calibration Target Before and After Testing for SA4 Camera.*

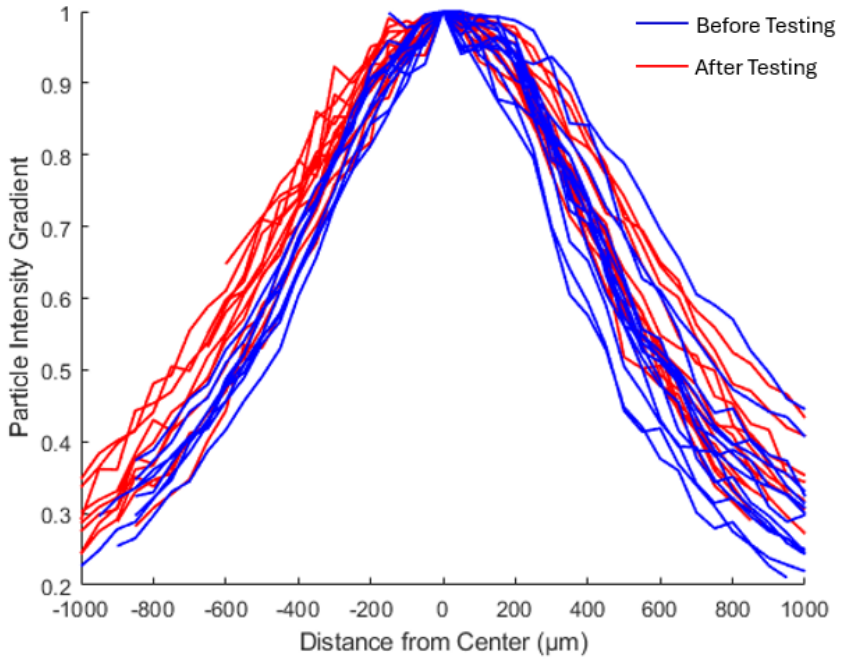


*Figure 75: Centered Normalized Particle Intensity Gradient of Particles on Calibration Target Before and After Testing for SA6 Camera.*

The last result of the calibration process is determining the intensity gradient threshold to filter between in and out-of-focus droplets for the data processing. Figures 76 and 77 show the average intensity gradient at different distances from the center focal plane for each camera. In theory, the focal plane is infinitesimally thin; however, a depth must be selected for real data analysis. A 0.70 threshold for images taken with the SA4 camera and a 0.78 threshold for images taken with the SA6 camera will be used. This corresponds to a focal plane depth of about 1 mm for the SA4 and about 0.7 mm for the SA6. These thresholds are selected because they correspond with the regions of the calibration curves with the maximum slopes. This means that the distance from the center is least sensitive to changes in intensity gradient at these thresholds. Regions of the graph towards the middle or either extreme, where the intensity gradient approaches zero, have flatter slopes, and are thus much more sensitive to changes in intensity gradient.

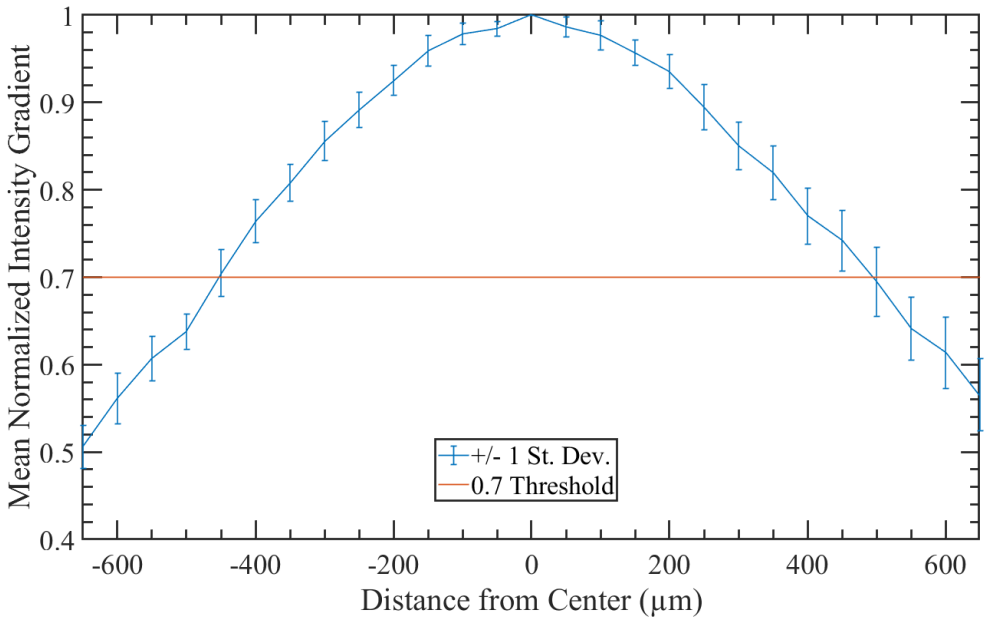


*Figure 76: Mean Normalized Particle Intensity Gradient with Threshold for SA4 Camera.*

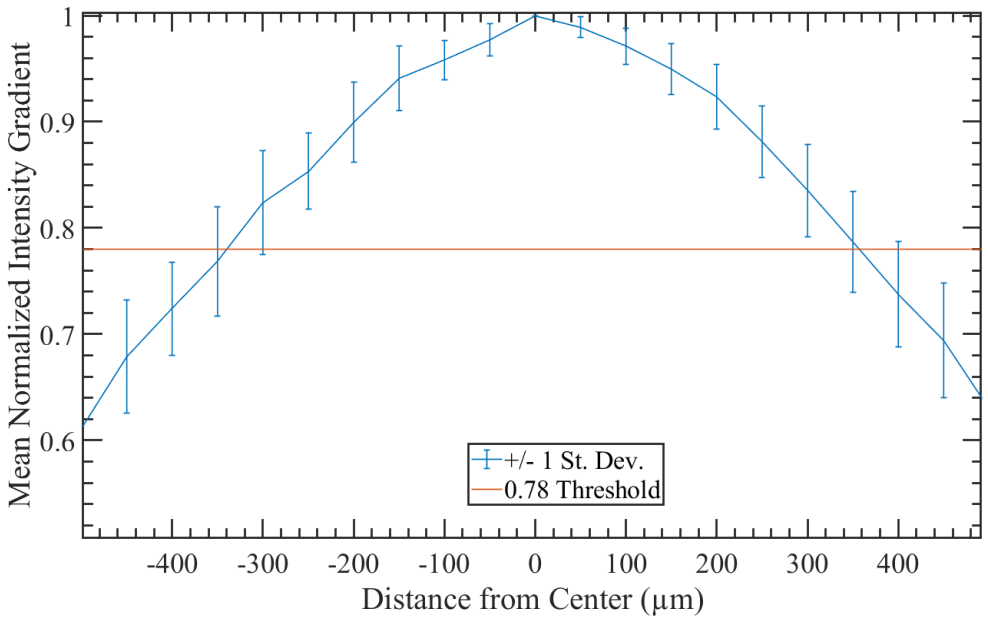


*Figure 77: Mean Normalized Particle Intensity Gradient with Threshold for SA6 Camera.*

## 6.3 Annular Flow Droplet Data

For each superficial velocity combination listed in Table 7, four sets of data are collected. Each trial involves recording images with each of the two high-speed cameras, for a total of eight datasets for each combination of superficial velocity. The first two repetitions in each set of four datasets per superficial velocity combination consist of images taken in the size imaging configuration at high shutter speeds. The last two repetitions in each set of four datasets per superficial velocity combination consist of images taken in the velocity imaging configuration at low shutter speeds. Every type of data for each condition is recorded twice to validate that the flow does not change with time since images are recorded for only a few seconds per repetition. Both cameras, which are placed 90 degrees apart, are used to collect data to verify that the radial distribution is axisymmetric.

All images are taken at the maximum resolution. The maxiumum resolution is 1,024 by 1,024 pixels for the SA4 camera and 1,920 by 1,440 pixels for the SA6 camera. The SA4 camera is placed so the front of its lens is 23.5 cm from the center of flow. The SA6 camera is placed so the front of its lens is 24.0 cm from the center of flow. These are the previously measured distances to achieve in-focus maximum resolution images with a 11 mm image width. This image width is chosen to be slightly larger than the 9.525 mm internal diameter of pipe to allow for a slight buffer in case images are recorded slightly off-center. Also, the image width corresponds to a physical size of 10.74 μm per pixel recorded by the SA4 camera and 5.73 μm per pixel recorded by the SA6 camera. These values are inputed into the droplet identification programs to convert pixel lengths to physical lengths. They are also used to determine an individual droplet's size uncertainity. When a droplet's diameter is calculated, the outer pixels on both ends correspond to the uncertainity in its calculation. The actual ends of each droplet's diameter are located somewhere within each outer pixel. Therefore, the droplet data from images captiured by the SA6 camera have an uncertainity of ± 0.01146 mm.

The maximum number of high resolution images that each camera can store at once are recorded for each repetition: 10,918 for the SA4 camera and 3,877 for the SA6 camera. It takes about 30 minutes for the images from both cameras to be saved on a computer hard drive. Since nine superficial velocitiy combinations are tested, 36 total experimental trials are conducted for a total of 532,620 total images between both cameras. Due to delays in the construction of the RPI test facility, not all images are able to be processed for the present study. The droplet identification programs have fairly high computational times. The present study processes and analyzes images captured for two different test conditions that have the same $j_f$. $J_g$ values of 22.0 and 33.5 m/s are analyzed in combination with a constant $j_f$ of 0.089 m/s. These conditions are runs 1 and 3 as

specified by Table 7. This allows for analysis of the effect of changing $j_g$. Additionally, only images captured by the SA6 camera are processed. These images are prioritized since they are higher resolution. All data will be processed in the future. For the two analyzed conditions, more distribution figures are located in Appendix B than are presented in this chapter. The radial distributions of size data contain error bars corresponding to one standard deviation. Both size and velocity data are studyed and processed for the two conditions for the present study.

A sample image from Run 3 is shown in Figure 78. This figure shows the raw image, the enhanced image when it is compared to the background, and the final image of identified droplets in the frame after being processed through the droplet idenfication program. While the droplets are hard to identify in the dark raw image in Figure 78(a), the enhanced image in Figure 78(b) shows that data for individual droplets can be isolated. This is further verified by the outlined droplets that are identified in Figure 78(c).

(a) 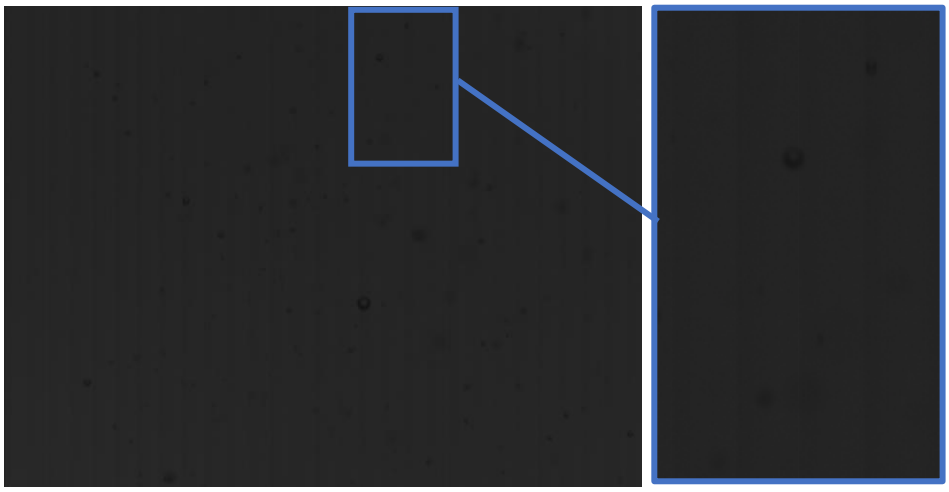

(b)

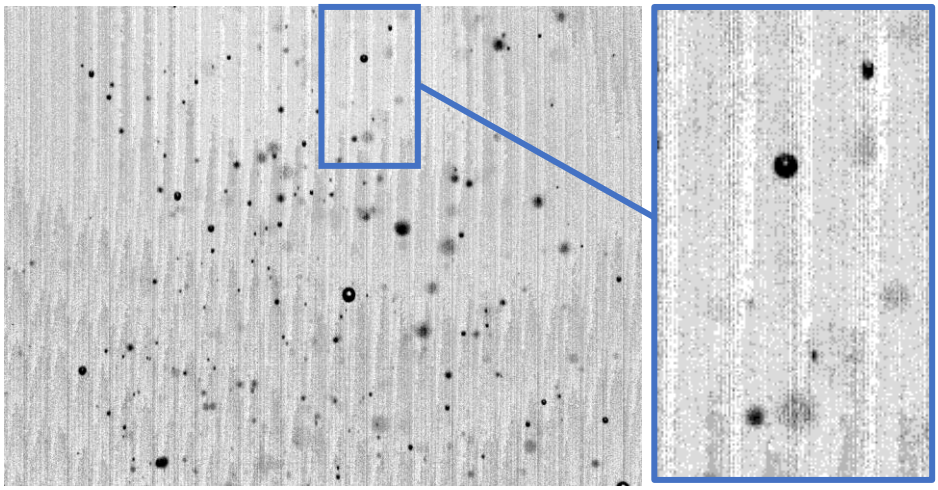

(c)

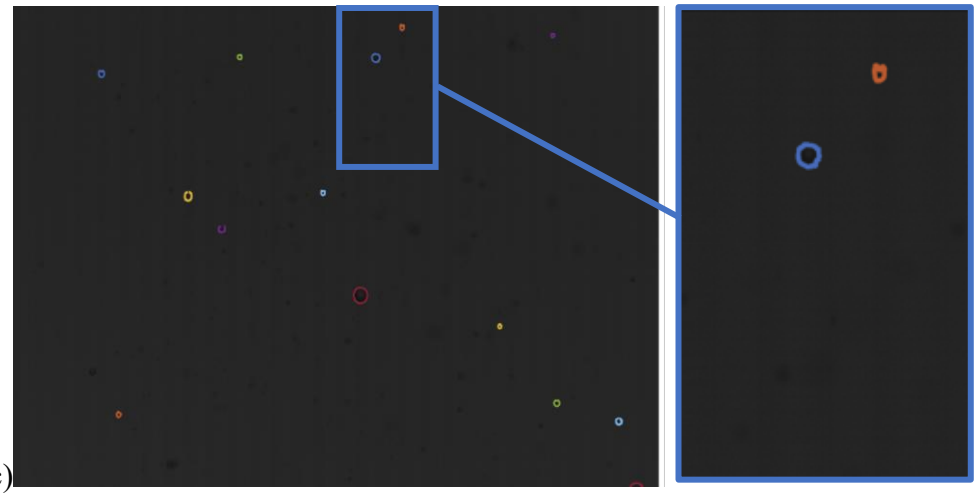

*Figure 78: Sample Image with Enlarged Portion from Run 3 Processed Through Droplet Identification Size Program with (a) raw image, (b) enhanced image, and (c) final identified droplets.*

The results for both runs tested are similar for each of the repeated repetition. For instance, Figure 79 shows the droplet fraction radial distribution for the two size data repetitions for run 3. These distributions both have peaks slightly to the left of the center. The slope also appears to be steeper on the right side of the distribution than the left for both repetitions. A potential reason for this asymmetric behavior could be the vacuum from the film extraction port sucking some droplets

from one side. Both distributions appear to have one distinct peak, similar to the number density distributions such as the one shown in Figure 80.

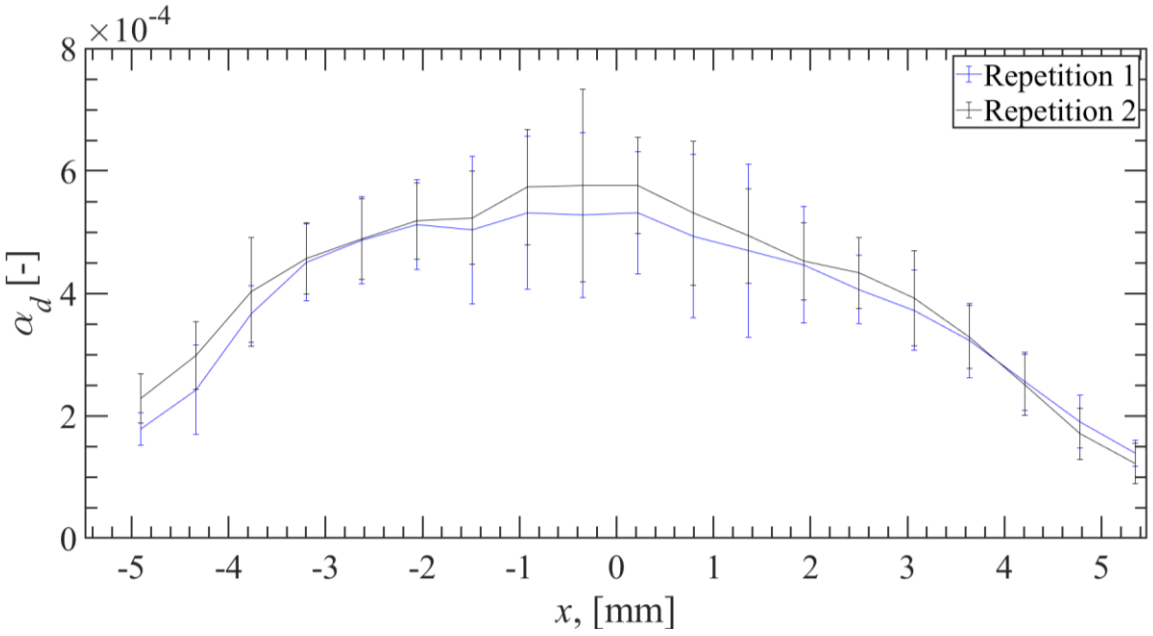


*Figure 79: Droplet Fraction Radial Distribution for Both Repetitions for Run 3 with Error Bars Corresponding to 1 Standard Deviation.*

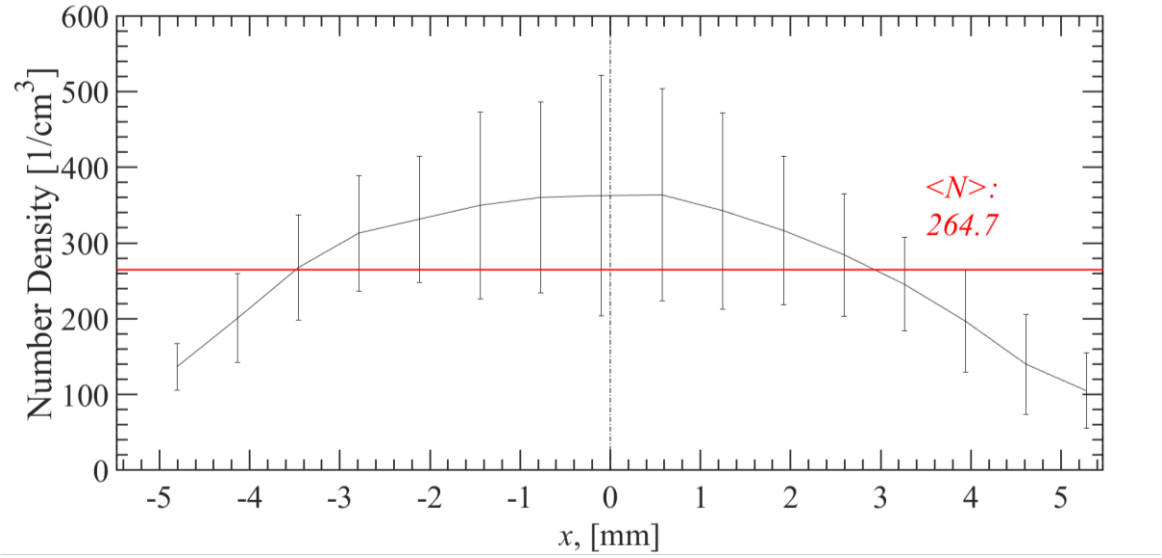


*Figure 80: Droplet Number Density Radial Distribution for First Repetition of Run 3 with Error Bars Corresponding to 1 Standard Deviation.*

There are a couple important contrasting features when the droplet fraction distributions from Figure 79 are compared to droplet fraction distributions when $j_g$ is decreased to 22.0 m/s in run 1, such as one of the repetitions in Figure 81. First, the maximum droplet fraction and area-averaged droplet fraction are both significantly lower than those observed when $j_g$ was higher in run 3. This means that fewer droplets were produced with these testing conditions. Second, the droplet fraction distribution does not have a single, distinct peak with the lower $j_g$ in run 1. Instead, there appear to be a central peak and then one additional peak on each side. This trend does not appear on the droplet number density curve for run 1, as shown in Figure 82. This could mean that many of the relatively large droplets exist in de-centralized peaks from Figure 81. Large droplets affect droplet fraction much more than overall droplet number density due to their large volume. This could also be a result of the lower droplet fraction leading to data with more fluctuations with the lower $j_g$.

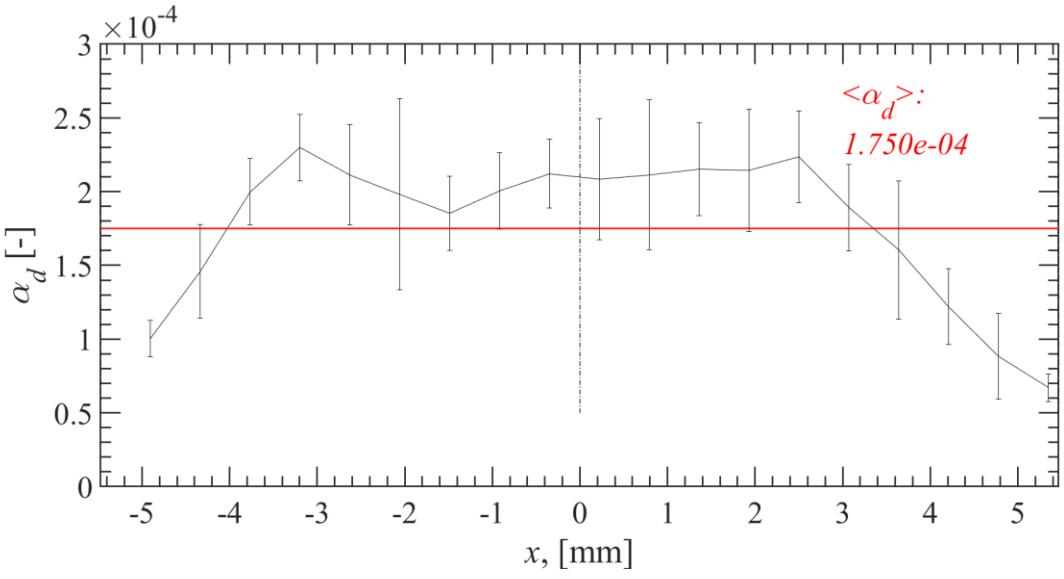


*Figure 81: Droplet Fraction Radial Distribution from First Repetition of Run 1 with Error Bars Corresponding to 1 Standard Deviation.*

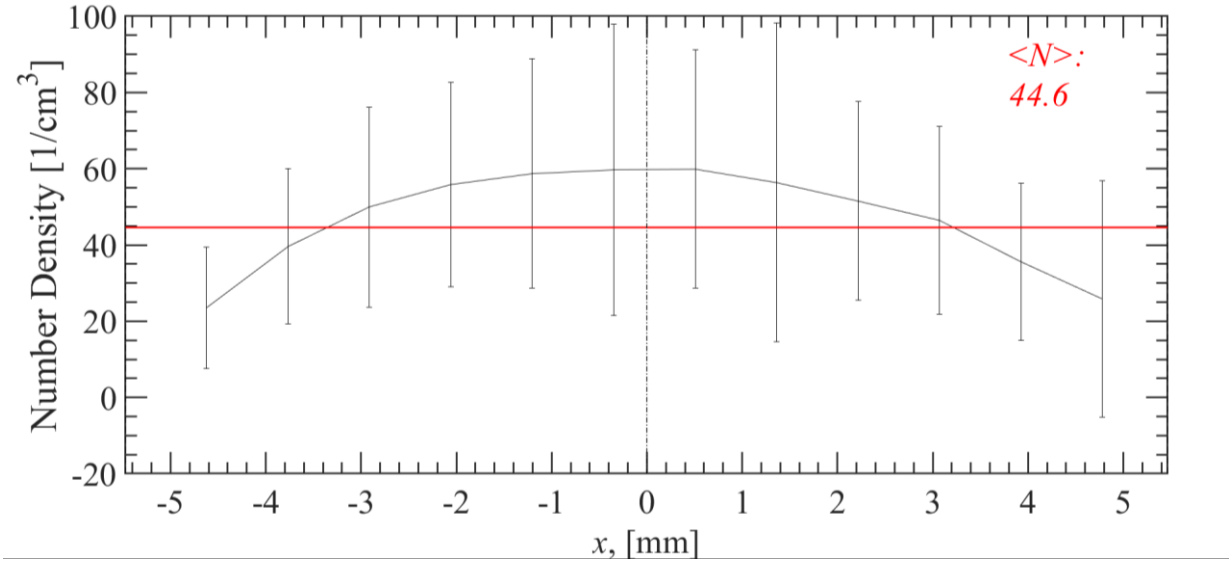


*Figure 82: Droplet Number Density Radial Distribution from First Repetition of Run 1 with Error Bars Corresponding to 1 Standard Deviation.*

The final important difference is that there are significantly more droplets with the higher $j_g$ in run 3. This can be seen clearly in Figure 83, which present a droplet size distribution plot with data from both repetitions for both conditions. The horizontal axis of Figure 83 has a minimum diameter of 0.03 mm because the majority of droplets less than 0.03 mm are filtered out in the droplet identification program because they are not distinguishable from background noise. Both distributions have peaks at similar locations, but the lower $j_g$ distribution has a significantly less steep slope to the right of the peak. The difference between the number of droplets in size ranges towards the peak is about an order of magnitude. On the other hand, the difference is much less far away from the peak. This provides evidence that the lower $j_g$ in run 1 has a larger percentage of larger droplets. The median average droplet diameter for run 3 is about 0.14 mm compared to 0.20 mm for run 1.

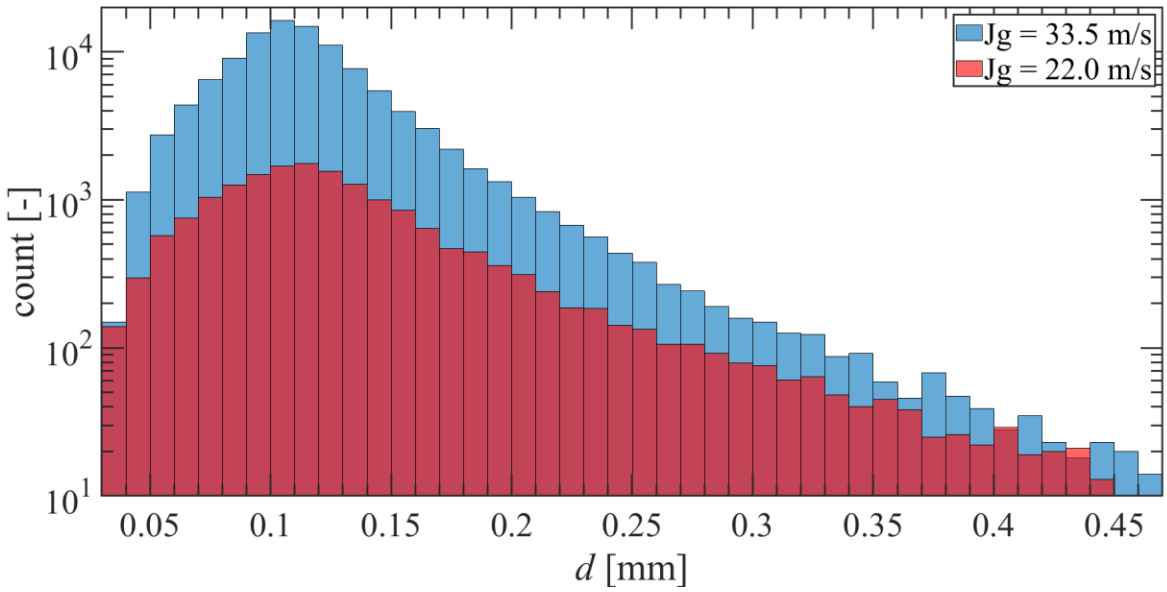


*Figure 83: Droplet Size Distribution with Data from Both Repetitions from Run 1 (red) and Run 3 (blue); jf Held Constant at 0.089 m/s.*

Another important comparison can be made with the theoretical droplet size distributions that were presented in Chapter 1. The present study is the first time these models have been compared to droplet data captured with high resolution cameras. Table 8 displays the volumetric median diameter ($D_{vm}$) estimates from both distributions from the literature for the conditions from run 1 and run 3 [13-14]. The volumetric median diameter is the droplet size where 50% of liquid is contained in smaller droplets. The table also includes the experimental values for each repetition of these conditions. It is interesting that the experimental values from the condition with the higher $j_g$ are close to the distribution created by Kocamustafaogullari et al., while the distribution created by Kataoka et al. is closer to the experimental data for the lower $j_g$ [13-14]. This trend can also be noted in Table 9, which displays the percent difference between the average of each pair of repetition and the theoretical $D_{vm}$ values.

*Table 8: $D_{vm}$ Estimates from Theoretical Distributions and Experimental Values from each Repetition of Runs 1 and 3 [13-14].*

| Run | Kataoka et al. $D_{vm}$ Estimate (mm) [13] | Kocamustafaogullari et al. $D_{vm}$ Estimate (mm) [14] | 1st Repetition $D_{vm}$ (mm) | 2nd Repetition $D_{vm}$ (mm) |
|---|---|---|---|---|
| 1 | 0.4263 | 0.2779 | 0.3660 ± 0.011 | 0.3861 ± 0.011 |
| 3 | 0.2433 | 0.1877 | 0.1729 ± 0.011 | 0.1857 ± 0.011 |

*Table 9: Average Experimental $D_{vm}$ and Percent Difference from Theoretical Distributions of Runs 1 and 3 [13-14].*

| Run | Average Experimental $D_{vm}$ (mm) | Percent Difference Between Experimental Average and Kataoka et al. $D_{vm}$ Estimate [13] | Percent Difference Between Experimental Average and Kocamustafaogullari et al. $D_{vm}$ Estimate [14] |
|---|---|---|---|
| 1 | 0.3761 | 11.8% | 35.3% |
| 3 | 0.1793 | 26.3% | 4.48% |

Further comparisons to the models from the literature are presented in Figure 84, Figure 85, and Table 10. Figures 84 and 85 are CDF plots of the volume as diameter changes. Experimental data is plotted along with both models from the literature [13-14]. Figure 84 shows these distributions for the conditions tested in run 1. Likewise, Figure 85 shows the distributions for the conditions tested in run 3. The experimental data in these figures include data from both repetitions. In both analyzed runs, the experimental data seems to follow the distribution developed by Kataoka et al. at low and high diameters but approach the distribution developed by Kocamustafaogullari et al. for diameters in the middle, especially between 0.15 and 0.3 mm.

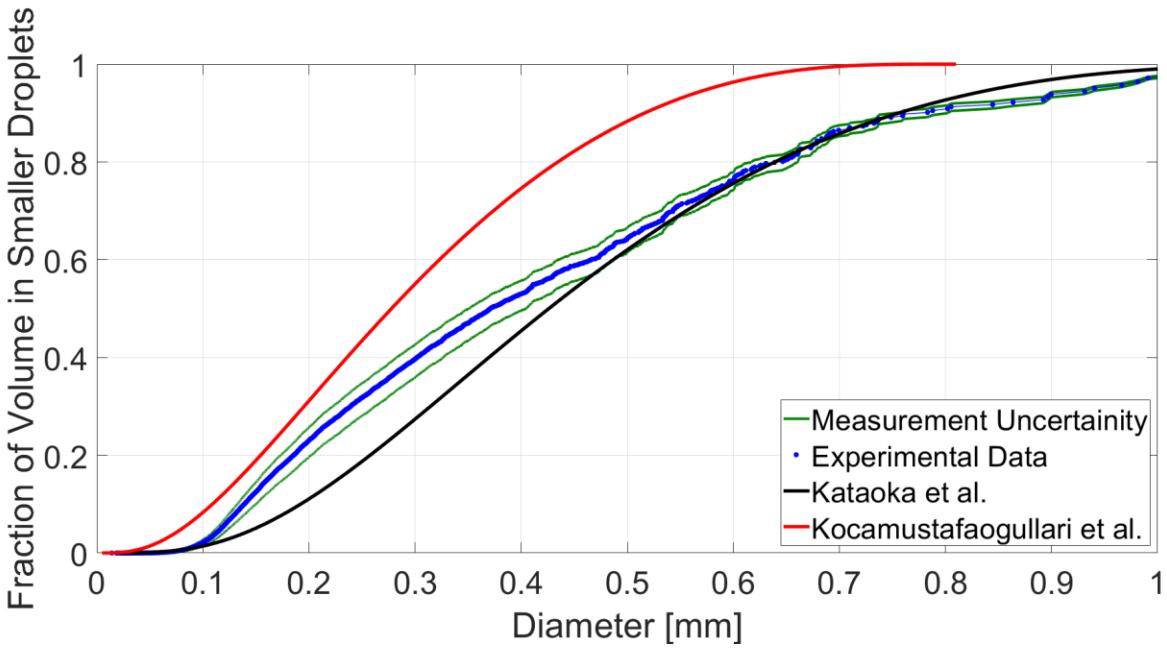


*Figure 84: CDF of Droplet Volume for Run 1 of Experimental Data and Theoretical Distributions from Literature [13-14].*

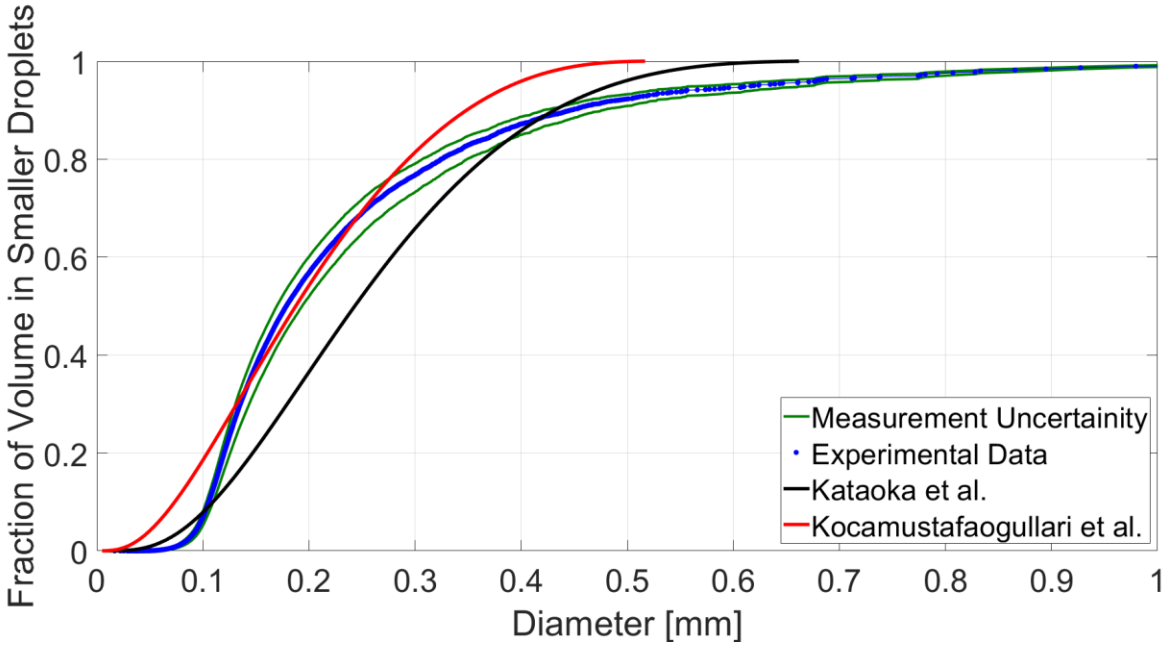


*Figure 85: CDF of Droplet Volume for Run 3 of Experimental Data and Theoretical Distributions from Literature [13-14].*

To quantify the difference between the experimental data and the literature distributions, root mean square error (RMSE) are calculated for each run between the experimental data and each theoretical distribution. Similar to the $D_{vm}$ analysis, the model developed by Kataoka et al. performs better for the run 1 conditions with a lower $j_g$ than the model developed by Kocamustafaogullari et al. The model developed by Kocamustafaogullari et al. performs better for the run 3 conditions with a higher $j_g$ than the model developed by Kataoka et al. Another observation is that the model developed by Kataoka et al. performs consistently with a similar RMSE value for both runs. On the other hand, the model developed by Kocamustafaogullari et al. performs significantly better for run 3 than run 1.

*Table 10: RMSE Between Experimental Data and Theoretical Distributions from Literature for Runs 1 and 3 [13-14].*

| Run | RMSE Between Experimental Data and Kataoka et al. Distribution [13] | RMSE Between Experimental Data and Kocamustafaogullari et al. Distribution [14] |
|---|---|---|
| 1 | 0.0496 mm | 0.1375 mm |
| 3 | 0.0484 mm | 0.0357 mm |

Velocity distributions of the magnitudes of total velocity, the horizontal component of velocity, and the vertical component of velocity are created for both conditions from the PSV program. Like the size distributions, the velocity distributions are similar between repetitions of the same condition. Figure 86 displays the radial distribution of total speed for the first repetition of runs 1 and 3. The distribution from run 3 has much higher velocity values and a maximum value that is almost three times larger than the distribution from run 1. Another observation is that the run 3 distribution appears to have one middle peak, while the run 1 distribution seems to have multiple smaller peaks. The vertical speed is an order of magnitude higher than the horizontal

speed for both testing conditions. Therefore, the vertical speed distributions are very similar to the total speed distributions. These distributions can be found with the others in Appendix B.

The maximum values of the total and vertical speed distributions are lower than initial estimates prior to analyzing the data. They were predicted to be closer to the $j_g$ of each run. One reason for this discrepancy could be that the vacuum suction from the film extraction port slowed the flow right before the droplet measurement port. A second reason could be that the speed significantly decreases as a result of the flow travelling through the open air for a few centimeters between the pipe outlet and the imaging plane. This small distance was required to eliminate the majority of unwanted large droplets from the secondary film.

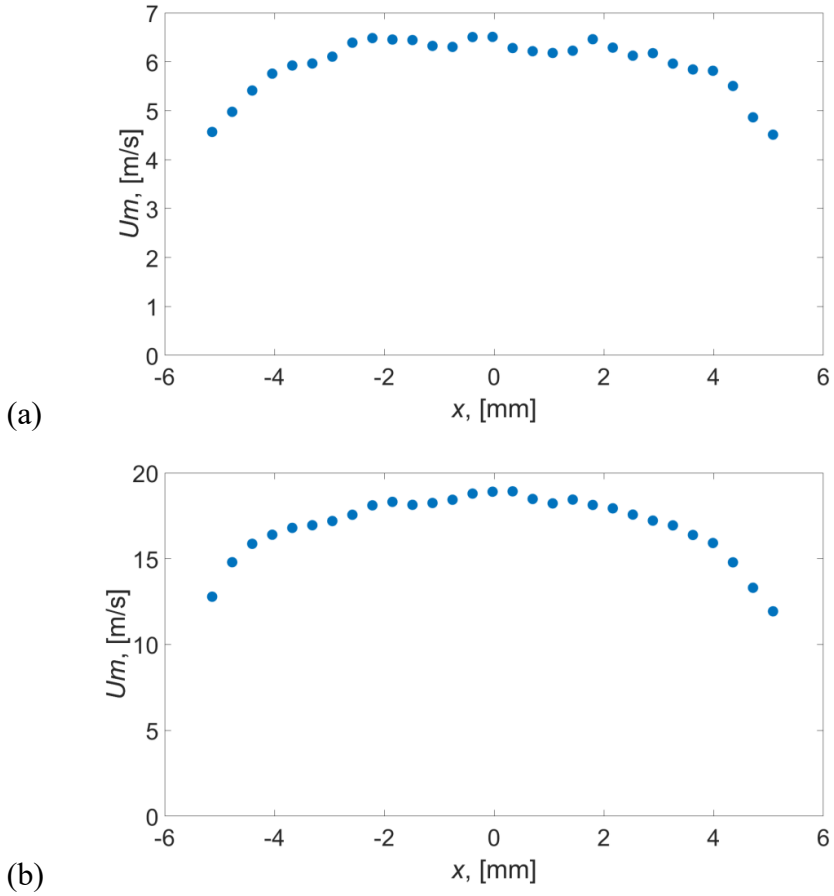


*Figure 86: Total Speed Radial Distribution from One Repetition of (a) Run 1 and (b) Run 3.*

Figure 87 displays the radial distribution of horizontal speed for the first repetition of each condition. The horizontal speed distributions exhibit some differences from the total and vertical speed distributions, besides being an order of magnitude smaller. While they experience peaks towards the center, they also all have sharp increases on either extreme side approaching the edge of each frame. This could be a result of droplets that recently separated from the film prior to the film extraction that are moving towards the center of flow. This could also be a result of droplets travelling towards the circumference of the pipe to deposit on the film. Another difference from the total and vertical speed distributions is that the center peaks for both conditions and each repetition do not show as significant of a central peak as the total speed and vertical speed radial distributions. Other than the extreme ends, the run 1 horizontal speed distribution is much flatter than the run 3 distribution.

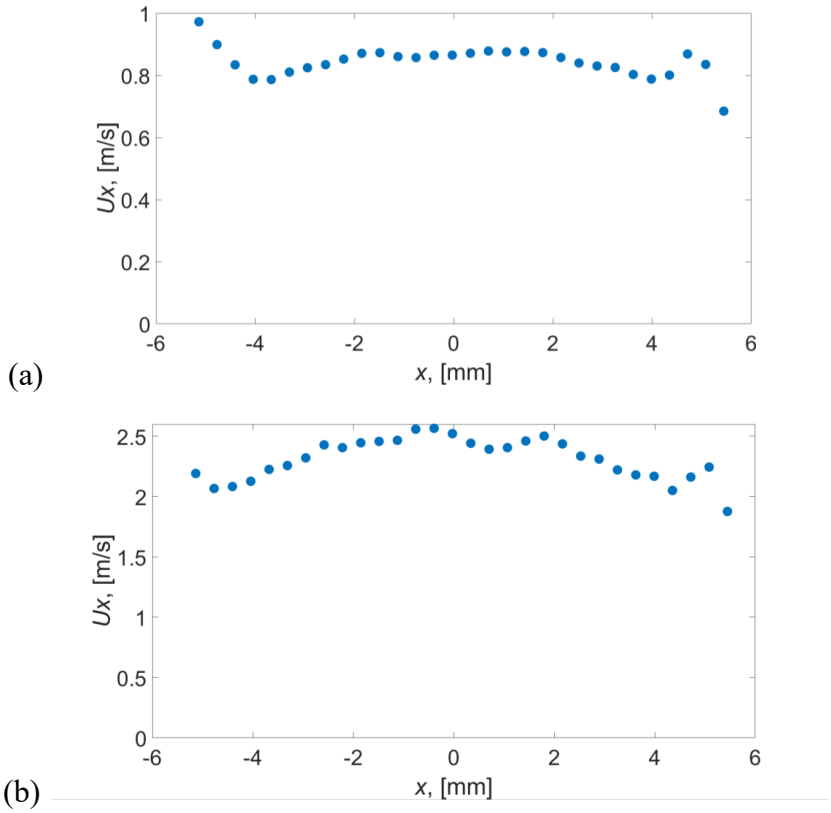


*Figure 87: Horizontal Speed Radial Distribution from One Repetition of (a) Run 1 and (b) Run 3.*

# Chapter 7

# 7. Conclusions and Future Work

## 7.1 Conclusions

The present study has outlined effective techniques to capture and process droplet data from the annular regime of two-phase flow. The study is the first to analyze entire frames of droplets in annular flow captured by a high-resolution camera. The study began with an overview of how the camera, lens, lens accessories, and lights were tested to ensure a compatible combination would be selected to capture droplets exiting a 9.525 mm pipe. Then, a calibration procedure was created for two critical reasons. First, the results from this procedure help determine the distance from the center of the focal plane of any pictured droplet. This is important because droplets that are far from the focal plane appear in recorded images with a significantly different size than their true physical size. They need to be filtered out. They are filtered by using an intensity gradient threshold, which analyzes the outline of each droplet. The second goal for the calibration procedure is to validate if the lighting conditions did not change significantly during the duration of testing. Calibration images are taken at the beginning and ending of testing and compared after they are processed through the calibration program.

The calibration target was meticulously created in a way that can be replicated in the future. The target contains glass beads with a similar index of refraction to water. Stationary particles are

needed so they can be moved in precise length increments to change the distance from the camera. A range of sizes are included to ensure larger particles, where refraction is dominant, and smaller particles, where scattering is dominant, are both tested. The smaller particles are between 50 and 300 μm in diameter and the larger particles are 1600 μm in diameter. All particles are attached to a transparent acrylic block. The smaller particles are attached with a piece of tape and the larger particles are attached by dipping them in a small amount of super glue with tweezers before placement on the acrylic block. The different sized particles need to be attached with different ways to avoid air bubbles that would form if the larger particles were placed under tape. The small particles are too small to be held by tweezers.

After initial calibration, droplet data can be recorded. The data tested in the present study includes images of droplets created by a commercial atomization nozzle and droplets in annular flow at the RPI test facility. The droplets in annular flow were collected for liquid superficial velocities ranging from 0.089 to 0.44 m/s and gas superficial velocities ranging from 22 to 40 m/s at 21°C and 1 atm. At the RPI facility, two cameras collected images simultaneously 90 degrees apart. Every testing condition was repeated with data recorded for two repetitions.

The images from all tests were processed through the droplet identification program. The program has two key components: the droplet size identification algorithms and droplet velocity PSV algorithms. The droplet size algorithms identify the outlines of in-focus droplets and record data to create size and radial distributions from images with a low exposure time. The PSV algorithms use images with a long exposure time to create intentional blurred streaks. The streak length is used to determine each droplet's velocity. Once each droplet is analyzed individually, radial velocity distributions are created.

The processed data of droplets created from the atomization nozzle demonstrated the initial effectiveness of the setup and identification program. The majority of droplets were between 100 and 150 μm. This narrow range is reasonable because the commercial atomization nozzle is designed to create droplets of that specific size range. The radial distributions for this data had random fluctuations but showed a generally uniform spatial distribution without significant peaks for both size and velocity data. Further testing of droplets close to the nozzle outlet showed that droplet identification program can not accurately process developing flow. The data collected at the RPI test facility was fully developed.

Images for two conditions collected at the RPI facility have been processed with many distributions displayed in Appendix B. These two conditions both have $j_f$ held constant at 0.089 m/s while changing $j_g$ between 22.0 and 35.5 m/s. Compared to the data from the droplets produced by the atomization nozzle, the size distributions of the annular flow data have clear peaks, especially for the higher $j_g$. The lower $j_g$ sized distribution has multiple smaller peaks towards the middle of the flow, while the higher $j_g$ has one larger central peak. The higher $j_g$ testing condition also produced flow with significantly more droplets. This was expected because increased air flow rate leads to more droplet entrainment. The lower $j_g$ contained a larger percentage of larger droplets than the higher $j_g$. The increased air flow leads to more instances of larger droplet breakups into multiple smaller droplets.

The droplet size distribution data from both conditions are also compared to theoretical droplet size distributions from the literature. The experimental results are closer to the distribution developed by Kocamustafaogullari et al. for the higher $j_g$ condition in run 1, but closer to the distribution created by Kataoka et al. for the lower $j_g$ condition in run 3 [13-14]. Once more data

is processed, these models can be evaluated further to determine if this trend continues for varying $j_g$ and if a trend emerges for which model performs better for higher values of $j_f$.

The velocity distributions from the RPI data also led to more conclusions. As expected, the higher $j_g$ leads to faster moving droplets, with speeds about three times faster than the lower tested $j_g$. Another observation is that the majority of total velocity is from the vertical component since the vertical component of velocity is about ten times larger than the horizontal component for both conditions. However, the horizontal component is very important since it is related to the rate of droplet deposition back on the film and of new droplet entrainment from the film. The cause for the lower than predicted vertical speeds will continue to be investigated.

## 7.2 Future Work

There are several ways to further this study to continue to collect and process annular two-phase flow data. First, raw images from the SA4 camera that were collected but not processed will be processed through the droplet identification programs. Including data from the SA4 camera will provide more data for each condition and verify if the RPI test facility produced axisymmetric droplet flow when the results are compared to results from the SA6 camera, position 90 degrees apart. Second, images from the other seven testing conditions will be processed and analyzed. This will allow for data and distributions to be analyzed for a much wider range of conditions. It will also study the effects of changing $j_f$, which was constant for the annular flow data analyzed in the present study. More data can also be collected at the RPI annular flow facility for more conditions than the nine already tested. This data will be compared with the theoretical droplet size

distribution models from the literature. Further, more data with the same conditions already tested can be collected to create a larger database for each condition.

Additionally, the droplet identification programs could be improved to extract more data from each raw image. Currently, the program is very good at identifying droplets between 50 and 200 μm. However, it has trouble identifying larger droplets due to the focal plane intensity gradient filters. Some droplets that are elliptically shaped and appear on the edge of the chosen focal plane depth appear only partially in-focus. The droplet identification program does not include these droplets in the final dataset because a full, connected ellipse is not formed. Larger droplets are more likely to experience this effect since they are more likely to cross one of the focal plane depth borders. Therefore, it is predicted that more data can be extracted per image, especially for large droplets, if the program processes droplets in different size ranges separately. The focal plane intensity gradient filters can be modified to include large droplets on the border that are not currently considered completely in-focus.

A second potential improvement to the droplet identification program could be modifying the PSV program to create velocity distributions with direction. Since the droplets are moving upwards, this can be used to determine the overall velocity direction and thus, the direction of the horizontal component of velocity. This would be useful to determine because it relates to the droplet deposition rates on the film.

There is also an important improvement that could be made to the RPI annular flow test facility. Currently, the droplet port is a few inches above the outlet of the film extraction port. This leads to a very thin, but existent, film that forms on the short pipe above the droplet extraction port as seen in Figure 88. When droplets travel out of the pipe into the opening to record images, some water from this thin film also escapes. The water from this film forms droplets that are significantly

larger than the inner droplets that are intended to be recorded. They also appear out-of-focus. Therefore, they are filtered out in the droplet identification program but can block in-focus droplets behind them. The camera is focused on the top of the opening to minimize the number of droplets from the film that appear in images. However, if the camera platform and film extraction port area of the RPI test facility is redesigned to align the camera's lens height with the height of the film extraction port's outlet, the small pipe will be removed, and a thin film will not form above the film extraction port. This would prevent areas from the raw images that are unusable due to large droplets from a secondary film.  Currently, most images do not experience any droplets from this thin film but an example of an image that contains the large out-of-focus droplet can be seen in Figure 89.

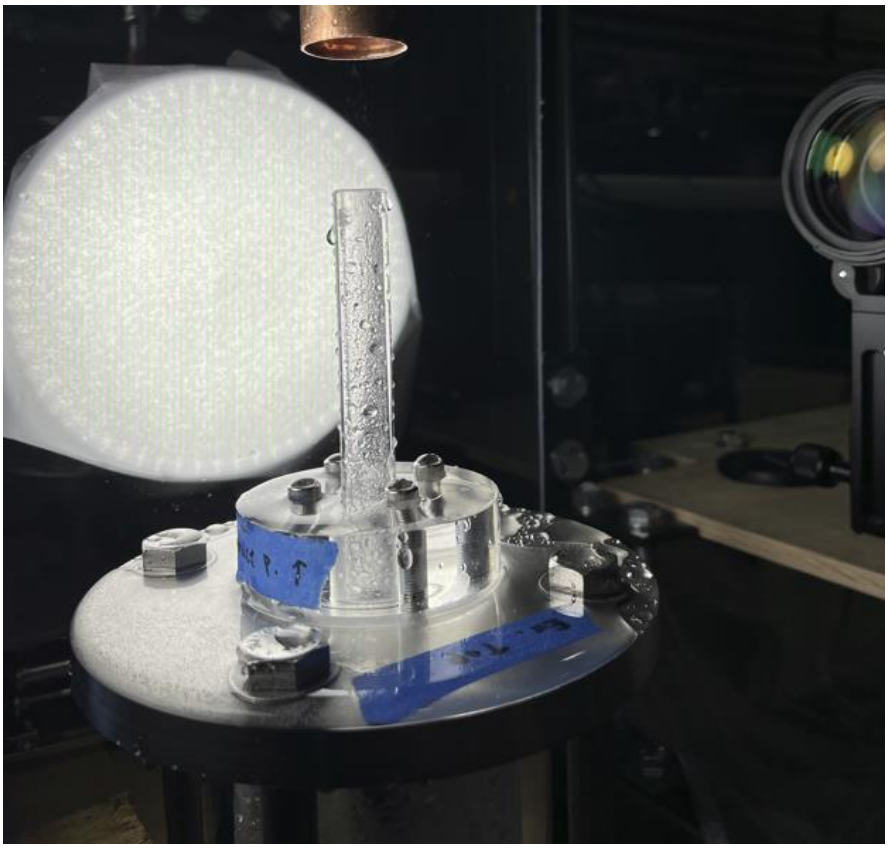

*Figure 88: Droplet Measurement Port with Outlet Pipe from Film Extraction Port.*

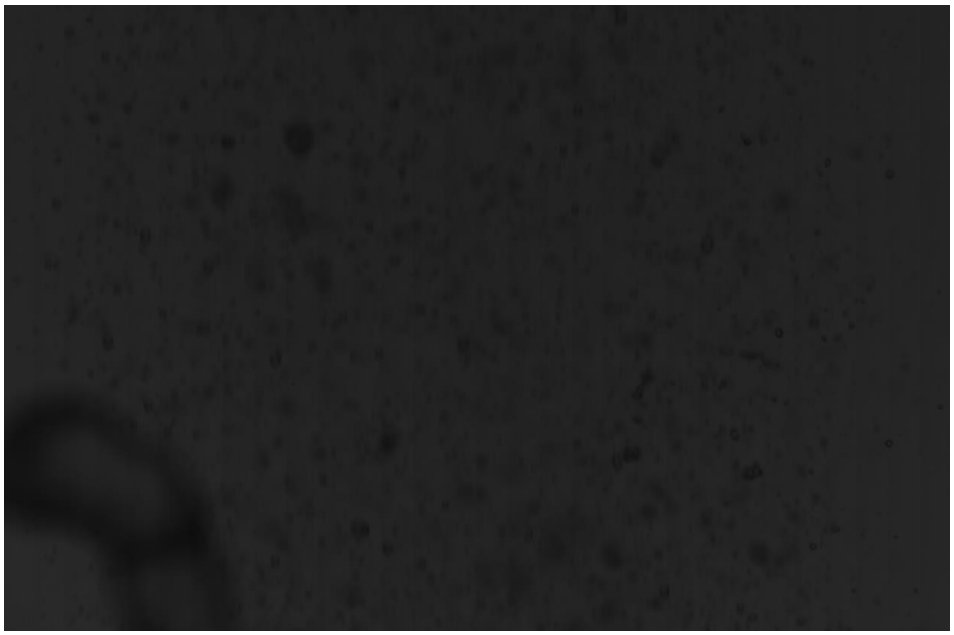

*Figure 89: Raw Image from RPI Test Facility with Large Droplet from Unintentional Secondary Annular Film in Bottom Left.*

A final idea for the future is using artificial intelligence to create a better droplet identification method. The images processed by the current droplet identification program could serve as a strong training dataset for the first generation of an artificial intelligence method. This could eventually lead to the creation of a more robust program that can process the data more efficiently and maximize the number of in-focus droplets analyzed. A program like this would also be able to be used more easily to identify droplets in many different configurations and fields with very different setups. An example could be identifying droplet size and velocity from a human sneeze, which could aid in research on disease transmission. The droplet measurement technique developed in this study has the potential to help a variety of fields collect droplet data that was previously impossible to collect.

# References


1. P. Fei and Pega Hrnjak, “Adiabatic Developing Two-Phase Refrigerant Flow in Manifolds of Heat Exchangers,” Jan. 2004.
2. Y. Liu *et al.*, “Motion characteristics of gas–liquid two-phase flow of microbubbles in a labyrinth channel used for aerated drip irrigation,” *Water*, vol. 15, no. 7, p. 1432, 2023. doi:10.3390/w15071432
3. R. Dhand and J. Li, “Coughs and Sneezes: Their Role in Transmission of Respiratory Viral Infections, Including SARS-CoV-2,” American Journal of Respiratory and Critical Care Medicine, vol. 202, no. 5, pp. 651–659, Sep. 2020, doi: https://doi.org/10.1164/rccm.202004-1263pp.
4. “NRC: Glossary -- Coolant,” www.nrc.gov. https://www.nrc.gov/reading-rm/basic-ref/glossary/coolant.html
5. Jae Ryong Lee, Sang Gi Park, Han Young Yoon, Hyoung Tae Kim, and Jae Jun Jeong, “Numerical study for CANDU moderator temperature prediction by using the two-phase flow analysis code, CUPID,” Annals of Nuclear Energy, vol. 59, pp. 139–148, Sep. 2013, doi: https://doi.org/10.1016/j.anucene.2013.04.002.
6. F. Zhao, X. Yan, H. Bo, T. Meng, C. Zeng, and S. Tan, “Application of droplet motion and phase change model in containment spray system,” Annals of Nuclear Energy, vol. 131, pp. 123–137, Sep. 2019, doi: https://doi.org/10.1016/j.anucene.2019.03.026.
7. Toru Oumaya, A. Nakamura, and N. Takenaka, “Results of a Steam-Water Experiment Simulating Two-Phase Flow in Pressurizer Spray Piping,” Volume 3: Thermal Hydraulics; Current Advanced Reactors: Plant Design, Construction, Workforce and Public Acceptance, Jan. 2009, doi: https://doi.org/10.1115/icone17-75582.
8. Geoffrey Frederick Hewitt and N. S. Hall-Taylor, Annular Two-phase Flow. Pergamon, 1970.
9. Y. Liu, Class Lecture, Topic: “Reactor Thermal Hydraulics: Introduction to Two-Phase Flow.” Department of Mechanical Engineering, Virginia Tech, Blacksburg, Virginia, November 2021.
10. K. Mishima and M. Ishii, “Flow regime transition criteria for upward two-phase flow in vertical tubes,” International Journal of Heat and Mass Transfer, vol. 27, no. 5, pp. 723–737, May 1984, doi: https://doi.org/10.1016/0017-9310(84)90142-x.
11. M. Ishii and M. A. Grolmes, “Inception criteria for droplet entrainment in two-phase concurrent film flow,” AIChE Journal, vol. 21, no. 2, pp. 308–318, Mar. 1975, doi: https://doi.org/10.1002/aic.690210212.
12. H. Du, I. Yilgor, and S. Shi, “Design of a Two-Phase Flow Facility for Investigation of Droplet Entrainment in Countercurrent Annular Flow,” Trans. Am. Nucl. Soc., vol. 125, no. 1, pp. 1276-1279, 2021, doi: https://doi.org/10.13182/T125-37101.
13. Kataoka, I., Ishii, M., Mishima, K., "Generation and Size Distribution of Droplet in Annular Two-Phase Flow," Transactions of the ASME. Journal of Fluids Engineering, Vol. 105, pp. 230-238, 1983.
14. G. Kocamustafaogullari, S. R. Smits, and J. Razi, “Maximum and mean droplet sizes in annular two-phase flow,” International Journal of Heat and Mass Transfer, vol. 37, no. 6, pp. 955–965, Apr. 1994, doi: https://doi.org/10.1016/0017-9310(94)90220-8.
15. K. Song and Y. Liu, “A compact x-ray system for two-phase flow measurement,” Measurement Science and Technology, vol. 29, no. 2, pp. 025305–025305, Jan. 2018, doi: https://doi.org/10.1088/1361-6501/aaa283.

16. K. Song, “Two-Phase Flow Measurement using Fast X-ray Line Detector System,” Ph.D. Dissertation, Virginia Tech, 2019.
17. Y. Liu, X. Yang, Q. Zhu, P. Ju, M. Ishii, and J. R. Buchanan, “Development of the droplet-capable conductivity probe for measurement of liquid-dispersed two-phase flow,” International Journal of Multiphase Flow, vol. 88, pp. 238–250, Jan. 2017, doi: https://doi.org/10.1016/j.ijmultiphaseflow.2016.06.012.
18. K. Wongwailikhit, N. Dietrich, G. Hébrard, and P. Painmanakul, “Performance of a Monofiber Optical Probe in Determining the Droplet Size and Velocity in Spray Systems Compared with a High-Speed Camera,” Industrial & Engineering Chemistry Research, vol. 58, no. 51, pp. 23366–23379, Oct. 2019, doi: https://doi.org/10.1021/acs.iecr.9b02446.
19. D. Wang, K. Song, Y. Fu, and Y. Liu, “Integration of conductivity probe with optical and x-ray imaging systems for local air–water two-phase flow measurement,” Measurement Science and Technology, vol. 29, no. 10, pp. 105301–105301, Aug. 2018, doi: https://doi.org/10.1088/1361-6501/aad640.
20. S. H. Pham, Zensaku Kawara, Takehiko Yokomine, and Tomoaki Kunugi, “Measurements of liquid film and droplets of annular two-phase flow on a rod-bundle geometry with spacer,” International Journal of Multiphase Flow, vol. 70, pp. 35–57, Apr. 2015, doi: https://doi.org/10.1016/j.ijmultiphaseflow.2014.11.010.
21. Z. Zhang, Z. Wang, H. Liu, Y. Gao, H. Li, and B. Sun, “Experimental study on entrained droplets in vertical two-phase churn and annular flows,” International Journal of Heat and Mass Transfer, vol. 138, pp. 1346–1358, Aug. 2019, doi: https://doi.org/10.1016/j.ijheatmasstransfer.2019.04.126.
22. Y. Fu and Y. Liu, “Development of a robust image processing technique for bubbly flow measurement in a narrow rectangular channel,” vol. 84, pp. 217–228, Sep. 2016, doi: https://doi.org/10.1016/j.ijmultiphaseflow.2016.04.011.
23. Y. Fu and Y. Liu, “BubGAN: Bubble generative adversarial networks for synthesizing realistic bubbly flow images,” Chemical Engineering Science, vol. 204, pp. 35–47, Aug. 2019, doi: https://doi.org/10.1016/j.ces.2019.04.004.
24. D. Wang et al., “A Comprehensive Measurement of Bubbly Flow in a 30 mm x 10 mm Rectangular Channel,” Jan. 2023, doi: https://doi.org/10.13182/nureth20-40012.
25. Y. Fu and Y. Liu, “3D bubble reconstruction using multiple cameras and space carving method,” Measurement Science and Technology, vol. 29, no. 7, p. 075206, Jun. 2018, doi: https://doi.org/10.1088/1361-6501/aac4aa.
26. Y. Fu, D. Wang, Y. Liu, X. Sun, T. Worosz, and J. R. Buchanan, “A 3-D Imaging System for Bubbly Flow Measurement,” Jan. 2023, doi: https://doi.org/10.13182/nureth20-40011.
27. S. Shi, D. Wang, Y. Qian, X. Sun, Y. Liu, and A. Tentner, “Liquid-phase turbulence measurements in air-water two-phase flows using particle image velocimetry,” Progress in Nuclear Energy, vol. 124, pp. 103334–103334, Jun. 2020, doi: https://doi.org/10.1016/j.pnucene.2020.103334.
28. Wang, Z., “Comparison of Particle Based Velocimetry Techniques in Single Phase Flow Measurement” M.Eng. Thesis, Virginia Tech, 2017.
29. Photron Limited, “Fastcam SA4 Fastcam SA4 RV Hardware Manual,” Revision 1.07E, Feb. 2014.
30. Photron Limited, “Fastcam SA6 Fastcam SA6 RV Hardware Manual,” Revision 1.02E, Feb. 2014.

31. Mugikura, Y., “Application of Defocusing Technique to Bubble Depth Measurement” M.S. Thesis, Virginia Tech, 2016.
32. “Soda Lime Solid Glass Microspheres 2.5g/cc - 1um to 4400um (4.4mm),” Cospheric. https://www.cospheric.com/SLGMSc_solid_glass_spheres_beads_microns.htm.
33. “Rayleigh Scattering,” Georgetown.edu, 2022. https://site.physics.georgetown.edu/~vankeu/webtext2/Workspace/Rayleigh%20scattering/Rayleigh%20scattering.htm.
34. P. Sawant, M. Ishii, and M. Mori, “Prediction of amount of entrained droplets in vertical annular two-phase flow,” International Journal of Heat and Fluid Flow, vol. 30, no. 4, pp. 715–728, Aug. 2009, doi: https://doi.org/10.1016/j.ijheatfluidflow.2009.03.003.
35. Series RM Rate-Master Flowmeters Specifications-Installation and Operating Instructions, Bulletin F-43, Dwyer Instruments Inc., Michigan City, Indiana, 2022.
36. “Weather in March 2024 in Troy, New York, USA,” www.timeanddate.com. https://www.timeanddate.com/weather/usa/troy-ny/historic?month=3&year=2024 (accessed Apr. 01, 2024).

# Appendix A

# List of Codes

This appendix contains a list of all the codes created or modified in Matlab for the present study with a brief description.

1. Flow Regime Map: This code takes fluids physical properties and flow channel geometric parameters and creates a two-phase flow regime map with superficial velocities as the axes [10].
2. Droplet Size Distribution 1: This code takes superficial velocities and flow channel geometric parameters and creates a droplet size distribution according to the model created by Kataoka et al. [13].
3. Droplet Size Distribution 2: This code takes superficial velocities and flow channel geometric parameters and creates a droplet size distribution according to the model created by Kocamustafaogullari et al. [14].
4. Depth-of-Field Calibration: This code takes calibration images and creates statistical plots to study the focal plane depth.
5. Droplet Identification Program, Droplet Identification: This code is the first step in the droplet identification program where raw images and filter values are inputs and statistical values about the identified in-focus droplets are the outputs [22].

6. Droplet Identification Program, Outline Inspection: This code is the second step in the droplet identification program where the recorded outlines for each recorded droplet from the previous frame are displayed over each original raw image [22].

7. Droplet Identification Program, Statistics Compilation: This code is the third step in the droplet identification program where the statistics from each frame are compiled together and droplet size distributions are created [22].

8. Droplet Identification Program, Radial Distributions: This code is the fourth step in the droplet identification program where radial droplet distributions are created [22].

9. Droplet PSV Program, Streak Identification: This code is the first half of the PSV program where in-focus streaks are identified and recorded for each frame [28].

10. Droplet PSV Program, Statistical Distributions: This code is the second half of the PSV program where the velocity of each droplet is calculated, and distributions are created [28].

# Appendix B

# Droplets from Annular Flow Distributions

This appendix contains the complete set of figures of droplet distributions captured by the SA6 camera for the testing repetitions from run 1 ($j_g$ = 22.0 m/s and $j_f$ = 0.089 m/s) and run 3 ($j_g$ = 33.5 m/s and $j_f$ = 0.089 m/s). The radial distributions included from high shutter speed data to measure droplet size are plots for droplet fraction, $\alpha_d$, and number density of droplets. A histogram for the droplet size distribution, independent of location is also included for each high shutter speed repetition. All three of these distributions contain the average of each respective value, with the standard deviations also plotted on the droplet fraction and number density plots. For the velocity data, graphs are included that present the radial distributions of the total speed, the horizontal component of speed, and the vertical component of speed.

Run 1, Size Data, Repetition 1:

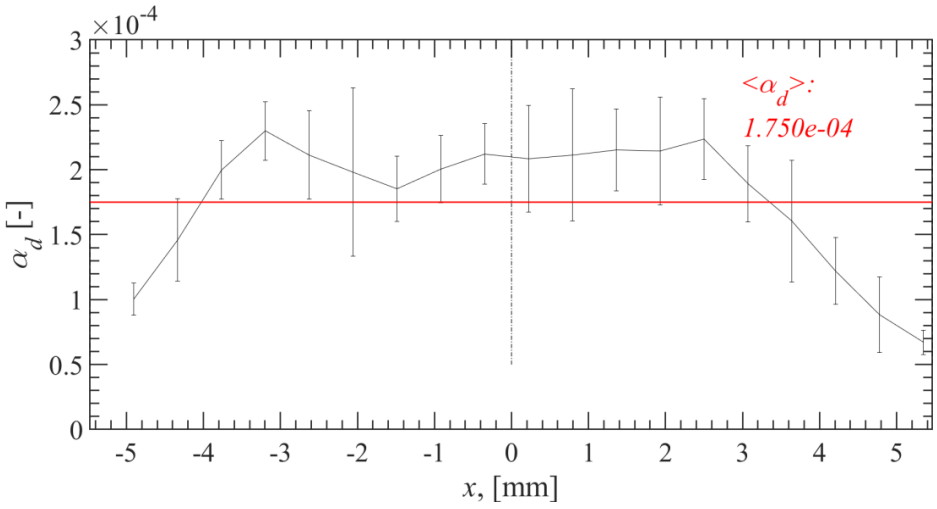


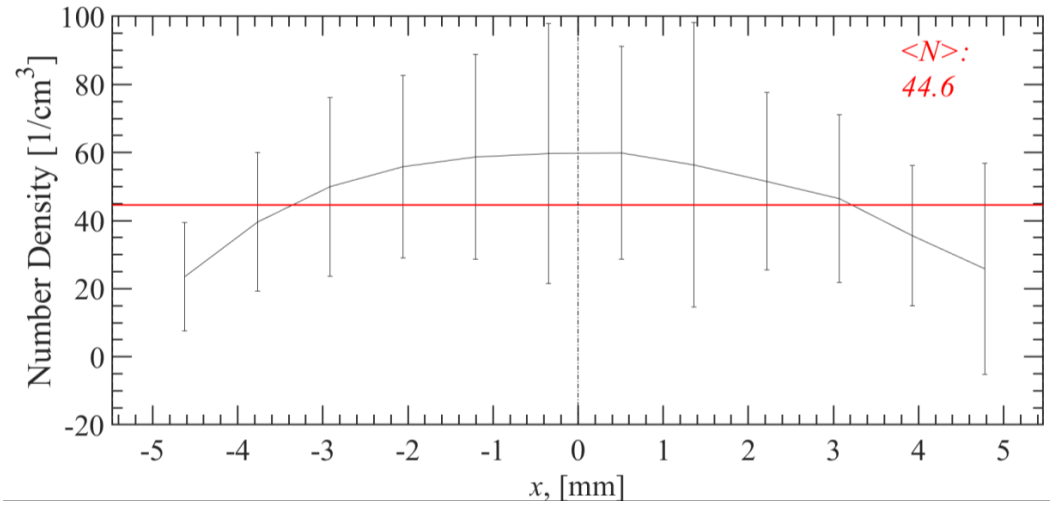


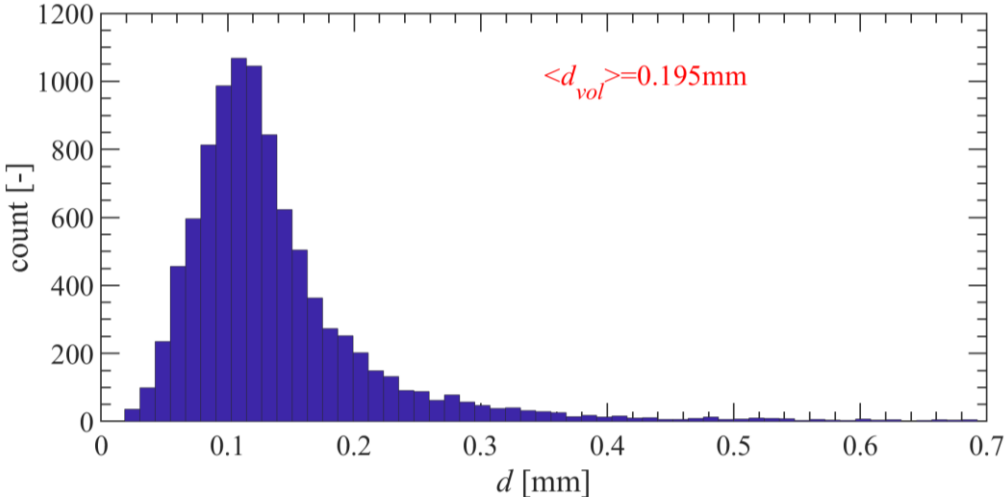

Run 1, Size Data, Repetition 2:

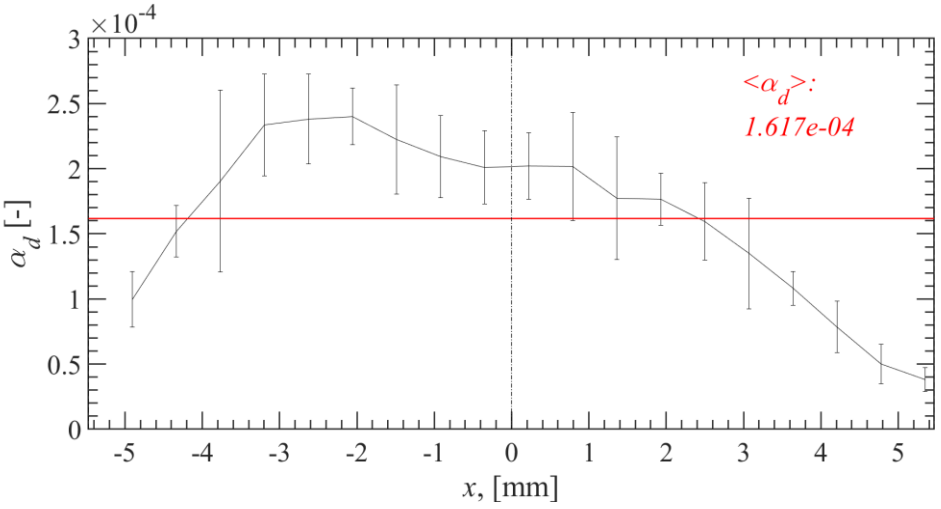


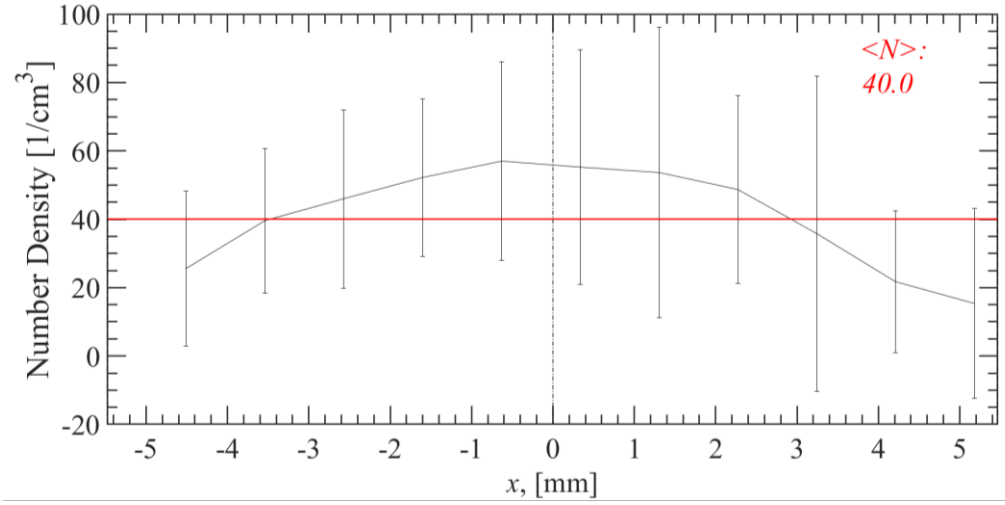


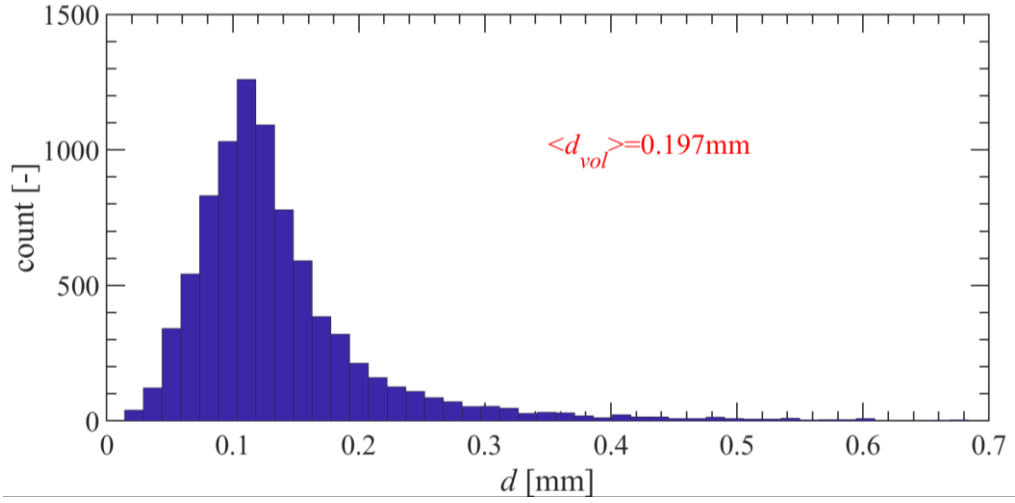

Run 3, Size Data, Repetition 1:

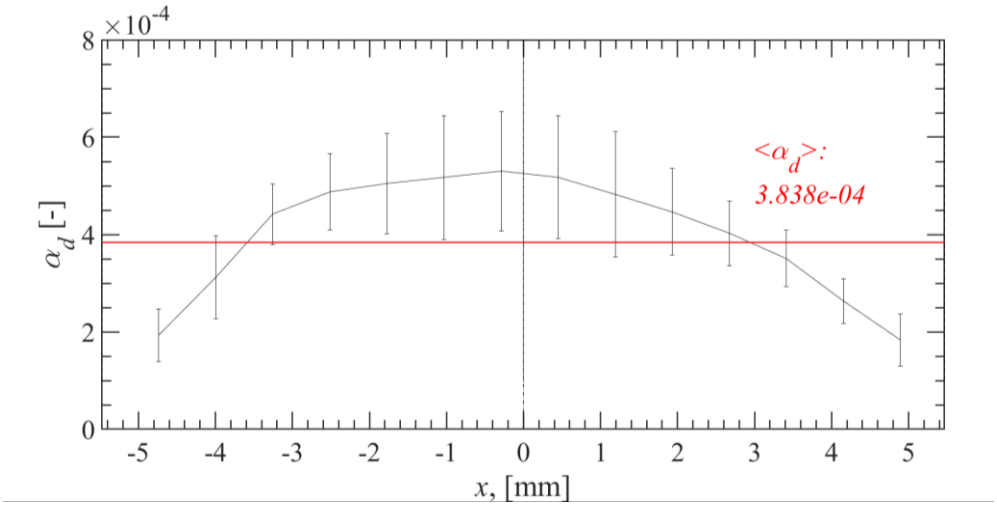


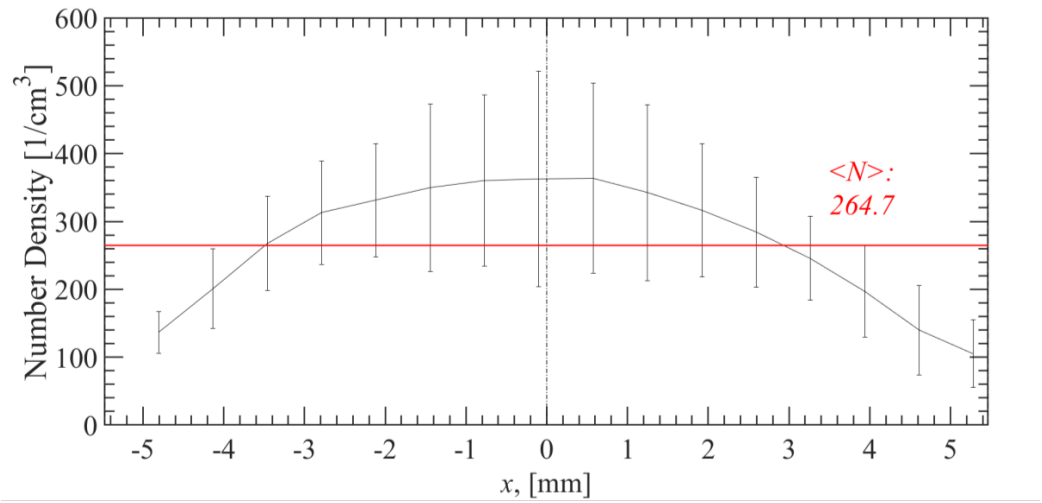


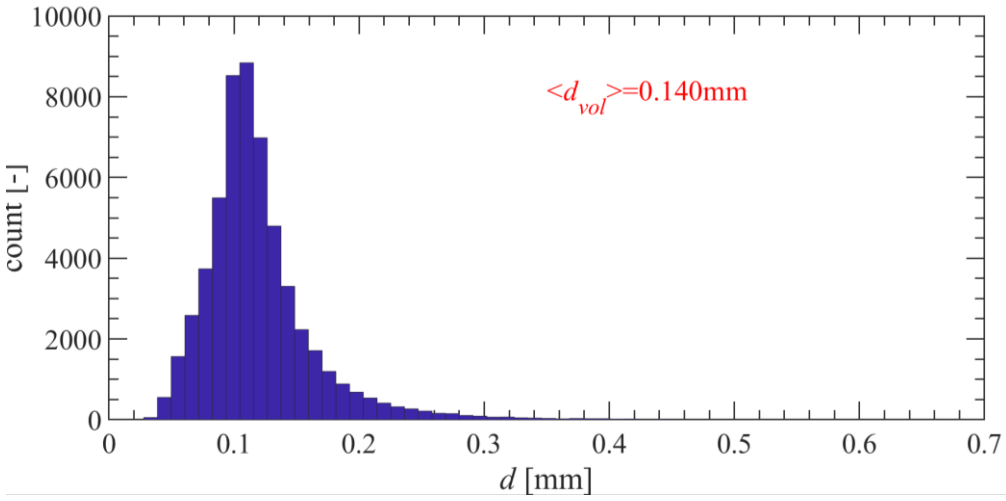

Run 3, Size Data, Repetition 2:

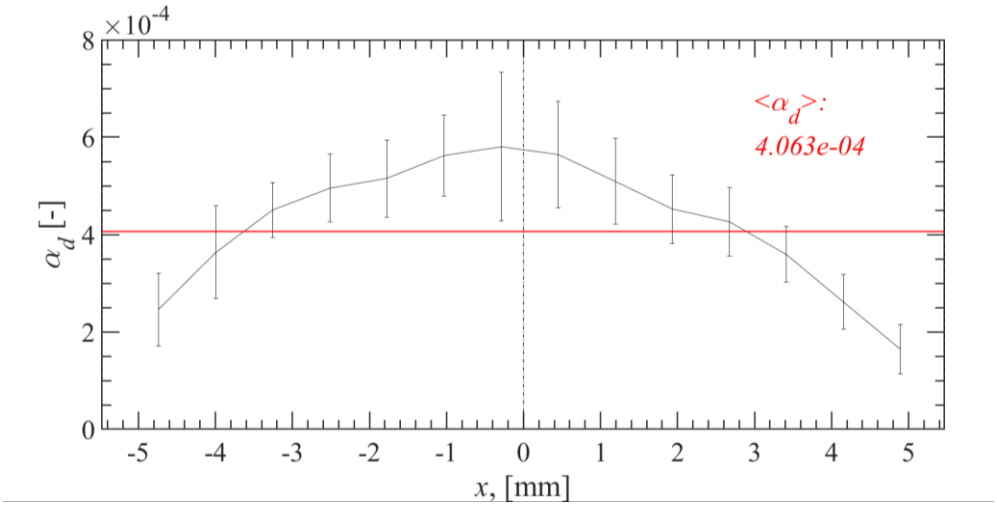


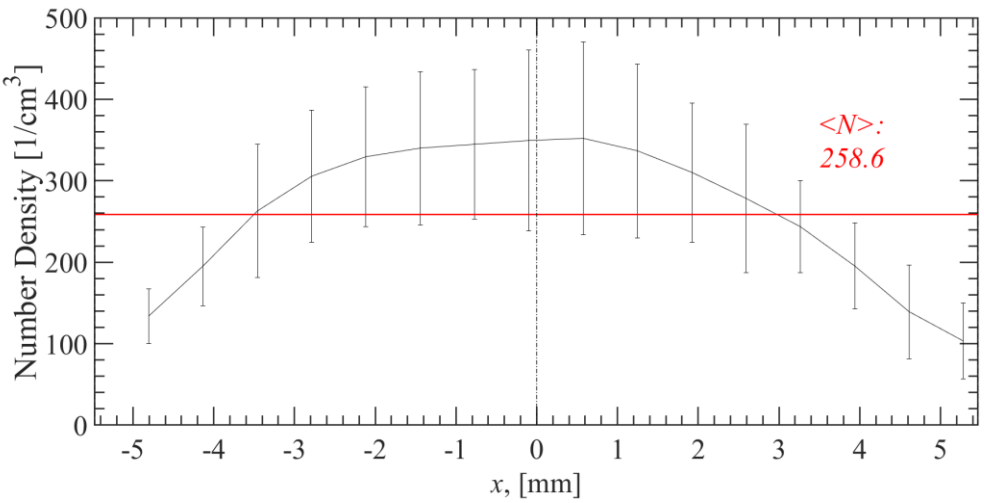


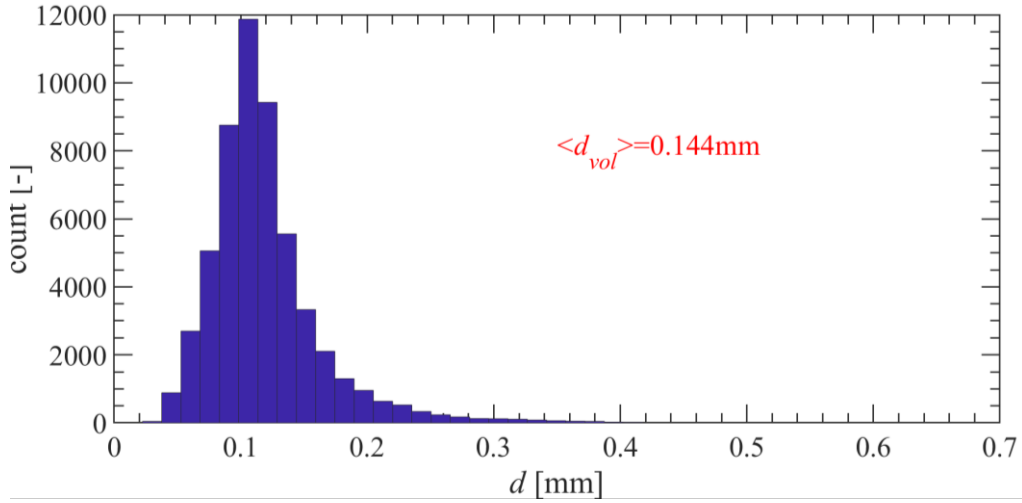

Run 1, Velocity Data, Repetition 1:

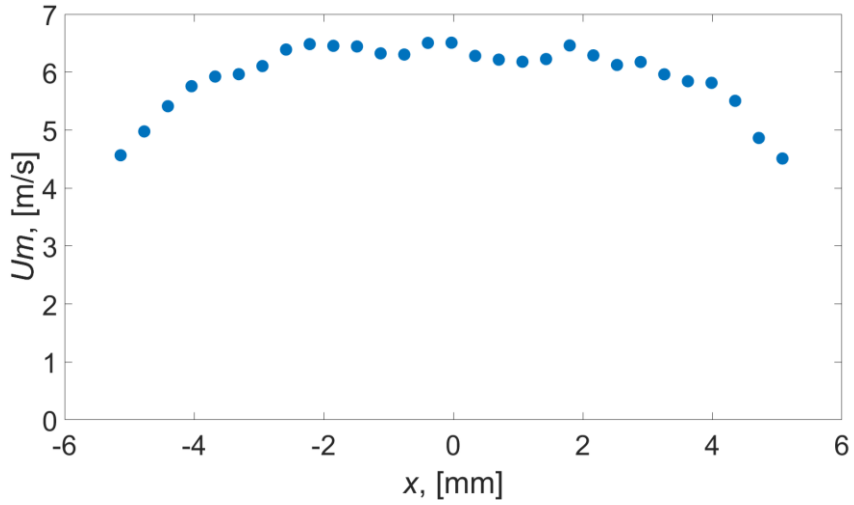


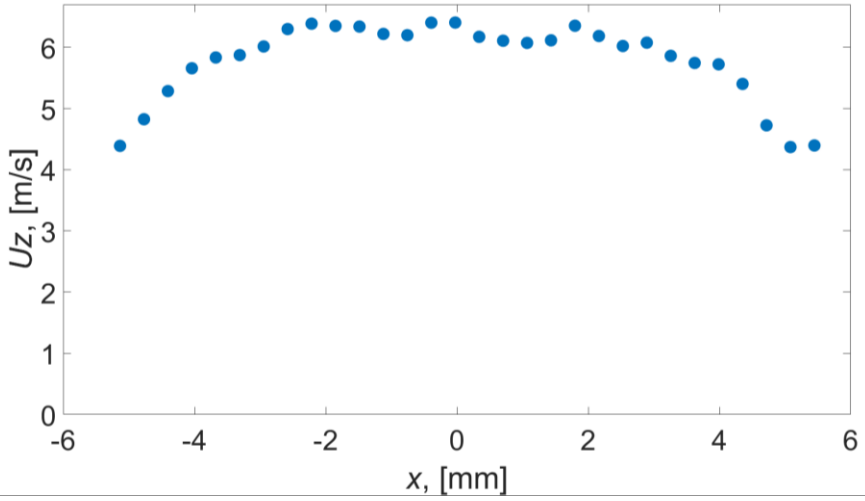


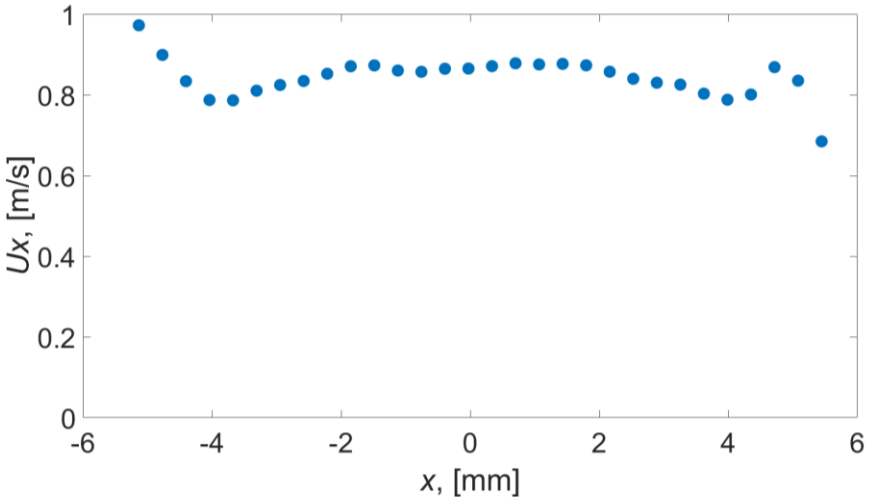

Run 1, Velocity Data, Repetition 2:

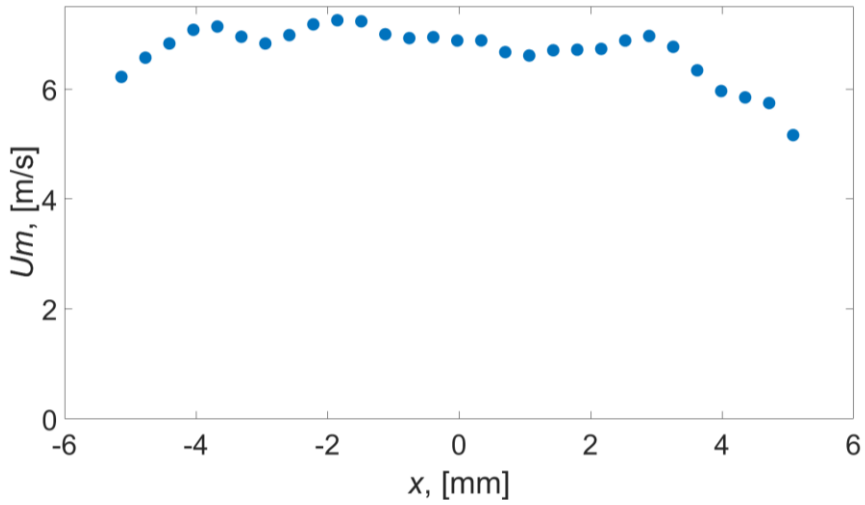


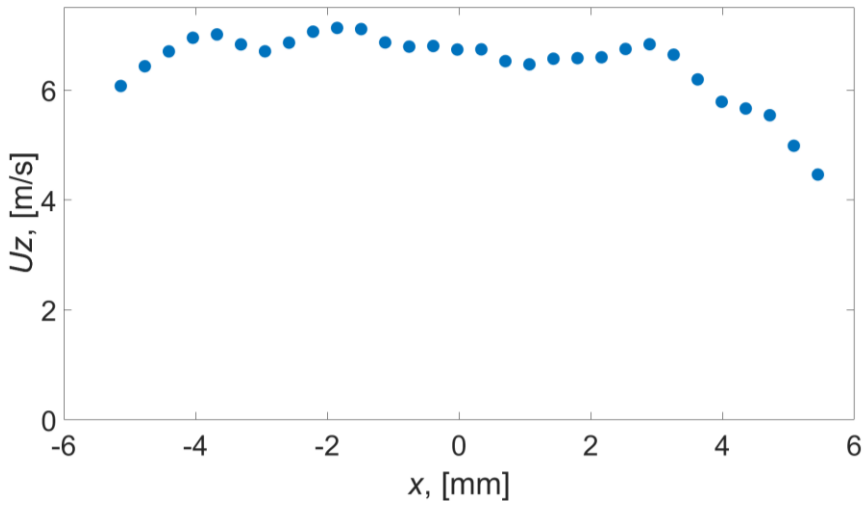


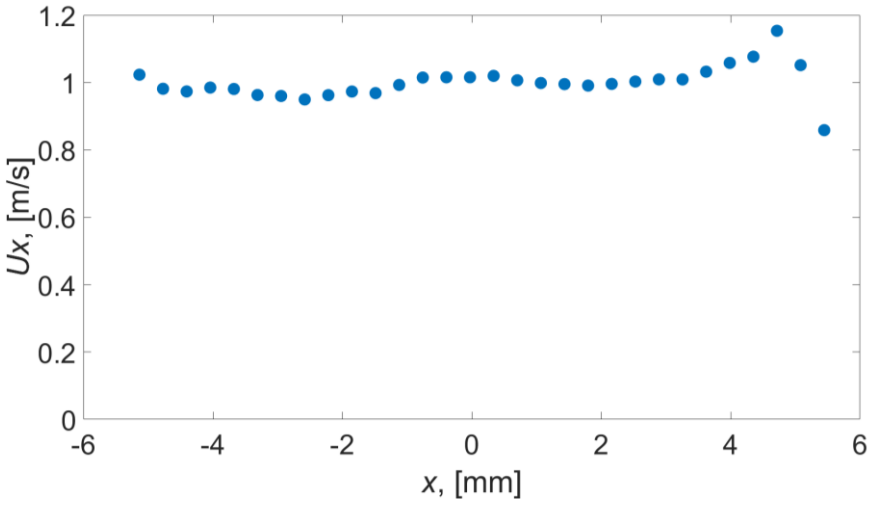

Run 3, Velocity Data, Repetition 1:

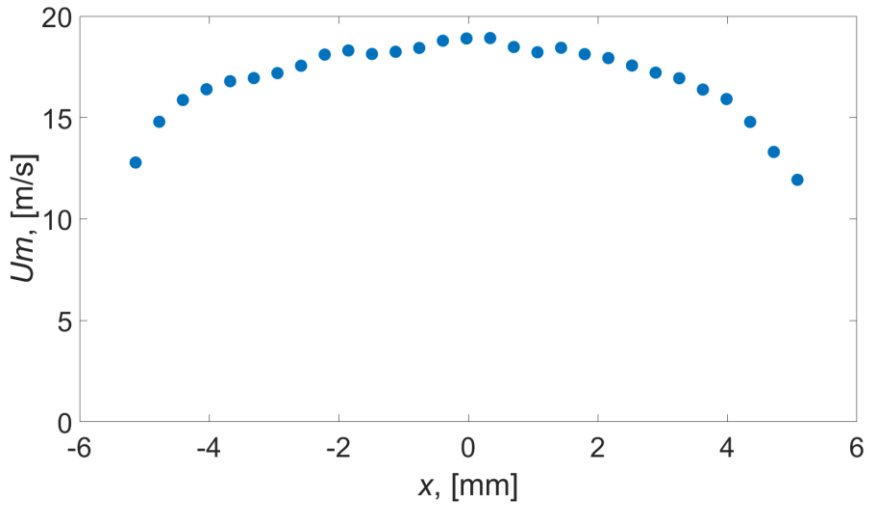


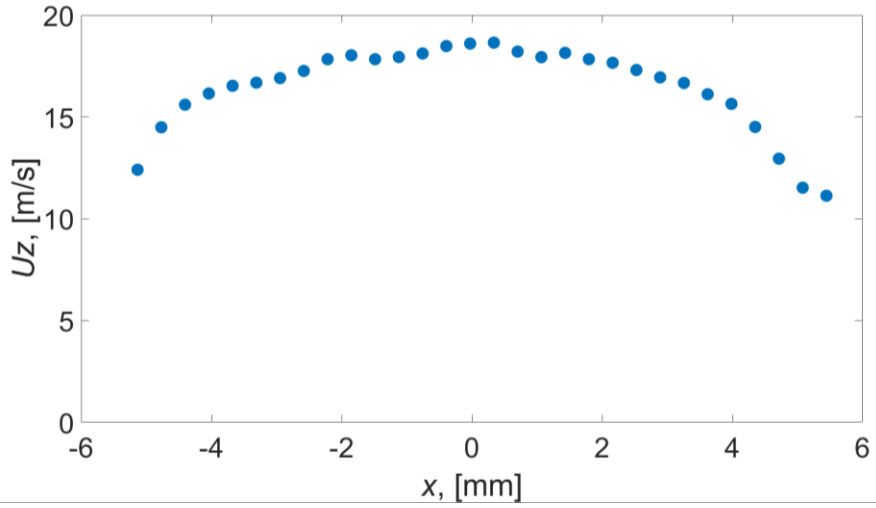


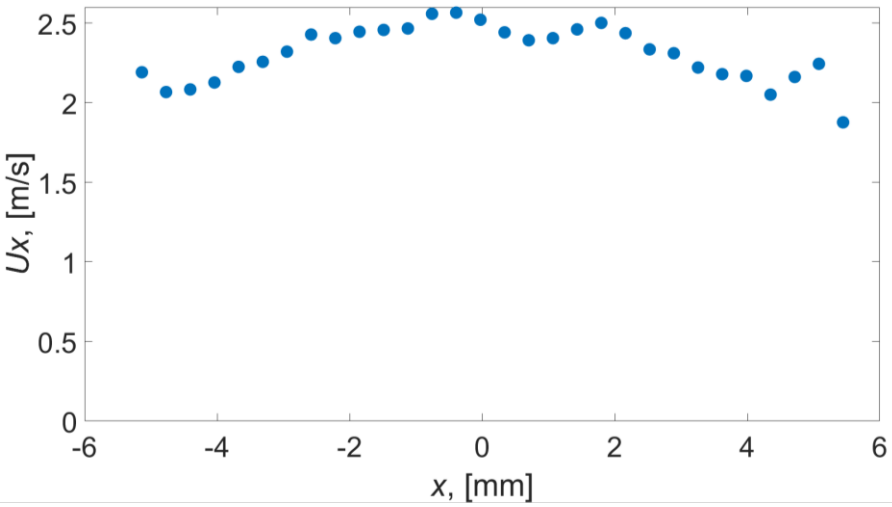

Run 3, Velocity Data, Repetition 2: